New high-performance oxide-based CVD coatings

DI David Hochauer

Leoben, February 2010

Being a thesis in partial fulfillment of the requirements for the degree of a
Doctor of montanistic sciences (Dr. mont.)
at the University of Leoben

Financial support by the Austrian Federal Government and the Styrian Provincial Government, represented by Österreichische Forschungsförderungsgesellschaft mbH and by Steirische Wirtschaftsförderungsgesellschaft mbH, within the research activities of the K2 Competence Centre on “Integrated Research in Materials, Processing and Product Engineering”, operated by the Materials Center Leoben Forschung GmbH in the framework of the Austrian COMET Competence Centre Programme, is gratefully acknowledged. This thesis was conducted at the Department of Physical Metallurgy and Materials Testing at the Montanuniversität Leoben, Austria in cooperation with the Materials Center Leoben Forschung GmbH in Leoben, Austria, CERATIZIT Austria GmbH in Reutte, Austria, CERATIZIT Luxembourg SARL in Mamer, Luxembourg and PLANSEE SE in Reutte, Austria.

Affidavit

I declare in lieu of oath that I did the PhD thesis by myself using only literature cited in this volume.

David Hochauer

Leoben, February 2010

Acknowledgements

I would like to thank Univ. Prof. DI Dr. Helmut Clemens, head of the Department of Physical Metallurgy and Materials Testing at the University of Leoben, for the opportunity to conduct my thesis at this institute, for the friendly and supportive environment.

My sincerest gratitude is due to ao. Prof. DI Dr. Christian Mitterer, chief of the Thin Films Group in Leoben. First of all, he established the preconditions for this work and gave me the chance to join this project. Also, he encouraged me always in the right moment and my asking for advice never was in vain, although I have been quite late sometimes. His subtle and kind supervision created an atmosphere which enhanced my abilities to learn and evolve. Finally, he was patient enough to allow me finishing this thesis at my own chosen speed – while still supporting it – which I appreciate as a huge gift.

I am also thankful to ao. Prof. DI Dr. Reinhold Ebner and to Dr. Richard Schanner, managing directors of the Materials Center Leoben (MCL), for giving me the opportunity to carry out my thesis within an MCL project. I am indebted to the MCL staff and the co-workers there who supported this project as good as possible. They offered straightforward help and solutions each time I was asking for.

This whole project would not have been possible, without the cooperating companies. I am deeply grateful to DI Dr. Martin Kathrein from CERATIZIT Austria, who outlined this work and convinced the company. Without his commitment this project would not have been started. Furthermore, our colloquies always added a valuable point-of-view, improved my knowledge and broadened my mind.
I really did appreciate the analytical and experimental support by MSc Marianne Penoy and DI Claude Michotte from CERATIZIT Luxembourg. Not a single question remained unanswered and the discussions were always fruitful and informative. The same was true for Dr. Hans-Peter Martinz from PLANSEE SE who provided his wide experience and knowledge with an inspiring attitude. Owing to him and Brigitte Nigg, the deposition experiments in the corrosion lab were successful and save.

The diploma students DI Christoph Czettl and DI Manfred Schlögl, as well as the student co-workers Oliver Jantschner and DI Christiane Vieh were a first-class band. Your input was an

important factor within this project. Working with you, as well as your company was an experience which I would not like to miss and our friendship may persist.

Being part of the Thin Films Group in Leoben is a beautiful status. Scientific atmosphere and work shared with friends, I would say. Although I have no comparison, I can hardly imagine a better place for doing one's thesis. I have enjoyed the last few years very much and I will rove back every now and then, hopefully not only with my thoughts.

Thanks from the bottom of my heart to my wife and my family, for their love, patience, solidarity and support. Their acceptance and the feeling of security generated a place of peace – of course not in a superficial way – but for mind and soul.
Thank you!
For coddle me up whenever necessary …
For your care …
For your …

Ich lebe mein Leben in wachsenden Ringen,
die sich über die Dinge ziehn.
Ich werde den letzten vielleicht nicht vollbringen,
aber versuchen will ich ihn.

Ich kreise um Gott, um den uralten Turm,
und ich kreise jahrtausendelang;
und ich weiß noch nicht: bin ich ein Falke, ein Sturm
oder ein großer Gesang.

Rainer Maria Rilke

Contents

1. Introduction

In the field of cutting applications, hard coatings are utilized in order to increase tool performance since the late 1960-ies [1]. These hard coatings offer retarded tool wear, increased cutting speed and extended abilities concerning difficult-to-machine materials. For cemented carbide cutting tools – which are resistant to elevated temperatures – thermal chemical vapor deposition (CVD) was the first coating synthesis method and it is still dominating nowadays. While the first wear protective hard coatings were carbides and nitrides, alumina (Al_2O_3) was introduced in the 1970's [2]. Its most prominent benefits are high chemical stability, high hot hardness and rather low thermal conductivity. Although other types of oxides have been investigated [3, 4], the utilization of alumina as an oxide component within commercial CVD coating architectures is unrivaled. Earlier CVD alumina studies were concerned with basic deposition parameter variations and stabilization conditions for specific alumina polymorphs. Following, the microstructure of alumina was characterized in detail [5]. The resulting knowledge allows to control the growth of a specific alumina polymorph with improved adhesion and selected texture [6, 7]. However, only a few studies are published concerning the improvement of CVD alumina coating properties by intentional incorporation of dopants, although there are promising references for bulk alumina. Therefore, the present thesis focuses on doping and alloying of CVD alumina and advances two experimental approaches: First, previous studies with the doping elements titanium and boron [8] were continued and extended on production-scale deposition units. Second, new doping elements were investigated on laboratory-scale, which involved the selection of dopant precursors with regard to their handling and process compatibility.

2. Alumina

2.1. Alumina phases

Within the binary equilibrium phase diagram of aluminum and oxygen (Fig. 1), there are two solids (Al(s), α-Al_2O_3(s)), two immiscible liquids (Al(l), α-Al_2O_3(l)) and the gas phase, which consists of oxide species as well as the single elements. The solubility of oxygen in aluminum is unknown but small and stoichiometric deviations of the α-Al_2O_3 compound are also supposed to be small [9]. There is no stable, condensed phase with an atom ratio of Al/O < 0.6 and the reported existence of oxides with an Al/O ratio significantly deviating from the value of 2/3 is not well established.

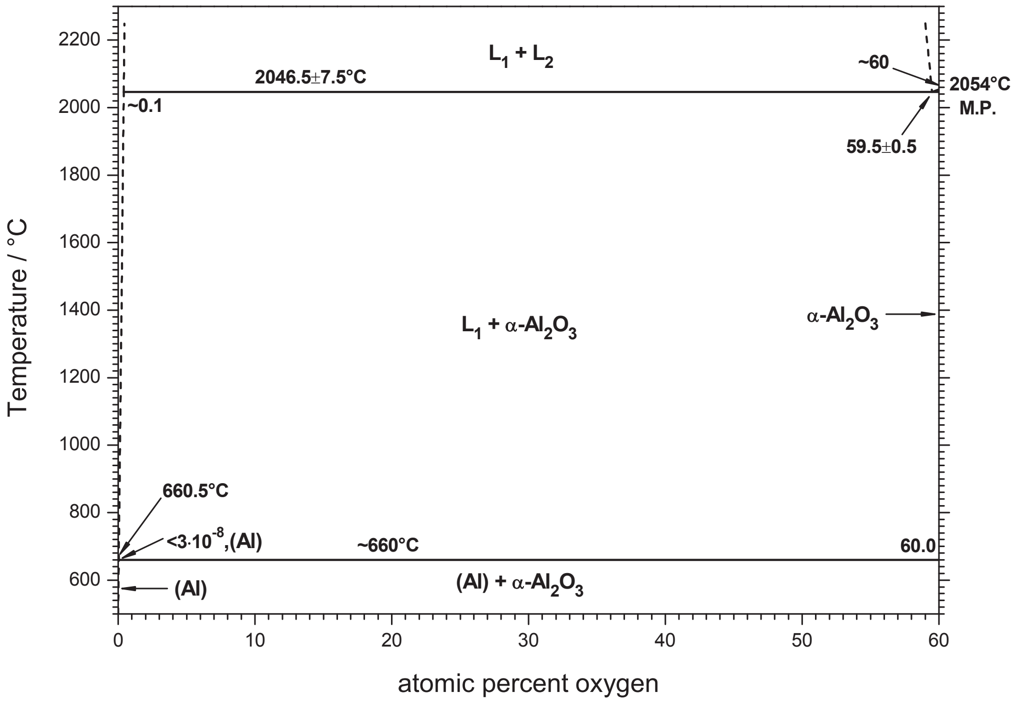

Fig. 1. Al-O binary phase diagram (condensed system) [10]

Beside the stable, amphoteric, hexagonal α-Al_2O_3 (also denoted as corundum, sapphire or α-alumina), there are several metastable polymorphs (γ, δ, κ, η, θ, χ), but all Al_2O_3 species are composed of close-packed layers of oxygen with different stacking sequences and different cation locations (tetrahedral and octahedral sites of the anion sublattice)[9, 10]. The crystal structures of α-Al_2O_3 and κ-Al_2O_3 as the most important ones in CVD technology are displayed in Fig. 2. Which alumina polymorph is present, depends on the synthesis method, starting material (e.g. the kind and condition of aluminum hydroxide mineral), temperature and atmosphere [11]. For a calcination process, starting with submicron sized gibbsite, the process of dehydration starts quickly at ~200°C but is not finished until a temperature of about 800°C is reached [12]. There, gibbsite transforms to hydrous χ-Al_2O_3, which transforms to anhydrous κ-Al_2O_3 and α-Al_2O_3. Different starting materials consequence other transformation series, e.g. diaspore transforms directly to α-Al_2O_3 at a relatively low temperature (450-600°C). However, for some alumina polymorphs (η-Al_2O_3, γ-Al_2O_3, …), the question concerning their degree of hydration is not clearly answered [9].

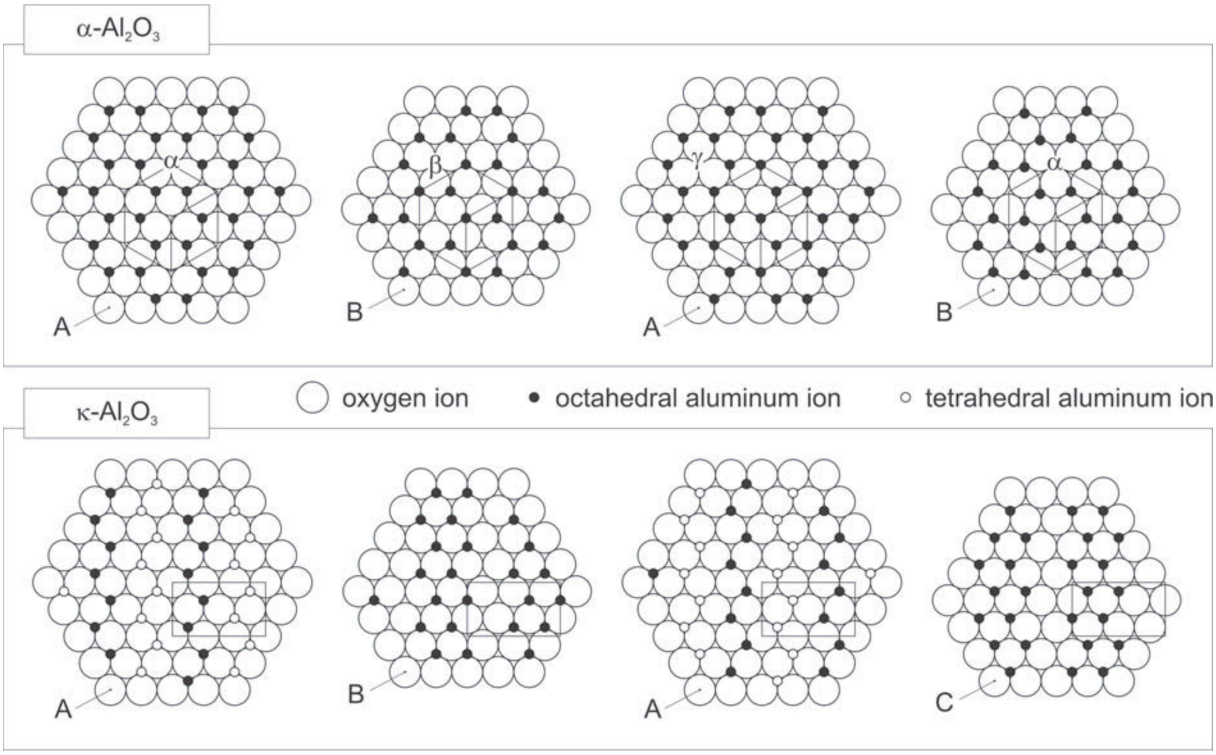

Fig. 2. Crystal structure of α-Al_2O_3 (upper row)[13] and κ-Al_2O_3 (lower row)[14], displaying double layers of oxygen ions with aluminum ions above. The stacking sequence for the oxygen anion sublattice is indicated with capital letters. For α-Al_2O_3, the hexagonal and the rhombohedral unit cells are indicated with solid straight lines and the first four double layers are drawn. The three possible positions for the aluminum vacancy (octahedral) are labeled with Greek letters. The complete stacking sequence (ABABAB) contains a fifth (A stacking) and a sixth double layer (B stacking) with aluminum vacancies in the β and γ position. For κ-Al_2O_3 the complete stacking sequence is drawn (ABAC) and the orthorhombic unit cell is indicated with solid straight lines. Unlike α-Al_2O_3, the aluminum ions are located within octahedral and tetrahedral interstices of the oxygen sublattice. For the deviations of the atom position from the ideal (unrelaxed) lattice shown here, see [15-17].

Comparing aluminum oxide to other oxide ceramics (see Table 1) indicates a relatively high thermal conductivity, an average melting point and a high hardness of alumina. Self-diffusion within alumina – which is very sensitive to low concentrations of impurities – seems to be a difficult topic, since the published studies are far from consistent although decades of scientific work are spent [18, 19].

Apart from the synthesis of bulk alumina starting from aluminum hydrates, also CVD is a possible route, where α-, κ- γ- and θ-Al_2O_3 phases are reported [1, 20, 21]. Alumina properties and the formation of the specific alumina polymorphs are influenced by the type of CVD precursor, deposition rate and gas phase additives, but deposition temperature is the main parameter. For example, below a deposition temperature of ~800°C, amorphous aluminum oxide is formed [22]. Furthermore, the deposition conditions during alumina nucleation [7] and surface treatment procedures of the substrate [23] are crucial. However, the detailed description of the transformation from a metastable alumina polymorph to the stable α-Al_2O_3 would need an experimental observation of the very first stage of transformation nucleation [9], which is not available in literature.

Table 1

Comparison of selected oxide ceramic materials [24]

Ceramic	melting point [°C]	density [g cm^{-3}]	thermal conductivity [W m^{-1} K^{-1}]	hardness [GPa]
Al_2O_3	2015	3.9	34	19.1
HfO_2	2750	10	1.6	15
SiO_2	1610	2.2	12	6-10
TiO_2	1850	4.25	8	11 [25]
ZrO_2	2700	10.2	3	17
Y_2O_3	2690, 2439 [26]	5 [26]	14 [27]	

2.2. Ternary systems

Apart from the rather scarce cases of complete (e.g. Cr_2O_3) and partial solubility (e.g. Ga_2O_3), there are generally low solubility limits determined for doping elements within the α-Al_2O_3 lattice. This finding is confirmed by calculations, which show high formation energies for interstitial and substitutional atoms within the α-Al_2O_3 lattice [28, 29]. For example, quasibinary oxide phase diagrams [30] show no solubility for the oxides of Si, V, U, Sn, Ti and B within alumina. Moreover, the reported solubility of Y_2O_3 in α-Al_2O_3 suggested at high temperatures (~5 mol.% at 1860°C) [30], turned out to be almost inexistent (<10 ppm) [31, 32]. Consequently, doping and alloying of alumina often causes segregation at interfaces [33] or the formation of additional phases [32, 34]. Most data concerning the solubility limits refer to bulk material (Table 2) and there are no quantitative investigations concerning doping element concentration for CVD alumina coatings found, but a few qualitative studies concerning the influence of impurities and dopants [35-37].

Table 2

Solubility limits for selected elements within alumina

Element	Solubility	Temperature range / K	Influence	Reference
Mn	0.5 %	-	enhanced densification	[38]
Mg	max. 132±11 ppm	1600°C		[39]
			faster pipe diffusion, 6x	[40]
Ca	< 30 ppm	1900°C		[41]
Si	< 300 ppm	1900°C		[41]
Y	< 10 ppm	-	less creep, higher toughness	[31, 32, 42]
Ti	1.0 / 2.5 mol % Ti_2O_3	1400 / 1700°C		[43]
	~500 ppm	1530°C		[44]

2.3. Technological properties

2.3.1. Chemical stability

In the field of cutting, a pronounced chemical stability is reported for CVD alumina coatings [45, 46], which is one of the advantages of ceramics compared to other classes of materials, while others are high hardness, high melting point and good wear resistance. Nevertheless, the corrosion resistance of alumina might be inferior to other engineering ceramics like silicon carbide or zirconia [47] and the amphoteric character of aluminum allows alumina dissolution in acids as well as in bases. Investigations concerning the acid and alkali corrosion resistance of alumina often show that additives or impurities, existing at grain boundaries, are the main reason for alumina corrosion, where increasing synthesis temperature improves the chemical stability [48, 49]. Most cutting conditions are rather chemically neutral (apart from wood cutting [50]) where an alumina top-layer offers good oxidation protection for the base-layers and/or the substrate. In particular, this oxidation resistance is superior to most of the common wear resistant nitride or carbide coatings, which oxidize already around 600°C [51-53]. However, with regard to chemical stability, the addition of doping elements could also lower the inertness of an alumina coating, due to segregation at grain boundaries or due to the formation of a second phase with a lower chemical stability [49].

2.3.2. Thermal properties

The thermal properties of alumina are closely related to the present alumina polymorph. Not only their different thermal data, but also transformations of polymorphs have major influences (see section 2.1). Moreover, the microstructure, influenced by the desired polymorph and the chosen synthesis route, represents an additional effect on thermal properties [54, 55]. The thermal conductivity and the coefficient of thermal expansion (CTE) are decisive thermal parameters for wear resistant coatings used in cutting application. A low thermal conductivity is favorable, because of the accompanied thermal shielding which results in lower temperatures within the cutting tool. Values of thermal conductivity are listed in Table 3 for a few selected alumina polymorphs as well as two alloyed alumina materials. Beyond microstructure (porosity, grain boundaries, …), two further influences are the crystalline structure and the lattice point defect density. A more complex crystal structure (e.g. an increased number of atoms per unit cell) and an increased density of point defects are related to a lower thermal conductivity. Similar to other point defects, impurities (e.g. solid solution) are related to a decrease of thermal conductivity. Hence, different values of thermal conductivity for similar ceramic materials are often attributed to small amounts of additional elements [54, 56].

For all compound materials, different CTE's are connected to internal stresses, for example thermal stresses within coatings deposited at high temperatures on a substrate different from the coating. Obviously, a bigger difference in CTE and more pronounced changes in temperature increase the stresses generated within different materials and their interfaces. The CTE's for α-Al_2O_3 and κ-Al_2O_3 are given in Table 4, showing a lower and more temperature-dependent value for κ-Al_2O_3. In addition, materials relevant for the deposition of CVD alumina on cutting tools are enclosed. CTE's above (TiN) and below (TiC, AlN) the values of alumina indicate the possibility for designing interlayers with matching CTE by alloying these components and/or varying their composition gradually. This fact may partly explain the successful application of these components in combination with alumina in CVD coating systems [1, 57].

Table 3

Thermal conductivity at 273 K (λ_{273}) and measured within a certain temperature range (λ_T)

Material	λ_{273} / W m^{-1} K^{-1}	λ_T / W m^{-1} K^{-1}	Temperature / K
sapphire (single crystal) [56]	40	170 – 13	120 – 800
bulk alumina (polycrystalline) [54]	-	9 – 5	800 – 1400
α-Al_2O_3 (CVD, crystalline) [56]	26	30 – 13	200 – 600
κ-Al_2O_3 (CVD, crystalline) [56]	7.4	14 – 5	80 – 600
α-Al_2O_3 (PVD, amorphous) [58]	1.6	0.6 – 1.9	80 – 400
$Y_3Al_5O_{12}$ [59]	13.5	140 – 11	60 – 300
bulk $Al_{18}B_4O_{33}$ [55]	~ 6	6 – 4	300 – 900

Table 4

Coefficients of thermal expansion (CTE) and the related temperature range

Material	CTE / 10^{-6} K^{-1}	Temperature / K	source
α-Al_2O_3 (CVD)	8.3	298 – 1073	[24]
bulk α-Al_2O_3	8.3 – 9.5	298	[60]
κ-Al_2O_3 (CVD)	3.8 – 8.1*	296 – 1110	[61]
TiN	9.5		[62]
	9.35	298	[60]
TiC	7.6		[62]
	7.4 – 8.8	298	[60]
TiO_2	9.0	273 – 1273	[24]
AlN	4.3	298 - 673	[24]
Cemented carbide (WC/Co)	4.5 – 6		[62]
	5.7	298	[60]
	5.0 – 7.0	293 – 673	[63]

* different lattice directions specified

2.3.3. Mechanical properties

Bulk alumina is a comparatively hard oxide ceramic (cf. Table 1), showing a hardness value almost linearly decreasing from 15 – 20 GPa at room temperature to a value below 5 GPa at 1400°C for single crystal sapphire and sintered aluminas (Vickers hardness, 4 kg load, vacuum: 10^{-2} Pa) [64]. Reported approaches for hardness enhancement are decreasing the porosity [65], diffusion treatments [66] and ion-implantation [67, 68]. At room temperature, the Young’s modulus is in the range of 400 – 600 GPa, where single crystalline sapphire shows a slightly higher value than polycrystalline alumina [67, 69]. For polycrystalline bulk alumina, grain boundary slip begins to affect high temperature Young’s modulus above 950°C [69]. On the other hand, ion implantation processes do not influence the Young’s modulus as long as crystallinity is not destroyed [67, 68] but a combined implantation and heat treatment process causes lower values [67]. Ion-implantation also increases residual compressive stress and fracture toughness and high-dose ion-implantation consequences a more ductile behavior of alumina, due to lower crystallinity and high residual stresses [70]. Cracking within alumina is reported to be initiated by prior plastic deformation, where polycrystalline alumina plastifies at a lower stress level, causing fatigue fracture at lower loads compared to single crystalline sapphire [71].

CVD alumina coatings also show a decreasing hardness from ~23 GPa at room temperature to ~7 GPa at 1000°C (Vickers hardness, 0.05 kg load, vaccum: 10^{-2} Pa) [72]. Compared to other common wear resistant hard coatings, alumina shows similar or lower hardness at room temperature but higher hot hardness (Fig. 3). For example at 600°C, the hardness of a CVD alumina coating is comparable to the hardness of a CVD TiC coating which is harder at lower temperature, but comparatively softer at temperatures above 800°C. At temperatures ranging from 0 – 1000°C, TiN CVD coatings tend to be slightly softer than alumina, while TiCN CVD coatings can be significantly harder than alumina at room temperature but their hot hardness is not reported [52].

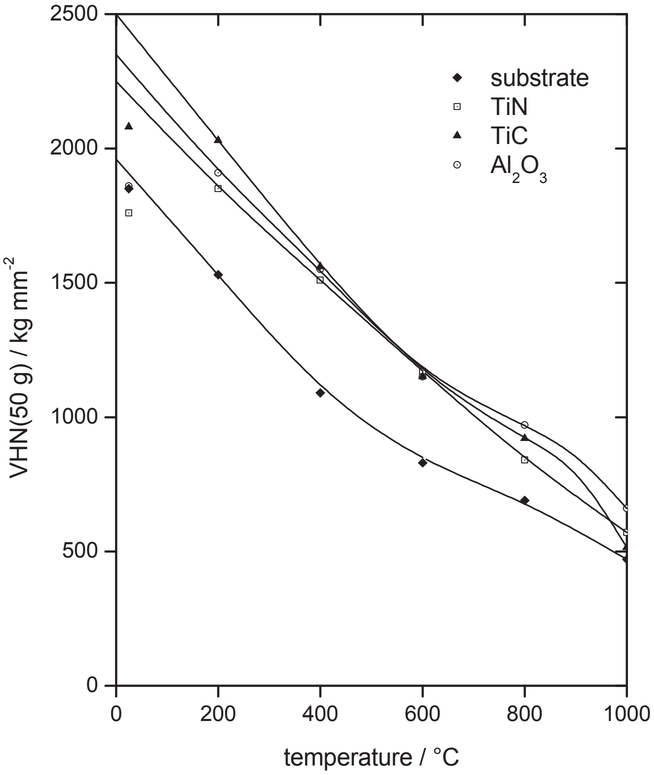

Fig. 3. Temperature influence on hardness of CVD coatings (TiN, TiC, Al_2O_3) compared to a cemented carbide substrate material (WC/Co) [72].

The hardness of α-Al_2O_3 and κ-Al_2O_3 is controversially discussed in literature, but measurements performed within the present thesis (Fig. 4) – showing a higher hardness for α-Al_2O_3 compared to κ-Al_2O_3 – are in good agreement with a recent publication [73]. One reason for ambiguous results within different studies is reported to be a confusion of “transformed κ-Al_2O_3” and “as-grown α-Al_2O_3”. Nevertheless, from the hardness point of view, a clear distinction of “transformed κ-Al_2O_3“ (i.e. α-Al_2O_3 present after a κ-α-transformation) and κ-Al_2O_3 is still missing [73, 74]. Another topic is the influence of coating texture on hardness, which is already suggested by the anisotropic behavior reported for bulk alumina [68] and plasma-sprayed alumina coatings [75]. Apparently, $(1\ 0\ \bar{1}\ 4)$ textured α-Al_2O_3 coatings show an increased hardness for certain deposition conditions, but it remains unclear whether a (0 0 0 1) texture causes a comparatively lower hardness value [76] or not [73]. Moreover, an investigation of the κ-Al_2O_3 hardness for different crystal orientations is not yet found in literature. However, compared to α-Al_2O_3 there is a lower resistance against cyclic loading reported for the κ-Al_2O_3 polymorph [77], but this study does not comment on different interface types and coating thicknesses for the investigated coatings. Within the same work, the similar behavior of a 1 µm grain-size α-Al_2O_3 (~6 µm thick) and a 4 µm grain-size α-Al_2O_3 (~8 µm thick) coating is remarkable.

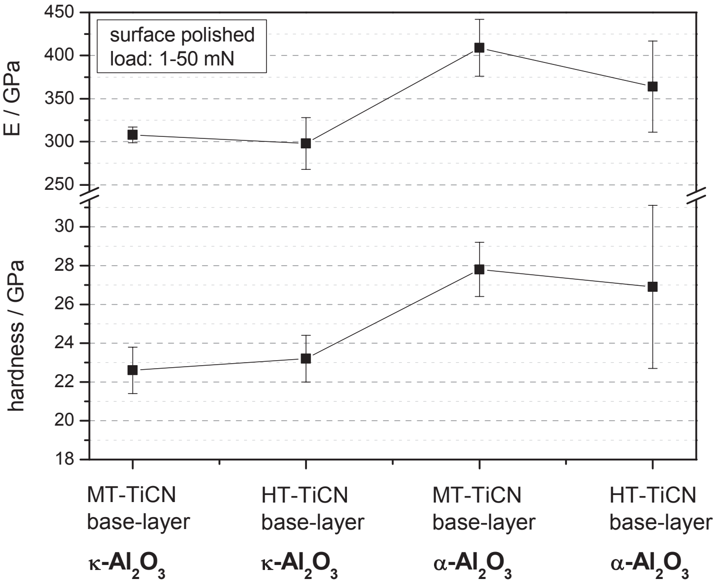

Fig. 4. Hardness measurements, performed at room temperature with a UMIS-II system, using fifty indents for each measurement of α-Al_2O_3 and κ-Al_2O_3 layers on different TiCN base-layers deposited at medium temperature (MT) and high temperature (HT).

2.3.4. Tribological properties

Friction – loss of energy* – and wear – loss of material* – are phenomena both arising from the same set of mechanisms, and the science describing both, these mechanisms and phenomena is called tribology. Distinguishing rolling and sliding is useful, but most rolling contacts contain at least small sliding components and the following focuses on the case of sliding. Listing the wear mechanisms shown in Fig. 5 is a very common approach, but still represents interdependent processes. Adhesion and abrasion are directly generating friction forces and all mechanisms may directly cause wear. Nevertheless, the occurrence of c) and/or d) would indirectly influence the friction. Abrasion is often divided into two-body- and three-body abrasive mechanisms, where the former is limited to asperity interaction and the latter includes hard particles located between the moving faces.

The friction behavior of engineering ceramics is affected by their low ductility which favors an elastic asperity contact (low energy dissipation, i.e. little contribution to friction), except at high temperatures. On the other hand, fracture occurring in the sliding contact might provide the possibility of energy dissipation and increase friction. Although adhesive forces are present, the high friction coefficient values (μ) of pure non-oxidized metals are not observed for ceramic-ceramic contacts which show typical friction values ranging from 0.25 to 0.8. The presence of gaseous or liquid water lowers the friction of oxide ceramics as they form hydrated surface layers. Hence, despite the general chemical inertness of ceramics, such tribochemical effects are responsible for the influence of different atmospheres on friction. Within a sliding contact, locally increased temperature as well as mechanical activation may accelerate surface reactions and film formation (lower μ) but also could remove adsorbed water and increase μ [78]. Additionally, higher temperatures favor plasticity which affects μ as the contact zone is not mainly elastic anymore. The influence of sliding speed on interfacial temperature and tribochemical processes is also considered to explain the huge variation of μ for some ceramics at different sliding speed (SiC, Si_3N_4, Al_2O_3, ZrO_2) [79], compared to the weak dependence of μ on sliding speed observed for metals [80].

---

* more precisely defined, for example [81]:

Friction is the resistance to motion which is experienced when one body moves tangentially over another with which it is in contact.

Wear is the removal of material from solid surfaces as a result of one contacting surface moving over another.

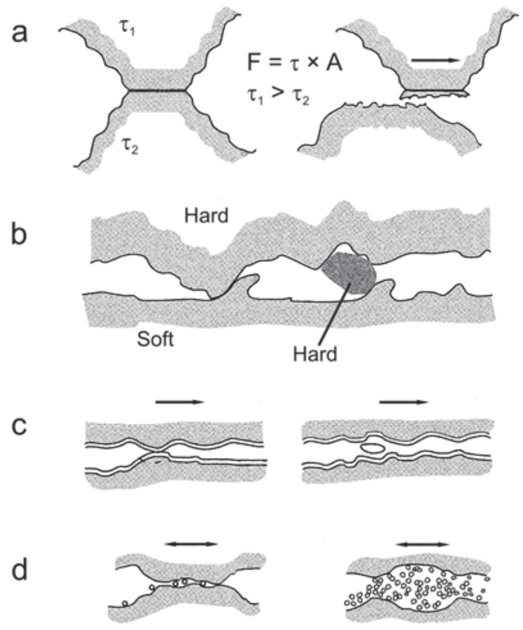

Fig. 5. Schematic presentation of wear mechanisms: adhesion (a), abrasion (b), fatigue failure (c) and chemical reation (c).

The wear behavior of engineering ceramics is also determined by their low plasticity and tribochemical processes. The latter are more relevant for ceramics than for metals, but wear phenomena might show more similarities between the sliding of ceramics and the sliding of metals than friction does. According to the discussion above, surface reactions and film formation also influence wear, but the tendency is not predetermined. Depending on factors like surface reaction velocities, stability of the tribochemical film and load, this processes either show protective character or material consuming character, i.e. lower or higher wear, respectively. Although the low plasticity of ceramics increases the chance for brittle fracture – and limits the structural application of ceramics – under sliding conditions a good performance is frequently observed. Apart from the temperature, the occurrence of plastic flow or brittle fracture also depends on the crystallographic orientation. For example, sliding on single crystals of Al_2O_3 parallel to prismatic planes in the c-axis direction leads to extensive fracture, whereas in other directions on these planes, or on the basal plane, it is accompanied by plastic flow [79]. Apart from film formation, water also influences the wear behavior as it increases the crack growth rate of some oxide ceramics (e.g. alumina), which fosters brittle fracture and severe wear. Additionally to this effect, the increased wear of alumina or zirconia in the presence of water is also attributed to an increased surface plasticity.

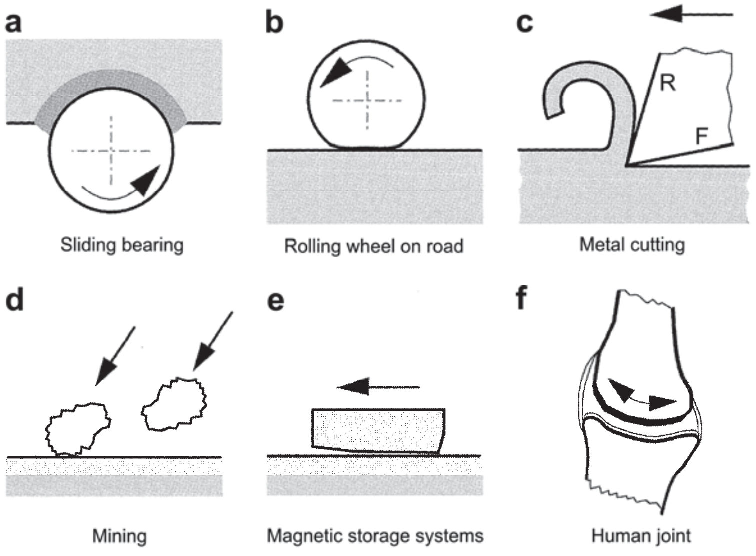

Fig. 6. Selected applications with different contact conditions in relative motion [81].

In spite of the low number of basic tribological mechanisms (cf. Fig. 5), their combinations cover a wide field of practical applications with very different characteristics, e.g. pointing out the huge difference between rolling and sliding contact. Fig. 6 presents an arbitrary selection of tribological systems, indicating the differences for systems which are mainly determined by sliding condition (Fig. 6a,c,e,f). For example, while a memory-disc/reading-head combination (Fig. 6e) does not deviate much from a standard pin-on-disc testing configuration, cutting definitely does (Fig. 6c). The latter combines two different sliding regimes, one at the rake face (label R, Fig. 6c) and one at the flank face (label F, Fig. 6c), separated by the cutting edge region. Temperature load, normal pressure and chemical attack are more severe at the rake face, while abrasion dominates at the flank face. During the cutting process, most of the heat is generated by the mechanical deformation of the chip. Hence, the higher temperatures at the rake face [82, 83] are caused by the higher temperature of the chip, compared to the workpiece material passing the cutting tool at the flank face. Additionally, the sliding of the chip on the rake face generates heat, the contact zone is bigger and the heat transfer is more efficient (normal pressures up to 1200 MPa) [81, 84]. Consequently, the hot chip – which is softer and less abrasive – could plastify [85] or solute [86] cutting tool surface material. For the same reason, the lower temperatures at the flank face are related to a harder workpiece material which rather abrades the cutting tool, in particular if a hard phase is present within the workpiece. Of course, friction, wear and the generated heat are influenced by cutting parameters like cutting speed, lubrication, feed rate, infeed rate and cutting geometry. For example, adhesive wear is often related to lower cutting speeds.

Coatings are a possibility to improve the performance of cutting tools by decreasing friction (less heat, lower cutting forces), abrasion (due to high coating hardness), adhesion and diffusion (higher chemical stability of the coating). These coatings must be adapted to the specific cutting application as well as to the utilized cutting tool substrate material. Hence, commercially cutting tools more often than not comprise a multilayer coating architecture, e.g. consisting of a bonding-layer [87, 88], a base-layer, a modification layer and a top-layer [1]. The sequence of materials, epitaxial interfaces, graded compositional transitions and adjusted layer thicknesses should provide optimal coating adhesion, hardness, toughness and chemical stability. However, a multilayer coated tool consequences an even more complex tribological system. For example, an alumina/TiCN coated turning tool [85] possesses an alumina surface first. But, for longer cutting times, two different layers of the coating system – alumina and TiCN – are simultaneously forming the contact area between workpiece material and cutting tool at the flank face. Even for severe cutting conditions, the temperature at the flank face is assumed to be lower than 900°C [85]. At these temperatures, alumina and TiCN show a comparable hardness (cf. Fig. 3). This means that abraded alumina particles will not cause severe damage in the TiCN and vice versa, which could improve the overall abrasive resistance. Compared to the flank face, the rake face of this coating system is reported to show lower wear (~50%) and the tribological behavior of the rake face is mainly determined by the alumina layer [85, 89]. Beneficially, the thermally insulating alumina layer (cf. Table 3) protects the tool against the high temperatures at the rake face. Nevertheless, due to the high temperature loads at the alumina surface, the main wear mechanism is reported to be plastification but not diffusion or dissolution wear. The latter are unlikely due to the low solubility of alumina within the workpiece material, in particular steel. Under these conditions, metastable κ-Al_2O_3 is likely to transform to stable α-Al_2O_3, but no crack formation is observed, which is attributed to the coating plasticity in combination with the high normal pressures [85, 89].

This example, presented from the coating point-of-view should point out the serious complexity of tribological processes involved in cutting. Considering further influences like the kind of cutting operation (e.g. drilling, turning, milling, …), cutting parameters (see above), the fine-geometry of the cutting edge, different workpiece material and its special condition (e.g. heat treatment, precipitations, inclusions, impurities, …) gives a huge number of different tribological contact situations, which is reflected by the extensive variety of commercial cutting tool products.

3. Coating synthesis

3.1. Chemical vapor deposition

The utilization of gaseous precursor materials, which are introduced into a reaction chamber, in order to synthesize a solid coating is called chemical vapor deposition (CVD). The necessary surface reaction usually is thermally activated, for example by high temperatures or by laser-assistance. The feed of less stable precursor compounds (e.g. metal-organic CVD) consequences chemical reactions which are activated at lower temperatures, but the widely used halide precursor gases are more stable and the deposition temperature often is in the range of 950 to 1150°C (thermal CVD). Further, deposition processes are distinguished, whether the reactor wall, the substrate and the gas mixture is heated (hot-wall CVD, the reactor wall is also coated) or if only the substrate is heated (cold-wall CVD) [45]. For the latter, the energy might be supported inductively, with laser or with microwave [90]. Apart from the deposition temperature, the deposition pressure plays a major role, as internal gas stream velocities (i.e. residence times) and boundary layer thickness (i.e. reactant diffusion to the substrate surface) are depending on pressure. Hence, pressure influences the homogeneity of the deposition process within the reactor, but also the supersaturation of the precursor gases is an important deposition parameter. Fig. 7 illustrates the basic steps involved in a CVD process. Concerning the surface reaction rate limits, “mass transport controlled” and “surface kinetics controlled” regimes are distinguished. The former describes the case where the diffusion from the laminar gas stream to the surface (via the gaseous boundary layer) occurs slower than the reaction of adsorbed species, and vice versa is valid for the latter. Fig. 8 displays the influence of deposition temperature and pressure on the heterogeneous deposition rate. Higher temperatures and lower pressures are suppressing the mass transport controlled regime, due to increased diffusion and decreased boundary layer thickness, respectively. Usually the surface kinetics controlled regime offers a more uniform deposition within the reactor, whereas fewer deposition processes might be operated in the mass transport controlled regime – aiming for maximized deposition rates. Eventually, deposition rates drop at still higher temperatures (e.g. close to the ordinate in Fig. 8) due to homogenous deposition, i.e. formation of solids within the gas stream and not at the substrate surface [24, 57].

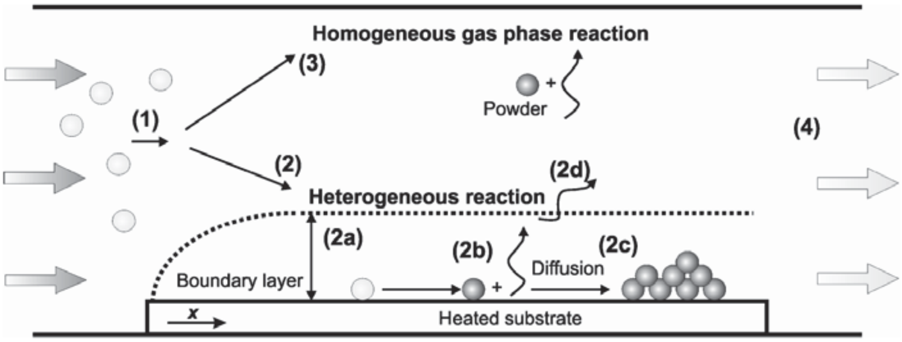

Fig. 7. Schematic illustration [91] of the basic process steps involved in CVD: gas feed (1), heterogeneous reaction (2), homogeneous reaction (3) and gas exhaust (4). The heterogeneous reaction comprises transport of the reactants through the boundary layer and adsorption (2a), chemical reactions at the substrate surface (2b), nucleation and growth (2c) and desorption of by-products (2d) [57, 92].

Thermal hot-wall CVD utilizing halide precursors was the first method for alumina coating deposition in the 1970-ies [2, 93]. A common precursor gas composition contained species like $AlCl_3$, CO_2, H_2 and the carrier gas species were chosen from Ar, N_2 or H_2. In the early 1990's, Fredriksson and Carlsson nicely reviewed the basics of alumina CVD [45]. Since then, investigating alumina structures and epitaxy, as well as the control of the polymorph [22, 94, 95], impurities [22, 35, 96], texture [7, 73, 76] and several doping/alloying approaches [8, 97-100] have been the matter of continuous and extensive research. Typical advantages of CVD are the high throwing power and the possibility of large batch sizes (e.g. several thousands of cutting tool inserts). The expression "throwing power" describes the ability of a coating technology to deposit at substrate regions which are not directly in the line-of-sight of the deposit's origin. That is, a high throwing power allows a more uniform film deposition at substrates with a complex shape (blind holes, undercuts, …).

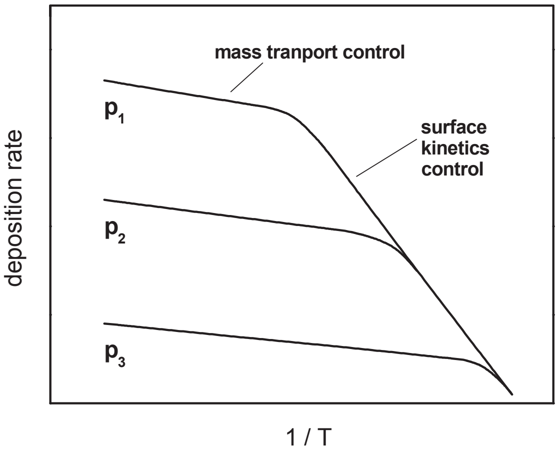

Fig. 8. Influence of deposition temperature and pressure on deposition rate: $p_1 < p_2 < p_3$ [92].

3.2. Alternative deposition methods

Considering the variations of CVD alumina processes [1, 45, 46, 101-104] with regard to the whole field of alumina coating deposition technologies reported today, reveals a predominant number of different plasma vapor deposition processes (PVD) [105-114]. Compared to CVD, these processes offer the possibility for lower deposition temperatures, sharper cutting edges and higher deposition rates [115, 116]. Several coating materials are harder when deposited by PVD, but hardness converges at temperature in the range of 1000°C [117]. Furthermore, PVD coatings possess considerable compressive residual stresses which enable crack stopping, while in CVD coatings often moderate tensile residual stresses occur, which are accompanied by the formation of a thermal crack network (depending on the thermal mismatch). The fact, that this intensive research on PVD alumina did not consequence commercially available PVD α-Al_2O_3 coatings indicates process restrictions [118]. Up to now, low deposition temperatures in the range of 500°C – a major advantage of PVD – did not result in competitive alumina coatings. On the other hand, increased temperatures (> 700°C) improved alumina properties but ruled out more temperature sensitive substrates like high speed steel. To sum up, a PVD alumina coating with superior performance is not reported yet. Nevertheless, the rapid evolution of PVD processes consequences new layouts like high power impulse magnetron sputtering (HIPIMS) [118] and also the adaption of existing methods like atomic layer deposition [119] enables new possibilities for alumina deposition. For HIPIMS the possibility of introducing high energies (ion bombardment) at the substrate surface is likely to be a key parameter for depositing α-Al_2O_3 [118] but also potentially decreases crystallinity and hence coating performance [120]. Assuming such an energy threshold necessary for a sufficient α-Al_2O_3 quality leads to the speculative question, if it could be overcome by ion bombardment without destroying the crystallinity. Nevertheless, HIPIMS technologies also possess a better throwing power than their conventional predecessors [121]. Alternatively, γ-Al_2O_3 is reported to be a suitable alumina modification [122] which is easier to synthesize at lower deposition temperatures [114, 120]. Indicators for the performance of state-of-the-art PVD γ-Al_2O_3 coatings are reported high hardness [106], specific cutting tests [105] and stability during heat treatments [123, 124].

In addition to CVD and PVD, plasma assisted chemical vapor deposition processes (PACVD, also denoted as plasma enhanced chemical vapor deposition: PECVD) are reported [125-128] This technology represents an intermediate approach where the use of gaseous precursors is combined with thermal and plasma activation. However, the increased substrate temperature of reactive PVD processes and misleading nomenclature [129] cause a vague distinction of PVD and PACVD. Moreover, no recent publications are found for PACVD, although the restart of research activities is rumored [130].

With regard to the optimization of a whole coating system (cf. section 2.3.4), often an impressive diversity of different layers are composed to a multilayer stack. For future coating systems, one further advantage of CVD might be its flexibility [120]. For example, a PVD reactor limits the number of different sublayer types in terms of different alloying elements, as each layer which contains new elements will need one target and will consume a fraction of the reactor chamber surface. In particular on production-scale, if higher deposition rates should be achieved, each new layer will need several targets. This restriction might be less valid for layers where sufficient rates can be achieved by only one or two targets and for metal-organic reactive PVD.

3.3. Variations of CVD conditions

Generally, deposition temperature, total pressure, flow rate and gas composition (supersaturation) are the main parameters of CVD [102, 131-133] (cf. section 3.1) and they must be adapted for each specific deposition. For example, there are trade-offs concerning desired coating growth rate and coating quality, as a fast grown layer often possesses a lower thickness homogeneity or coating density [21, 45]. Temperature and pressure must also be optimized with regard to the specific precursor gas mixture and investigations are published within the wide range of 200 – 1800°C and 67 – 1013 mbar [45]. If lower deposition temperatures are necessary, CVD processes which apply metal-organic precursors allow sufficient deposition rates. But also minor changes to the gas mixture, like the use of bromide or iodide instead of aluminum chloride [96, 103] are reported to affect impurity sensitivity and uniformity of the deposition process. Particularly, control of impurities turned out to be decisive during alumina deposition [22, 35, 96]. Also the supersaturation of the precursor gases determines the alumina deposition process. For example, it is an important parameter during the nucleation step as it is correlated to nucleation density and consequently influences the coating morphology [2, 134]. Furthermore, different bonding- and base-layers offer the possibility to influence the nucleation conditions for an alumina layer [45, 87, 88]. Another possible variation is the addition of new precursors to the deposition gas mixture. As a prominent example, H_2S addition increases deposition rate and coating thickness homogeneity, while almost no sulfur is incorporated [1, 21, 99]. Other species might be added, in order to dope or alloy the alumina CVD coating and improve its properties. However, such developments are not straightforward. The main difficulty seems to be the ensemble of many homogeneous and heterogeneous chemical reactions [135, 136], which makes the prediction and control of additional reactions for additional precursor gases demanding.

3.3.1. Effect of deposition atmosphere

For CVD of alumina, aluminum chloride is the commonly used aluminum donor and due to the deliquescence nature of $AlCl_3$, in-situ generation at 250 – 400°C with metallic aluminum and HCl or Cl_2 is preferred. Possible oxygen donors are CO_2, H_2O, N_2O, O_2 and alcohols. The reaction of $AlCl_3$ with O_2 is slow but a recent study presented reasonable deposition rates at atmospheric pressure [137]. The reaction of $AlCl_3$ with H_2O is much faster but deposition rates are decreasing with increasing temperature [93] (reaction 1). Aluminum chloride hydrolysis with H_2 and CO_2 runs at a medium rate (reaction 2) and possesses several advantages. For this reaction, water is in-situ generated by the “water gas shift reaction” (reaction 3), which was also separately studied [138].

$$2\ AlCl_3(g) + 3\ H_2O(g) \leftrightarrow Al_2O_3(s) + 6\ HCl(g) \tag{1}$$

$$2\ AlCl_3(g) + 3\ CO_2(g) + 3\ H_2(g) \leftrightarrow Al_2O_3(s) + 3\ CO(g) + 6\ HCl(g) \tag{2}$$

$$CO_2(g) + H_2(g) \leftrightarrow H_2O(g) + CO(g) \tag{3}$$

The gas mixture of carbon dioxide and hydrogen acts as a “water reservoir” which extends the alumina deposition zone and improves process controllability. For somewhat lower deposition rates, the addition of HCl or CO further extends the alumina deposition zone. Hence, reaction 2 is more often than not preferred to reaction 1. Additionally, reaction 1 rather would be suitable for lower deposition temperatures, which are unfavorable related to incorporation of water and chlorine within the deposited alumina layer below 550°C and 800°C, respectively. [45]

Argon, hydrogen, nitrogen and their mixtures are common carrier gases for alumina CVD processes. Basic influences of different carrier gas compositions are the diffusivity of the precursor species within the carrier gas and the manner of gaseous flow itself. For example, the type of carrier gas might influence the diffusion time of a precursor molecule through the gaseous boundary layer adjacent to the substrate surface, but also the thickness of this boundary layer. Hence, residence times of different precursor species depend on the kind of diluting gas. Consequently, also the contributions of homogeneous and heterogeneous reactions might be influenced. Additionally, different carrier gases might affect the formation of intermediate species during the deposition process, as some of these intermediate species contain e.g. hydrogen [135, 139]. An increased amount of hydrogen is reported to increase the alumina deposition rate [140, 141] and laboratory-scale experiments [142, 143] performed within this thesis confirmed this. These laboratory-scale experiments also showed a slight but significant increase in hardness (~15%) for alumina deposited with hydrogen carrier gas. The role of argon and nitrogen might be simplified as non-reactive and less diffusive replacement of hydrogen.

Thermodynamic calculations for alumina deposition [46, 103, 133, 134] showed a smaller influence of deposition temperature and pressure (-150…1300°C, 70…500 mbar) compared to the composition of the gas mixture. There, characteristic values are the partial pressure ratio of hydrogen and carbon dioxide or the aluminum chloride partial pressure. High alumina yields are reported for $p(H_2) / p(CO_2)$ close to one [144]. High carbon dioxide concentrations hold the danger of oxidation of the substrate or any interlayer. Furthermore, calculations would suggest the co-deposition of free carbon for high hydrogen concentrations. The latter was not found for the deposition runs performed within this thesis nor reported in experimental studies. Only for deposition conditions where calculations suggest a high amount of co-deposited carbon, small carbon contents were detected. This deviation between experiment and thermodynamic calculation is attributed to slow carbon forming reactions. On the other hand, the increased alumina deposition rate for increased hydrogen amount is found experimentally and calculations [135] relate it to a more pronounced $AlCl_3$ decomposition. These more recent calculations are dealing with a radical chain reaction mechanism, including more than 30 species and more than 100 reversible chemical gas phase reactions. They also predict the experimentally observed retarding effect for relatively high HCl additions [141], but could not clarify the influence of CO. Furthermore, the water gas shift reaction appears to be unimportant within this kinetic model, but three coupled reactions are water forming:

$$AlO + H_2 \leftrightarrow Al + H_2O \qquad (4)$$

$$H_2 + OH \leftrightarrow H_2O + H \qquad (5)$$

$$HCl + OH \leftrightarrow H_2O + Cl \qquad (6)$$

Based on the radical chain reaction mechanism, a further developed approach [145] considered the water gas shift reaction to be important. For this simulation, this reaction was found to start slowly, but speed up with increasing residence time as it was catalyzed by in-situ formed gaseous AlOCl. In parallel, a combined thermodynamic and kinetic approach was performed, which took into account homogeneous and heterogeneous chemical reactions [139]. However, these calculations include the water gas shift reaction a priori, but neglect gaseous AlOCl. They suggest that CVD of alumina is far from thermodynamic equilibrium, i.e. for most of the major species partial equilibrium is reached only after comparatively long residence times.

So far, thermodynamic chemical calculations could only offer guidelines for deposition process conditions, but suffer from a lack of predictive power. More useful kinetic chemical calculations are yet performed only for gas phase reactions; hence do not consider the whole deposition process. Nevertheless, simulations reveal a highly interdependent system of chemical reactions. While there are good partial results achieved by applying a kinetic approach, there is a lack of kinetic data and several possible chemical reactions must be neglected. Consequently, today's kinetic models do not allow a comprehensive simulation of CVD processes.

3.3.2. Effect of substrate

Beside the addition of gaseous nucleation modifiers (e.g. $TiCl_4$ or $ZrCl_4$), the kind of substrate surface is decisive for the nucleation process and often predetermines the growth period, i.e. the whole alumina layer. Also the crystal structure depends on the nucleation process because of the polymorphous nature of alumina. Furthermore, coating properties like adhesion and texture are influenced by this step [7, 146, 147]. Obviously for the former effects, this step is crucial, while the latter could also be manipulated during the further growth of the alumina coating [148]. Important substrate properties are crystallinity, lattice faults, roughness, and chemical homogeneity of the surface. For example, alumina nuclei are non-uniformly distributed when deposition is directly started on cemented carbide (different phases are forming the surface) but much more evenly distributed if a TiC base-layer is applied [45]. Common ways of substrate surface modification are etching, manipulation of the adsorbed layer at the substrate surface and the deposition of rather thin modification- or bonding-layers. Etching of a TiC base-layer is a reported modification step prior to alumina deposition [23] where already formed titanium oxide [94, 149] is removed from the surface. This process allows the preferred growth of κ-Al_2O_3 on TiC, while α-Al_2O_3 occurs as long as titanium oxide is present. Consequently, titanium oxide containing bonding-layers are utilized in order to stabilize the α-Al_2O_3 modification [87, 88]. This effect is explained by orientation relationships observed for α-Al_2O_3 and Ti_2O_3 [150]. Special modification layers with different balances of their metal constituents (titanium, aluminum) are also reported to allow the control of α-Al_2O_3 or κ-Al_2O_3 growth [6, 95]. These effects are often related to epitaxial relationships which have been investigated for alumina and TiN or TiC [5, 61, 147, 151, 152]. However, no difference between α-, κ- and θ-Al_2O_3 polymorphs and TiC or TiN, regarding interfacial atomic arrangement, was found [45]. Moreover, studies which include the thin bonding-layer are rare and epitaxial relationships between base-layer, bonding-layer and alumina layer are sometimes observed [87], but sometimes they are not found [153]. One explanation for difficult to observe epitaxial relationships is the ratio of grain sizes at the interface, i.e. one alumina grain often covers several of the finer base-layer or bonding-layer grains, which could impede transmission electron microscopy imaging. Nevertheless, similar orientation relationships between grain columns were found for alumina multilayers [147], which suggests that the alumina texture could to be influenced by the layers underneath and the substrate material. On the other hand, alumina is reported to nucleate randomly orientated on CVD TiN-coated cemented carbide, while the finally grown α-Al_2O_3 layer might possesses a $(1\ 0\ \overline{1}\ 4)$ and $(1\ 1\ \overline{2}\ 6)$ texture [134]. In another investigation, a more pronounced $(1\ 0\ \overline{1}\ 4)$ α-Al_2O_3 texture with increasing deposition temperature (TiN-coated cemented carbide, 950°C – 1100°C) was found, but the authors did not characterize the early alumina growth period [133]. Furthermore, varying the oxidation potential of the deposition atmosphere during the alumina nucleation is reported to allow texture control [7]. But also within this study, the $(1\ 0\ \overline{1}\ 4)$ orientation shows the best wear resistance, which could lead to the speculative question, if only a down-grade in performance is possible with “control activities” during the nucleation step.

Within this thesis, different TiCN base-layers consequenced a change in texture for α-Al_2O_3 or κ-Al_2O_3 coatings, while the alumina deposition conditions remained constant (Table 5). This could be explained by the different texture on MT-TiCN [154] and HT-TiCN [155] but the κ-Al_2O_3 texture seems to be less influenced and texture coefficients are more extreme on the MT-TiCN base-layer.

Table 5

Texture coefficients [156] for α- and κ-Al_2O_3 on MT-TiCN and HT-TiCN base-layers. Bold numbers indicate the most pronounced orientations.

Lattice plane (hkl)	α-Al_2O_3 MT-TiCN	α-Al_2O_3 HT-TiCN	Lattice plane (hkl)	κ-Al_2O_3 MT-TiCN	κ-Al_2O_3 HT-TiCN
(012)	1.29	0.54	(112)	0.14	0.80
(104)	0.41	0.63	(013)	1.14	1.42
(110)	0.30	**1.98**	(122)	0.06	0.58
(113)	1.27	0.90	(004)	**2.79**	1.40
(024)	0.16	1.27	(132)	0.11	0.57
(116)	0.81	0.34	(015)	**1.99**	**1.69**
(214)	1.18	**1.74**	(134)	0.87	0.73
(300)	**2.60**	0.60	(135)	0.89	0.81

3.4. Doping and alloying of CVD alumina

The addition of a further element, in order to alter the properties of the matrix material, is an ancient alchemic approach. Although a lot of the applied methods have been enormously improved and many have been newly developed, this approach still contains a considerable empiric component. Dopants and impurities have an influence on the defect chemistry of alumina and consequently alter the diffusion processes within this material. Hence, high-temperature properties like plastification or creep resistance are different for doped and undoped alumina [157]. The presence of additional elements during the CVD synthesis of alumina also could influence the stability of different alumina polymorphs or their transformation. For example, silicon is reported to stabilize the α-Al_2O_3 polymorph and favor the κ-α-transformation [36, 146].

3.4.1. Element selection

Scientific improvement approaches concerning the doping and alloying of wear resistant hard coatings mostly aim for improved tribological properties. For example, increased coating hardness and the possibility of reducing friction forces are often desired (cf. section 2.3.4). At the same time, doping and alloying of alumina rather decreases its chemical stability (cf. section 2.3.1) [48, 49, 158] and therefore must be implemented carefully. The generally low solubility limits of dopants within alumina (see Table 2) further restricts these approaches and doping often results in multiphase coatings (see Publication I and II). A straightforward approach is the addition of a second phase which shows e.g. higher hardness or low-friction effects. Furthermore, additional elements can be introduced in order to alter the coating morphology via co-deposition (e.g. segregation and renucleation) or via influencing the nucleation behavior and the surface reactions (i.e. conditions for coating growth). Related to the complex chemistry of CVD, experimental knowledge is of vital importance as basic consideration and simulations (necessarily simplified) often fail to give a good prediction. With regard to this background, this thesis partly focused on a doping approach basing on the utilization of already available precursors on production-scale CVD systems. For these precursors ($TiCl_4$, BCl_3, CH_4) also the handling was solved. A second, more fundamental approach investigated different precursors, feed methods and doping influences for less common doping elements (Y, Cr, Sn, Nb, Sr, Ta, Si, Mn). These results are summarized by two diploma theses [142, 143] and not shown in this ph.d. thesis

3.4.2. Titanium doping

The influence of titanium doping on alumina properties has been investigated in the early 1980’s (e.g. [159]), but only recently detailed experimental microstructural studies were published [160]. For example, the enhanced densification during sintering of titanium doped alumina is related to an anisotropic relation of titanium and alumina (caused by an anisotropic segregation of titanium [33]). A disadvantage of such a titanium doped alumina could be higher creep rates and diffusivity, when compared to undoped alumina. For alumina-titania coatings prepared by different methods, titania addition is reported to influence residual stress, scratch resistance, electrical- and optical properties [161, 162] and porosity [163]. For thermal CVD alumina, an increased growth rate, different as-deposited phase stability and altered residual stresses are found for titanium doped κ-Al_2O_3 [8]. For the α-Al_2O_3 / Ti_3O_5

coatings deposited within the present thesis (Publication I), titanium oxide offers lower high temperature friction (~0.4) compared to the undoped coating (~0.8). For other deposition technologies like plasma spraying, this improvement is not reported although the coatings are of similar composition [164].

The simultaneous addition of $TiCl_4$ and CH_4 to a thermal alumina CVD process was aiming for the co-deposition of Al_2O_3 and TiC, but titania formation could hardly be suppressed [165]. Nevertheless, a graded coating composition – i.e. decreasing titanium content with proceeding deposition time – was presented to be a promising approach for improved alumina adhesion on TiC base-layers. Combined titanium boron doping significantly increased the thermal stability of κ-Al_2O_3, i.e. retarded the κ-α-transformation (Publication IV). Additionally, this coating is a more effective diffusion barrier when compared to undoped κ-Al_2O_3. Moreover, the κ-Al_2O_3 seems to exhibit a higher solubility limit for titanium and for boron than the α-Al_2O_3.

For bulk alumina, a surface treatment combining titanium monoxide deposition with a subsequent heat treatment [66] causes diffusion of titanium into alumina and is reported to increase hardness if optimal conditions are chosen. Heat treatment temperatures below 900°C could not provide sufficient titanium diffusion. Heat treatments above 1300°C (and times longer than two hours, in air) resulted in a two-phase region close to the surface. This Al_2O_3-TiO_2 mixture possesses a lower hardness, which is also observed for two-phase CVD coatings (α-Al_2O_3 / Ti_3O_5, Fig. 9) deposited within this thesis (Publication I). A decline in mechanical properties is also observed after the formation of TiO_2 during the heat treatment of titanium implanted alumina, but toughness increases simultaneously [67, 166]. For this material, recovery processes depend on the heat treatment atmosphere and usually start at the aluminum sub-lattice and continue at the oxygen sub-lattice.

For titanium doping, the kind of atmosphere (e.g. reducing or oxidizing) seems to have a decisive influence. For example, titanium doped alumina might be an ionic conductor at high oxygen partial pressures $p(O_2)$ and an electric conductor at low $p(O_2)$. For alumina which contains TiO_2 precipitates, different CO/CO_2 mixtures (i.e. different $p(O_2)$) changed Ti^{4+} concentrations and transport properties [44].

These defect chemistry mechanisms are basing on different defect energies for varying synthesis conditions like $p(O_2)$. Oxidizing conditions favor the formation of substitutional Ti^{4+} ions, while substitutional Ti^{3+} ions show lower defect energy under reducing conditions [34, 157, 167]. Related to these changed conditions, titanium doped alumina exhibits different

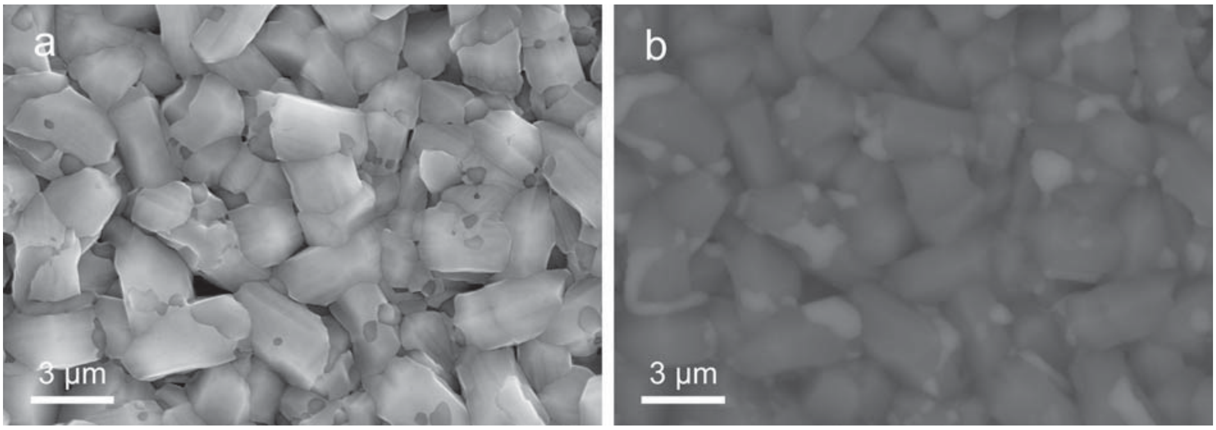

Fig. 9. SEM secondary electron (a) and backscattered electron (b) top-view images of an as-deposited α-Al_2O_3 / Ti_3O_5 coating with a titanium content of ~4.2 at.%. The right micrograph displays the bright titanium oxide phase (for experimental details: see Publication I).

mechanical properties depending on the charge state of titanium (e.g. higher yield stress for Ti^{4+}- than for Ti^{3+}-doped alumina). Furthermore, the dependence of titania precipitation on ageing atmosphere [168] is also explained with altered titanium ion charge within the alumina lattice.

The observed unexpected behavior of titanium doped alumina, like increased chemical diffusion with decreasing temperature from 1520 to 1350°C is attributed to short circuit diffusion in connection with TiO_2 precipitation [44].

3.4.3. Boron doping

Compared to the amount of literature available for titanium doping, there are very few publications available concerning boron doping. Usually they are related to the semiconductor- and electronic devices industry, e.g. boron doping of diamond films [169] or silicon germanium films [170]. Nevertheless, in the field of wear resistant hard coatings for cutting tools, boron doping might be of greater importance than titanium doping is.

Comparable to the chemical investigations for CVD alumina deposition, there are some studies dealing with boria (B_2O_3) deposition [171-173]. Similar to the behavior of aluminum halides, boron halides (BCl_3, BBr_3) slowly react with oxygen, but even for low temperatures immediately form boria, if water vapor is present. A thermodynamic comparison of boron hydrides and boron halides reveal milder, more favorable deposition conditions for the latter [174]. However, no fundamental investigation considering the simultaneous CVD reaction of aluminum and boron containing precursors with an oxygen donor was found.

Experimental studies concerning oxide phases which contain aluminum and boron frequently report on aluminum borate (e.g. $Al_4B_2O_9$, $Al_{20}B_4O_{36}$), for example synthesized by heating powders of B, B_2O_3 and Al_2O_3 or by CVD [175, 176]. Beneficial properties of this refractory material are high Young's modulus, high strength, good chemical stability and low coefficient of thermal expansion (CTE). Most studies consider its application for oxidation resistant whiskers which could be used for reinforcing ceramic materials or within metal matrix composites [177, 178] A recently suggested application of a boria-alumina mixed oxide are catalyst supports [179].

Within this work, the influence of boron doping on CVD of alumina was studied in detail. Publication II investigates the influence of boron doping on CVD α-Al_2O_3, for different precursor gas mixtures and deposition temperatures. It was found that boron incorporation within α-Al_2O_3 is almost impossible at ~1000°C deposition temperature, but can be done at lower temperatures. In these cases, boron incorporation always is accompanied by the formation of aluminum borate which causes a lower coating hardness and a lower wear resistance. For boron doped α-Al_2O_3 deposited at ~1000°C a slightly increased coating hardness was observed. The influence of boron doping was also examined for κ-Al_2O_3 coatings, where it improved thermal stability and reduced diffusion through the κ-Al_2O_3 layer (Publication IV). Compared to the undoped coating, this improvement was significant and it was just slightly below the level of the combined titanium boron doped coating. This effect on phase stability is contrary to other doping experiments (cf. section 3.4, silicon doping) and contributes to the investigation of the κ-α-transformation, where mainly the occurrence of free surface in combination with high temperatures was considered so far [180-183], but also the influence of compressive stresses during cutting has to be taken into account [85].

3.4.4. Carbon doping

The incorporation of carbon within CVD alumina layers was discussed relatively early, during the fundamental investigation of deposition parameter variations (cf. section 3.3.1). Later on, the co-deposition of carbon by adding methane or carbon disulphide to the precursor gas mixture was reported to consequence a pronounced grain refinement for CVD alumina coatings [97, 184]. It was found that carbon disturbs the regular alumina growth and SIMS measurements show the formation of carbon particles in the deposited layer, which are also suggested to be arranged as a "carbon network" [37]. With the same method, no carbides were detected and heterogeneous nucleation of alumina seems to be impossible on amorphous carbon [184]. Furthermore, it is reported, that methane stabilizes κ-Al_2O_3 if the $AlCl_3$-CO_2-H_2 precursor system is used [165], which likely is related to an affected nucleation step (see section 3.3.2). For these coatings, the deposition of a compact alumina layer directly onto cemented carbide is possible without whisker formation. High methane concentrations cause a very fine grain size of alumina, but increase layer porosity and decrease growth rate. The combination of high methane concentration and increased flow rates allow the deposition of a uniform, compact, extremely fine grained alumina [97].

Alternatively, also the utilization of a metallorganic precursor (aluminum acetylacetonate) precursor allows the deposition of well adhering α-Al_2O_3+C layer directly on cemented carbide, without the prior deposition of a base-layer. Results within this study indicate that carbon impedes surface and bulk diffusion which may increase the number of nucleation sites [140]. For an increased aluminum acetylacetonate concentration, homogeneous nucleation was observed.

For the α-Al_2O_3 coatings deposited within the present work, there was only little carbon co-deposited, but surface segregation of carbon was clearly increased (Publication III). Differently from the laboratory-scale experiments mentioned above, these deposition runs were conducted in an industrial-scale production plant. This is connected to different controllable ranges of several deposition parameters, for instance the residence time of the gases. Furthermore, the deposition of alumina was started on an α-promoting bonding-layer and methane addition started only after an initial deposition of undoped α-Al_2O_3. This later introduction of methane might limit its effect, since its addition to an already ongoing ensemble of chemical reactions and adsorbed species is expected to be less influential than the start of this whole ensemble with an additional precursor.

The most significant improvement, observed for methane addition, was a reduction of the friction coefficient at room temperature as well as at high temperature (Fig. 10). Related to CVD alumina deposited on cemented carbide, this behavior was not reported so far.

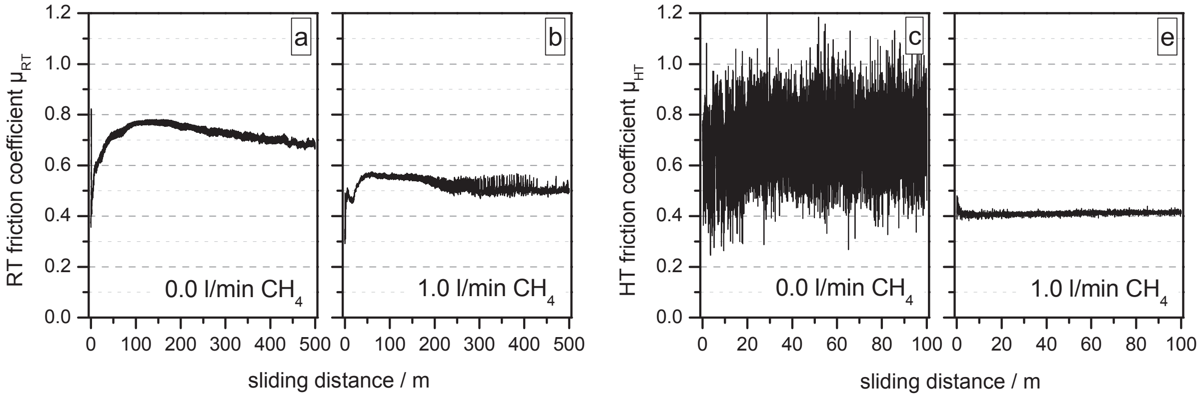

Fig. 10. Friction coefficient curves determined with a ball-on-disc test at room temperature (a, b) and at 700°C testing temperature (c, d). In both cases, the addition of methane during alumina deposition decreased the friction coefficient (b, d) compared to the undoped alumina coating (a, c). For experimental details see Publication III.

4. Summary

The present thesis investigates the doping of CVD alumina coatings for cemented carbide cutting tools on production-scale deposition units. Three dopants (titanium, boron and carbon), two base-layers (medium-temperature [MT] and high-temperature [HT] TiCN) and two alumina polymorphs (α-Al_2O_3 and κ-Al_2O_3) were considered.

Several fundamental properties of alumina came into focus:

- Because of the low density of intrinsic lattice defects in alumina, already low amounts of dopants or background impurities have a significant influence on alumina properties. Analytical detection of these low concentrations often makes a clear correlation of chemical composition and properties difficult.
- After decades of research, self-diffusion of alumina and diffusion processes within alumina are not consistently described.
- Doping is already reported to increase the creep resistance of alumina, because the segregation of some doping elements impedes dislocation movement at grain boundaries. As grain boundary slip also affects mechanical properties at high temperatures, doping with similar, segregating elements could improve mechanical properties and increase the resistance against plastification at the rake face of the cutting tool. This mechanism could be applied for α-Al_2O_3 and κ-Al_2O_3 coatings.

Doped α-Al_2O_3 coatings showed tribological improvements and a slightly increased hardness. For doped κ-Al_2O_3, a beneficially retarded κ-α-transformation and a slower diffusion of substrate elements through the alumina layer were observed. Furthermore, κ-Al_2O_3 seems to possess higher solubility limits for titanium and boron than α-Al_2O_3. Considering the increased thermal stability of doped κ-Al_2O_3, it seems to be possible to improve its ability for high speed cutting applications, where the lower thermal conductivity and the slightly better matched coefficient of thermal expansion (CTE) of κ-Al_2O_3 to cemented carbide substrate could be beneficial. However, theoretical benefits form the CTE point-of-view might not be realized without adaptation of the base-layer. The investigation of different base-layers confirmed the decisive influence reported for the substrate surface which is present during the alumina nucleation step.

Within the present work, the alumina was nucleated in undoped condition, but the introduction of the dopant precursor already during the nucleation of the alumina layer is assumed to offer a huge potential for influencing the subsequently growing alumina layer. At the same time, such an influence might bear the danger of drastically changed coating properties.

CVD of alumina involves a huge ensemble of chemical reactions, where already small amounts of additional gases could change alumina properties, even if no dopant incorporation is detected. Also the adaptation of deposition conditions in order to optimize the doping process is not straightforward, as the behavior of this ensemble of chemical reactions hardly can be predicted. Moreover, varied deposition conditions often change the “history” of the substrates, which will finally be coated by the layer of interest (i.e., the intentionally varied part). For example, a variation of the alumina deposition temperature could be related to different periods of cooling/heating which will influence the otherwise constantly deposited base-layer. Consequently, the crucial nucleation of the alumina layer might not only be influenced by the variation of alumina deposition conditions.

Promising approaches for further improved alumina properties arising from the present thesis are the adjustment of oxidation potential in accordance with the applied doping element and the utilization of dopant segregation at grain boundaries in order to hinder plastification.

5. Abbreviations and symbols

CC	cemented carbide, e.g. WC/Co
CTE	coefficient of thermal expansion
CVD	chemical vapor deposition
HIPIMS	high power impulse magnetron sputtering
HT-TiCN	titanium carbon nitride base-layer deposited at high temperature
λ_{273}	thermal conductivity at a temperature of 273 K
λ_T	thermal conductivity at a certain temperature range
μ	friction coefficient
MT-TiCN	titanium carbon nitride base-layer deposited at medium temperature
p	pressure
$p(X)$	partial pressure for the gaseous species X
PACVD	plasma assisted chemical vapor deposition = PECVD
PECVD	plasma enhanced chemical vapor deposition = PACVD
PVD	physical vapor deposition
SEM	scanning electron microscopy
UMIS-II	ultra-microhardness indentation system, second generation

6. Literature

[1] S. Ruppi, J. Phys. IV 11/3 (2001) 847.

[2] M. Kornmann, H. Schachner, R. Funk, B. Lux, J. Cryst. Growth 28/2 (1975) 259.

[3] C. Bjormander, Surf. Coat. Technol. 201/7 (2006) 4032.

[4] M. Pulver, W. Nemetz, G. Wahl, Surf. Coat. Technol. 125/1-3 (2000) 400.

[5] M. Halvarsson, S. Vuorinen, Int. J. Refract. Met. Hard Mater. 15/1-3 (1997) 169.

[6] M. Halvarsson, S. Vuorinen, H. Norden, Mat. Res. Soc. Symp. Proc., 1993, p. 83.

[7] S. Ruppi, Int. J. Refract. Met. Hard Mater. 23/4-6 (2005) 306.

[8] M. Kathrein, W. Schintlmeister, W. Wallgram, U. Schleinkofer, Surf. Coat. Technol. 163-164 (2003) 181.

[9] I. Levin, D. Brandon, J. Am. Ceram. Soc. 81/8 (1998) 1995.

[10] H.A. Wriedt, in: T.B. Massalski (Ed.), Binary Alloy Phase Diagramms, ASM Metals Park, OH, 1985, p. 185.

[11] A. Petzold, Aluminiumoxid: Rohstoff, Werkstoff, Werkstoffkomponente, Deutscher Verlag für Grundstoffindustrie, Leipzig, 1991.

[12] G.W. Brindley, J.O. Choe, Am. Miner. 46/7-8 (1961) 771.

[13] L. Pauling, S.B. Hendricks, J. Am. Chem. Soc. 47 (1925) 781.

[14] H.L. Gross, W. Mader, Chem. Commun. 1 (1997) 55.

[15] G. Paglia, A.L. Rohl, C.E. Buckley, J.D. Gale, J. Mater. Chem. 11/12 (2001) 3310.

[16] C. Ruberto, Y. Yourdshahyan, B.I. Lundqvist, Phys. Rev. B 67/19 (2003) 18.

[17] Y. Yourdshahyan, C. Ruberto, M. Halvarsson, L. Bengtsson, V. Langer, B.I. Lundqvist, S. Ruppi, U. Rolander, J. Am. Ceram. Soc. 82/6 (1999) 1365.

[18] J.H. Harding, K.J.W. Atkinson, R.W. Grimes, J. Am. Ceram. Soc. 86/4 (2003) 554.

[19] A.H. Heuer, J. European Ceram. Soc. 28/7 (2008) 1495.

[20] A. Larsson, S. Ruppi, Int. J. Refract. Met. Hard Mater. 19/4-6 (2001) 515.

[21] S. Ruppi, A. Larsson, Thin Solid Films 388/1-2 (2001) 50.

[22] E. Fredriksson, J.-O. Carlsson, Surf. Coat. Technol. 56/2 (1993) 165.

[23] M. Danzinger, R. Haubner, B. Lux, J. Phys. II 1/C2 (1991) 579.

[24] H.O. Pierson, Handbook of Chemical Vapor Deposition (CVD), Noyes Publ., Park Ridge, New Jersey, 1999.

[25] H. Holleck, J. Vac. Sci. Technol. 4/6 (1986) 2661.

[26] http://www.webelements.com/, 2009 October 20

[27] L. Fornasiero, E. Mix, V. Peters, K. Petermann, G. Huber, Ceram. Int. 26/6 (2000) 589.

[28] W.Y. Ching, Y.N. Xu, M. Ruhle, J. Am. Ceram. Soc. 80/12 (1997) 3199.

[29] K.P.D. Lagerlöf, R.W. Grimes, Acta Mater. 46/16 (1998) 5689.

[30] E.M. Levin, C.R. Robbins, H.F. McMurdie, Phase diagrams for Ceramists, Am. Ceram. Soc., Columbus, OH, 1964.

[31] J.D. Cawley, J.W. Halloran, J. Am. Ceram. Soc. 69/8 (1986) C195.

[32] R.C. McCune, W.T. Donlon, R.C. Ku, J. Am. Ceram. Soc. 69/8 (1986) C196.

[33] W. Swiatnicki, S. Lartiguekorinek, J.Y. Laval, Acta Met. Mater. 43/2 (1995) 795.

[34] C.W. Li, W.D. Kingery, in: W.D. Kingery (Ed.), Structure and Properties of MgO and Al_2O_3 Ceramics, American Ceramic Soc., Cambridge, Massachusetts, 1983, p. 368.

[35] M. Danzinger, R. Haubner, B. Lux, in: T.S. Sudarshen, D.G. Bhat (Eds.), Surf. Modif. Technol. III, The Minerals, Metals & Materials Society, Warrendale, 1990, p. 829.

[36] E. Fredriksson, J.O. Carlsson, J. Phys. 50/C-5 (1989) 391.

[37] P. Wilhartitz, M. Grasserbauer, H. Altena, B. Lux, Surf. Interface Anal. 8/4 (1986) 159.

[38] C. Toy, M. Demirci, S. Onurlu, M. Sadik Tasar, T. Baykara, J. Mater. Sci. 30 (1995) 4183.

[39] L. Miller, A. Avishai, W.D. Kaplan, J. Am. Ceram. Soc. 89/1 (2006) 350.

[40] X.H. Tang, K.P.D. Lagerlof, A.H. Heuer, J. Am. Ceram. Soc. 86/4 (2003) 560.

[41] S.I. Bae, S. Baik, J. Am. Ceram. Soc. 76/4 (1993) 1065.

[42] S. Lartigue-Korinek, C. Carry, L. Priester, J. European Ceram. Soc. 22/9-10 (2002) 1525.

[43] W.D. McKee, E. Aleshin, J. Am. Ceram. Soc. 46/1 (1963) 54.

[44] G. Petot-Ervas, B. Saadi, C. Petot, M. Loudjani, J. European Ceram. Soc. 17/7 (1996) 943.

[45] E. Fredriksson, J.O. Carlsson, J. Chem. Vap. Dep. 1 (1993) 333.

[46] C.-S. Park, J.-G. Kim, J.S. Chun, J. Vac. Sci. Technol. 1/4 (1983) 1820.

[47] Q. Fang, P.S. Sidky, M.G. Hocking, Corros. Sci. 39/3 (1997) 511.

[48] L. Curkovic, M.F. Jelaca, S. Kurajica, Corros. Sci. 50/3 (2008) 872.

[49] W. Genthe, H. Hausner, J. European Ceram. Soc. 9/6 (1992) 417.

[50] H. Winkelmann, E. Badisch, M. Roy, H. Danninger, Mater. Corros. 60/1 (2009) 40.

[51] A. Mitsuo, S. Uchida, N. Nihira, M. Iwaki, Surf. Coat. Technol. 103-104 (1998) 98.

[52] J. Wagner, C. Mitterer, M. Penoy, C. Michotte, W. Wallgram, M. Kathrein, in: G. Kneringer, P. Roedhammer, H. Wildner (Eds.), 16th Int. Plansee Seminar, Reutte, 2005, p. 917.

[53] M. Wittmer, J. Noser, H. Melchior, J. Appl. Phys. 52/11 (1981) 6659.

[54] F.R. Charvat, W.D. Kingery, J. Am. Ceram. Soc. 40/9 (1957) 306.

[55] H. Wada, K. Sakane, T. Kitamura, Y. Kayahara, A. Kawahara, N. Sasaki, J. Ceram. Soc. Jap. 102/8 (1994) 695.

[56] D.G. Cahill, S.M. Lee, T.I. Selinder, J. Appl. Phys. 83/11 (1998) 5783.

[57] K.L. Choy, Progr. Mater. Sci. 48/2 (2003) 57.

[58] S.M. Lee, D.G. Cahill, T.H. Allen, Phys. Rev. B 52/1 (1995) 253.

[59] G.A. Slack, D.W. Oliver, Phys. Rev. B 4/2 (1971) 592.

[60] H.E. Hintermann, Wear 100/1-3 (1984) 381.

[61] M. Halvarsson, V. Langer, S. Vuorinen, Surf. Coat. Technol. 76-77 (1995) 358.

[62] H. Holzschuh, in: G. Kneringer, P. Rödhammer, H. Wildner (Eds.), 16th Int. Plansee Seminar, Reutte, 2005, p. 801.

[63] W. Schedler, Hartmetall, VDI-Verl., Düsseldorf, 1988.

[64] A. Krell, O.V. Bakun, Acta Met. 34/7 (1986) 1315.

[65] A. Krell, S. Schädlich, Int. J. Refract. Met. Hard Mater. 19/4-6 (2001) 237.

[66] T. Nagai, K. Wasa, S. Hayakawa, J. Mater. Sci. 11/8 (1976) 1509.

[67] L. Boudoukha, F. Halitim, S. Paletto, G. Fantozzi, Ceram. Int. 24/3 (1998) 189.

[68] M.E. O'Hern, C.J. McHargue, C.W. White, G.C. Farlow, Nucl. Instr. Meth. 46/1-4 (1990) 171.

[69] J.B. Wachtman, D.G. Lam, J. Am. Ceram. Soc. 42/5 (1959) 254.

[70] W. Ensinger, R. Nowak, Nucl. Instr. Meth. 80-81/Part 2 (1993) 1085.

[71] M.O. Guillou, J.L. Henshall, R.M. Hooper, Int. J. Refract. Met. Hard Mater. 16/4-6 (1998) 323.

[72] P.K. Mehrotra, D.T. Quinto, High Temp.-High Press. 18 (1986) 199.

[73] S. Ruppi, A. Larsson, A. Flink, Thin Solid Films 516/18 (2008) 5959.

[74] A. Jämting, M. Ring, S. Ruppi, M.V. Swain, J. Hard Mater. 6/2 (1995) 67.

[75] J. Zhao, V.V. Silberschmidt, Computational Mater. Sci. 32/3-4 (2005) 620.

[76] H. Chien, M.C. Gao, H.M. Miller, G.S. Rohrer, Z. Ban, P. Prichard, Y. Liu, Int. J. Refract. Met. Hard Mater. 27/2 (2009) 458.

[77] X.D. Zhu, H.L. Dou, Z.G. Ban, Y.X. Liu, J.W. He, Key Engin. Mater. 373-374 (2008) 113.

[78] R.H.J. Hannink, M.J. Murray, H.G. Scott, Wear 100/1-3 (1984) 355.

[79] I.M. Hutchings, Tribology: Friction and Wear of Engineering Materials, Edward Arnold, London, 1992.

[80] E. Rabinowicz, Friction and wear of materials, John Wiley, New York, 1995.

[81] K. Holmberg, A. Matthews, Coatings Tribology: Properties, Mechanisms, Techniques and Applications in Surface Engineering, Elsevier, Amsterdam, Oxford, 2009.

[82] G. Boothroyd, Proc. Inst. Mech. Engrs. 177/29 (1963) 789.

[83] A.K. Tieu, X.D. Fang, D. Zhang, Wear 214/2 (1998) 252.

[84] B. Lux, C. Colombier, H. Altena, K. Stjernberg, Thin Solid Films 138/1 (1986) 49.

[85] A. Larsson, M. Halvarsson, S. Ruppi, Surf. Coat. Technol. 111/2-3 (1999) 191.

[86] G. List, M. Nouari, D. Gehin, S. Gomez, J.P. Manaud, Y. Le Petitcorps, F. Girot, Wear 259 (2005) 1177.

[87] T. Ishii, N. Shima, H. Ueda, S. Okayama, M. Gonda, J. Vac. Sci. Technol. A 19/2 (2001) 633.

[88] Z.-J. Liu, Z.-K. Liu, C. McNerny, P. Mehrotra, A. Inspektor, Surf. Coat. Technol. 198/1-3 (2005) 161.

[89] S. Ruppi, M. Halvarsson, Thin Solid Films 353/1-2 (1999) 182.

[90] Y. Someno, M. Sasaki, T. Hirai, Jap. J.Appl. Phys. 30/8 (1991) 1792.

[91] J. Wagner, Chemical Vapor Deposition of Titanium Nitride based HArd Coatings, Ph.D. thesis, Montanuniversität Leoben, 2007.

[92] J.O. Carlsson, Thin Solid Films 130 (1985) 261.

[93] R. Funk, H. Schachner, C. Triquet, M. Kornmann, B. Lux, J. Electrochem. Soc. 123/2 (1976) 285.

[94] E. Fredriksson, J.-O. Carlsson, Surf. Coat. Technol. 73/3 (1995) 160.

[95] S. Vuorinen, J. Skogsmo, Thin Solid Films 193/1-2 (1990) 536.

[96] C. Colombier, J. Peng, H. Altena, B. Lux, Int. J. Refract. Hard Met. 5/2 (1986) 82.

[97] M. Danzinger, J. Peng, R. Haubner, B. Lux, J. Phys. II 1/C2 (1991) 571.

[98] P. Mårtensson, Surf. Coat. Technol. 200/11 (2006) 3626.

[99] T. Oshika, M. Sato, A. Nishiyama, J. Phys. IV 12/PR4 (2002) 113.

[100] W.C. Russell, C. Strandberg, Int. J. Refract. Met. Hard Mater. 14/1-3 (1996) 51.

[101] J.A. Aboaf, D.R. Kerr, E. Bassous, J. Electrochem. Soc. 120/8 (1973) 1103.

[102] R. Colmet, R. Naslain, Wear 80/2 (1982) 221.

[103] C. Colombier, B. Lux, J. Lindström, Int. J. Refract. Hard Met. (1986) 222.

[104] R. Connelly, A.K. Pattanaik, V.K. Sarin, Int. J. Refract. Met. Hard Mater. 23/4-6 (2005) 317.

[105] M. Astrand, T.I. Selinder, F. Fietzke, H. Klostermann, Surf. Coat. Technol. 188-89 (2004) 186.

[106] K. Bobzin, E. Lugscheider, M. Maes, C. Piñero, Thin Solid Films 494/1-2 (2006) 255.

[107] R. Cremer, K. Reichert, D. Neuschütz, G. Erkens, T. Leyendecker, Surf. Coat. Technol. 163-164 (2003) 157.

[108] R. Cremer, M. Witthaut, D. Neuschütz, G. Erkens, T. Leyendecker, M. Feldhege, Surf. Coat. Technol. 120-121 (1999) 213.

[109] M.S. Jochen, D.S. William, M. Allan, Surf. Coat. Technol. 94-95 (1997) 179.

[110] T. Leyendecker, I. Rass, G. Erkens, M. Feldhege, Surf. Coat. Technol. 97/1-3 (1997) 790.

[111] B. Rother, Surf. Coat. Technol. 154/2-3 (2002) 262.

[112] Y. Yamada-Takamura, F. Koch, H. Maier, H. Bolt, Surf. Coat. Technol. 142-144 (2001) 260.

[113] O. Zywitzki, K. Goedicke, H. Morgner, Surf. Coat. Technol. 151-152 (2002) 14.

[114] O. Zywitzki, G. Hoetzsch, Surf. Coat. Technol. 94-95 (1997) 303.

[115] D.T. Quinto, Int. J. Refract. Met. Hard Mater. 14/1-3 (1996) 7.

[116] O. Zywitzki, G. Hoetzsch, Surf. Coat. Technol. 76-77/Part 2 (1995) 754.

[117] D.T. Quinto, G.J. Wolfe, P.C. Jindal, Thin Solid Films 153/1-3 (1987) 19.

[118] T.I. Selinder, E. Coronel, E. Wallin, U. Helmersson, Int. J. Refract. Met. Hard Mater. 27/2 (2009) 507.

[119] E. Marin, L. Guzman, A. Lanzutti, L. Fedrizzi, M. Saikkonen, Electrochem. Com. 11/10 (2009) 2060.

[120] A. Schütze, D.T. Quinto, Surf. Coat. Technol. 162/2-3 (2003) 174.

[121] J. Alami, P.O.Ã. Persson, D. Music, J.T. Gudmundsson, J. Bohlmark, U. Helmersson, J. Vac. Sci. Technol. 23/2 (2005) 278.

[122] C. Täschner, B. Ljungberg, V. Alfredsson, I. Endler, A. Leonhardt, Surf. Coat. Technol. 108-109/1-3 (1998) 257.

[123] V. Edlmayr, M. Moser, C. Walter, C. Mitterer, Surf. Coat Technol. 204/9-10 (2010) 1576.

[124] F. Klocke, K. Gerschwiler, S.E. Cordes, R. Fritsch, Adv. Engin. Mater. 10/7 (2008) 622.

[125] M. Fink, J. Laimer, H. Störi, C. Mitterer, Surf. Coat. Technol. 200/1-4 (2005) 360.

[126] O. Kyrylov, R. Cremer, D. Neuschütz, Surf. Coat. Technol. 163-164 (2003) 203.

[127] R. Tabersky, H. van den Berg, U. König, Int. J. Refract. Met. Hard Mater. 14/1-3 (1996) 79.

[128] C. Täschner, B. Ljungberg, I. Endler, A. Leonhardt, Surf. Coat. Technol. 116-119 (1999) 891.

[129] P. Frach, H. Bartzsch, D. Glöß, M. Fahland, F. Händel, Surf. Coat. Technol. 202/22-23 (2008) 5680.

[130] private communication, F. Rovere, 2009.

[131] J.M. Blocher, J. Vac. Sci. Technol. 11/4 (1974) 680.

[132] D.M. Dobkin, M.K. Zuraw, Principles of chemical vapor deposition, Kluwer Academic Publishers, Dordrecht, Bosten, London, 2003.

[133] J.-G. Kim, C.-S. Park, J.S. Chun, Thin Solid Films 97/1 (1982) 97.

[134] C.-S. Park, J.-G. Kim, J.S. Chun, J. Electrochem. Soc. 130/7 (1983) 1607.

[135] L. Catoire, M.T. Swihart, J. Electrochem. Soc. 149/5 (2002) C261.

[136] S.V. Sotirchos, S.F. Nitodas, J. Cryst. Growth 234 (2002) 569.

[137] I. Nasution, A. Velasco, H.-j. Kim, J. Cryst. Growth 311/2 (2009) 429.

[138] G.L. Tingey, J. Phys. Chem. 70/5 (1966) 1406.

[139] S.F. Nitodas, S.V. Sotirchos, J. Electrochem. Soc. 149/2 (2002) C130.

[140] A. Kwatera, Thin Solid Films 200/1 (1991) 19.

[141] M. Schierling, E. Zimmermann, D. Neuschutz, J. Phys. IV 9/P8 (1999) 85.

[142] C. Czettl, Oxide-based Coatings Deposited by Thermal CVD, Diploma thesis, Montanuniversität Leoben, 2007.

[143] M. Schlögl, Influence of Dopants on Oxide-based Coatings Deposited by Thermal CVD, Diploma thesis, Montanuniversität Leoben, 2009.

[144] I. Lhermitte-Sebire, R. Colmet, R. Naslain, C. Bernard, J. Less Common Met. 118/1 (1986) 83.

[145] P.F. Tan, J. Muller, D. Neuschutz, J. Electrochem. Soc. 152/5 (2005) C288.

[146] E. Fredriksson, J.O. Carlsson, Thin Solid Films 263/1 (1995) 28.

[147] M. Halvarsson, J.E. Trancik, S. Ruppi, I. J. Refract. Met. Hard Mater. 24/1-2 (2006) 32.

[148] S. Ruppi, Surf. Coat. Technol. 202/17 (2008) 4257.

[149] C. Chatfield, J.N. Lindstrom, M.E. Sjostrand, J. Phys. 50/5 (1989) 377.

[150] M. Halvarsson, S. Vuorinen, Surf. Coat. Technol. 76-77/1 (1995) 287.

[151] C. Chatfield, Int. J. Refract. Met. Hard Mater. (1990) 132.

[152] M. Halvarsson, S. Vuorinen, Mater. Sci. Engin. A 209/1-2 (1996) 337.

[153] M. Halvarsson, H. Nordén, S. Vuorinen, Surf. Coat. Technol. 68-69 (1994) 266.

[154] S. Ruppi, A. Larsson, J. Vac. Sci. Technol. A 21/1 (2003) 66.

[155] C. Czettl, C. Mitterer, M. Penoy, C. Michotte, M. Kathrein, in: L. Sigl, P. Rödhammer, H. Wildner (Eds.), 17th Int. Plansee Seminar, Reutte, 2009, p. 565.

[156] G.B. Harris, Phil. Mag. 43/336 (1952) 113.

[157] K. Matsunaga, A. Nakamura, T. Yamamoto, Y. Ikuhara, Phys. Rev. B 68/21 (2003).

[158] L. Curkovic, M.F. Jelaca, Ceram. Int. 35/5 (2009) 2041.

[159] B.J. Pletka, T.E. Mitchell, A.H. Heuer, Acta Met. 30/1 (1982) 147.

[160] S. Lartigue-Korinek, C. Legros, C. Carry, F. Herbst, J. European Ceram. Soc. 26/12 (2006) 2219.

[161] D.-H. Kuo, C.-N. Shueh, Thin Solid Films 478/1-2 (2005) 109.

[162] A. Stabel, A. Caballero, J.P. Espinos, F. Yubero, A. Justo, A.R. Gonzalez-Elipe, Surf. Coat. Technol. 100-101 (1998) 142.

[163] K.A. Habib, J.J. Saura, C. Ferrer, M.S. Damra, E. Gimenez, L. Cabedo, Surf. Coat. Technol. 201/3-4 (2006) 1436.

[164] X. Lin, Y. Zeng, C. Ding, P. Zhang, Wear 256/11-12 (2004) 1018.

[165] C. Colombier, B. Lux, J. Mater. Sci. 24/2 (1989) 462.

[166] F. Halitim, N. Ikhlef, S. Abdeslam, G. Fantozzi, Ceram. Int. 23/6 (1997) 509.

[167] K. Matsunaga, A. Nakamura, T. Yamamoto, Y. Ikuhara, Solid State Ionics 172/1-4 (2004) 155.

[168] A. Yasuda, J. Aoki, T. Sakuma, Ceram. Int. 24/7 (1998) 483.

[169] R.B. Jackman, B. Baral, C.R. Kingsley, J.S. Foord, Diamond Relat. Mater. 5 (1996) 378.

[170] Y. Kunii, Y. Inokuchi, A. Moriya, H. Kurokawa, J. Murota, Appl. Surf. Sci. 224 (2004) 68.

[171] W.G. French, L.J. Pace, V.A. Foertmeyer, J. Phys. Chem. 82/20 (1978) 2191.

[172] V. Geiss, E. Froschle, J. Electrochem. Soc. 123/1 (1976) 133.

[173] N.A. Sezgi, A. Ersoy, T. Dogu, H.Ö. Özbelge, Chem. Engin.Process. 40 (2001) 525.

[174] P. Peshev, J. Solid State Chem. 154/1 (2000) 157.

[175] C. Cheng, C. Tang, X.X. Ding, X.T. Huang, Z.X. Huang, S.R. Qi, L. Hu, Y.X. Li, Chem. Phys. Lett. 373/5-6 (2003) 626.

[176] Y. Li, R.P.H. Chang, Mater. Chem. Phys. 97/1 (2006) 23.

[177] W.D. Fei, L.D. Wang, Mater. Chem. Phys. 85/2-3 (2004) 450.

[178] K. Suganuma, T. Fujita, N. Suzuki, K. Niihara, J. Mater. Sci. 9 (1990) 633.

[179] Y. Saih, K. Segawa, Appl. Catal. 353/2 (2009) 258.

[180] A.B. Belonoshko, R. Ahuja, B. Johansson, Phys. Rev. B 61/5 (2000) 3131.

[181] P. Hansson, M. Halvarsson, S. Vuorinen, Surf. Coat. Technol. 76-77 (1995) 256.

[182] J. Skogsmo, M. Halvarsson, S. Vourinen, Surf. Coat. Technol. 54/1-3 (1992) 186.

[183] S. Vuorinen, L. Karlsson, Thin Solid Films 214/2 (1992) 132.

[184] H. Altena, G. Pauer, P. Wilhartitz, B. Lux, in: J.O. Carlsson, J. Lindström (Eds.), 5th EuroCVD, Uppsala, Sweden, 1985, p. 334.

7. Publications

7.1. List of included publications

Publication I:	Titanium doped CVD alumina coatings *D. Hochauer, C. Mitterer, M. Penoy, C. Michotte, H.P. Martinz, M. Kathrein* Surface and Coatings Technology 203 (2008) 350-356.
Publication II:	The effect of boron doping on thermal CVD of alumina *D. Hochauer, C. Mitterer, M. Penoy, C. Michotte, H.P. Martinz, M. Kathrein* Proceedings of the 17th Int. Plansee Seminar 2009, Vol. 2, p. 555-564.
Publication III:	Carbon doped alumina coatings grown by thermal CVD *D. Hochauer, C. Mitterer, M. Penoy, C. Michotte, S. Puchner, H. Hutter, H.P. Martinz, M. Kathrein* in manuscript
Publication IV:	Thermal stability of doped CVD κ-Al_2O_3 coatings *D. Hochauer, C. Mitterer, M. Penoy, C. Michotte, H.P. Martinz, M. Kathrein* Surface and Coating Technology (2010), in submission

7.2. Supervised diploma theses

Diploma thesis I:	Oxide-based coatings deposited by thermal CVD *C. Czettl*, May 2007
Diploma thesis II:	Influence of dopants on oxide-based coatings deposited by thermal CVD *M. Schlögl*, June 2009

7.3. Contributions to the included publications

	Concept*	Experimental	Interpretation	Manuscript*
Publication I	70%	40%	80%	85%
Publication II	70%	50%	90%	90%
Publication III	80%	40%	90%	90%
Publication IV	80%	70%	90%	90%

* supervision is not included

Publication I

Surface and Coatings Technology 203 (2008) 350-356.

Titanium doped CVD alumina coatings

D. Hochauer[a], C. Mitterer[b], M. Penoy[c], C. Michotte[c], H.P. Martinz[d], M. Kathrein[e]

a) Materials Center Leoben Forschung GmbH, Roseggerstrasse 12, A-8700 Leoben, Austria
b) Department of Physical Metallurgy and Materials Testing, University of Leoben, Franz-Josef-Strasse 18, A-8700 Leoben, Austria
c) CERATIZIT Luxembourg SARL, L-8201 Mamer, Luxembourg
d) PLANSEE SE, A-6600 Reutte, Austria
e) CERATIZIT Austria GmbH, A-6600 Reutte, Austria

Abstract

Chemical vapor deposited alumina coatings are successfully applied for high-performance cemented carbide cutting tools. The aim of this work was to investigate in detail the influence of a varied $TiCl_4$ flow rate on the deposition of alumina by low-pressure chemical vapor deposition (LPCVD). The coatings were deposited onto a TiN-TiCN base-layer at 1005°C using a precursor gas mixture of $AlCl_3$, $TiCl_4$, CO_2, HCl, H_2S, and H_2. Coating characterization was conducted by scanning electron microscopy (SEM), glancing angle X-ray diffraction (GAXRD), glow discharge optical emission spectroscopy (GDOES), nanoindentation, biaxial stress measurements, and ball-on-disc tests. GAXRD investigations showed the α-Al_2O_3 phase for all coatings beside different titanium compounds. SEM top-view images indicated that low titanium contents modify the polygonal grain shape of the α-Al_2O_3 phase to a more cuboid-like form, while the highest titanium content applied (4.2 at.% Ti) causes a less dense coating topography. The hardness values remain constant at ~26 GPa for pure α-Al_2O_3 and low Ti doping contents and decrease slightly to ~23 GPa for 4.2 at.% Ti. However, with increasing Ti-content the tribological behavior at 700°C in terms of both friction and wear resistance is significantly improved.

1. Introduction

Doping and alloying of alumina with titanium is used for many applications in order to design crucial properties like hardness, wear resistance or optical parameters [1-4], whereas only very little work is published concerning doped alumina coatings applied for wear protection of cutting tools [5]. Undoped alumina coatings are widely used for cutting applications due to their high chemical stability, low thermal conductivity and high hardness also at high temperatures [6-8] and their microstructure is well investigated [9-12]. Common coating architectures consist of TiN, TiC, and/or TiCN base-layers which are deposited prior to a mono- or multilayer of alumina [9, 10, 13]. Frequently, a thin TiN top-layer improves wear indication and optical appearance. Thermal chemical vapor deposition is the dominating process for the production of these coating systems, but recently also physical vapor deposited alumina coatings have been reported [14-17].

This work focuses on the influence of a varied $TiCl_4$ flow rate on the deposition of alumina with chemical vapor deposition at low pressures (LPCVD). The precursor gas mixture applied is based on a composition similar to that utilized for commercially deposited alumina multilayers, where the $TiCl_4$ flow rate was systematically varied. Instead of a multilayer arrangement an alumina monolayer was deposited in order to minimize additional influences superimposing the $TiCl_4$ flow rate. Special emphasis was laid on structure evolution with increasing Ti-content and the resulting effects on mechanical properties and tribological behavior.

2. Experimental details

Undoped and Ti-doped alumina monolayer coatings were deposited by LPCVD at a pressure of 80 mbar. The temperature during alumina deposition was set to 1005°C, utilizing an industrial-scale hot-wall CVD plant with radial gas distribution (Bernex BPX 530L). The precursor mixture comprised of the gases $AlCl_3$, CO_2, HCl, H_2S, H_2, and $TiCl_4$ which was the only liquid precursor. The latter was varied between 0.0 and 0.6 ml/min (0 - 0.23 vol.%), while the composition of the other gases was kept constant and is comparable to state-of-the-art coatings as reported in literature [13, 18-20]. The alumina deposition time was 3 hours. To improve adhesion and suppress coating/substrate interdiffusion, a TiN/TiCN base-layer was applied between the cemented carbide substrates (11 wt.% Co, 4 wt.% TiC, 8 wt.% TaC-NbC, 77 wt.% WC) and alumina. For tribological tests, disc-shaped substrates with a diameter of 30 mm and a thickness of 4 mm were used; all other investigations were performed on flat cemented carbide inserts (12.8 × 12.8 × 4.8 mm^3). Prior to deposition, all substrates were polished and cleaned with a standard procedure comparable to commercial production.

Concentration depth profiles were determined by glow discharge optical emission spectroscopy (GDOES) with a Jobin-Yvon Horiba JY10000RF equipment. The given chemical compositions were calculated by averaging these concentration values within the respective alumina layers. To confirm the so obtained coating composition and for additional information about the chemical bonding states, X-ray photoelectron spectroscopy (XPS) was performed, using an Omicron Multiprobe system (Al $K\alpha$ radiation). Spectra were obtained for the as-deposited state, after in-situ vacuum annealing at 350°C for 20 min and after Ar^+ ion sputtering at 2 keV for 20 min, respectively. The energy scale of the XPS spectra was corrected using the deviation of the adventitious carbon peak at 285.0 eV (C 1s). The crystallographic structure and phase formation were determined with glancing angle X-ray diffraction (GAXRD) using Cu $K\alpha$ radiation with an incident angle of 2°. The residual stresses in the alumina layer were analyzed with the $\sin^2\psi$-method. All XRD measurements were conducted with a Panalytical X'Pert Pro diffractometer. Coating top-view morphology and fracture cross-section appearance were investigated with a scanning electron microscope (SEM, Zeiss EVO 50) equipped with an energy-dispersive X-ray analyzer (Oxford Instruments INCA).

Hardness and Young's modulus were assessed by nanoindentation on diamond-polished coating surfaces, using a UMIS system with a Berkovich indenter, and loads stepwise increased from 1 to 50 mN for each measurement. The tribological characterization was performed on CSM ball-on-disc tribometers at room temperature and 700°C with a 6 mm diameter alumina ball counterpart. Normal-load sliding-distance combinations of 10 N for 500 m and 5 N for 100 m were used for room temperature and high temperature tests, respectively. For all tests, a tangential sliding speed of 0.1 m/s and a wear track radius of 5 mm were selected. The width of the wear tracks was measured with a Wyko NT1000 3D profiling system (white light interferometry) and compared with light optical microscope (LOM) images of the ball-wear scar. Subsequently, all discs from room- and high temperature ball-on-disc tests were investigated with Raman spectroscopy, using a Jobin-Yvon LabRam confocal Raman spectrometer (Nd-YAG laser, wavelength: 532.2 nm, power: 10 mW). Several measurements were performed within and outside the wear track after a calibration procedure on silicon, polyethylene and calcite.

3. Results and discussion

Alumina coatings show an increasing Ti-content with increased $TiCl_4$ addition to the precursor gas mixture. Fig. 1 displays the deposition rate, derived from the coating thickness as observable in the SEM fracture cross-sections and the corresponding deposition time, and the Ti-content as determined with GDOES plotted versus the $TiCl_4$ flow rate. For flow rates up to 0.4 ml/min $TiCl_4$, an apparently linear dependency is visible, while for 0.6 ml/min $TiCl_4$ a disproportionally high Ti-content emerges. The deposition rate drops from ~1.4 µm/h for $TiCl_4$ flow rates below 0.4 ml/min to ~0.9 µm/h for 0.6 ml/min $TiCl_4$. This decline is accompanied by the onset of powder formation within the deposition chamber; hence a further increased $TiCl_4$ flow rate would be unfavorable for synthesis of dense coatings. It seems that the deviations from the average Ti-content within the alumina coating are getting more pronounced with increasing $TiCl_4$ flow rate. The error bars in Fig. 1 refer to these Ti-content variations, visible in the GDOES depth profiles, suggesting a less homogeneous Ti distribution with increasing $TiCl_4$ flow rate.

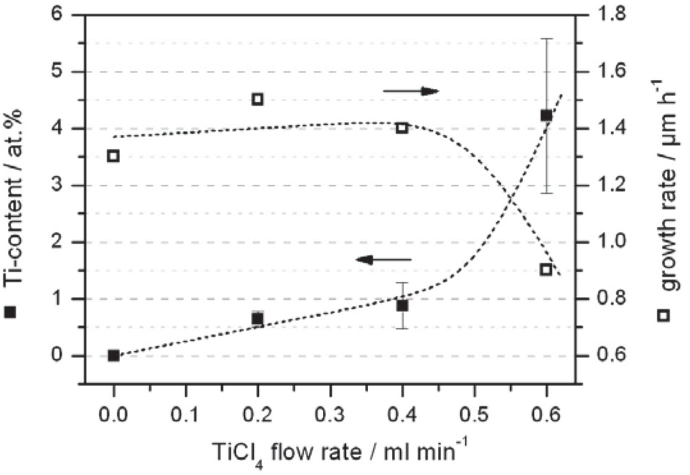

Fig. 1. Influence of increasing $TiCl_4$ addition on alumina deposition rate (open squares) and average Ti-content (solid squares) within the alumina layer.

Fig. 2 shows the development of coating morphology with increasing Ti-content. The shape of the grains is significantly changed already for low Ti-contents, as visible in the top-view images. Typical large equiaxed α-alumina grains [13, 21, 22] are modified to a more cuboid-like shape: moreover the grains of the 0.6 at.% Ti-containing coating seem to show a laminated sub-structure, a feature which is not visible for a further increased Ti-content. The surface facets of the individual grains are less smooth only for the coating with a Ti-content of 0.9 at.%, whereas the grains are elongated and the coating structure seems to be more open for

4.2 at.% Ti. In contrast to the appearance of the top-views, the fracture surfaces of the different coatings are very similar to each other, except for a slightly smaller surface roughness for the undoped alumina coating (see Fig. 2). The fracture cross-section images show the coating architecture, consisting of an alumina top-layer and a TiN/TiCN base-layer, deposited onto the cemented carbide substrate (below the dash-dotted line in Fig. 2). The alumina/TiCN interface is indicated by a dashed line, evidencing that the coating with the highest Ti-content is the thinnest one. As has been shown in Fig. 1, based on a constant alumina deposition time, the deposition rate is the lowest for this coating. Generally, a thinner coating tends to consist of smaller grains [23] which could explain the finer structures shown in Fig. 2 for the 4.2 at.% Ti-containing coating. It is noticeable that the fracture surface of this coating is compact, despite the somewhat open appearance in the top-view.

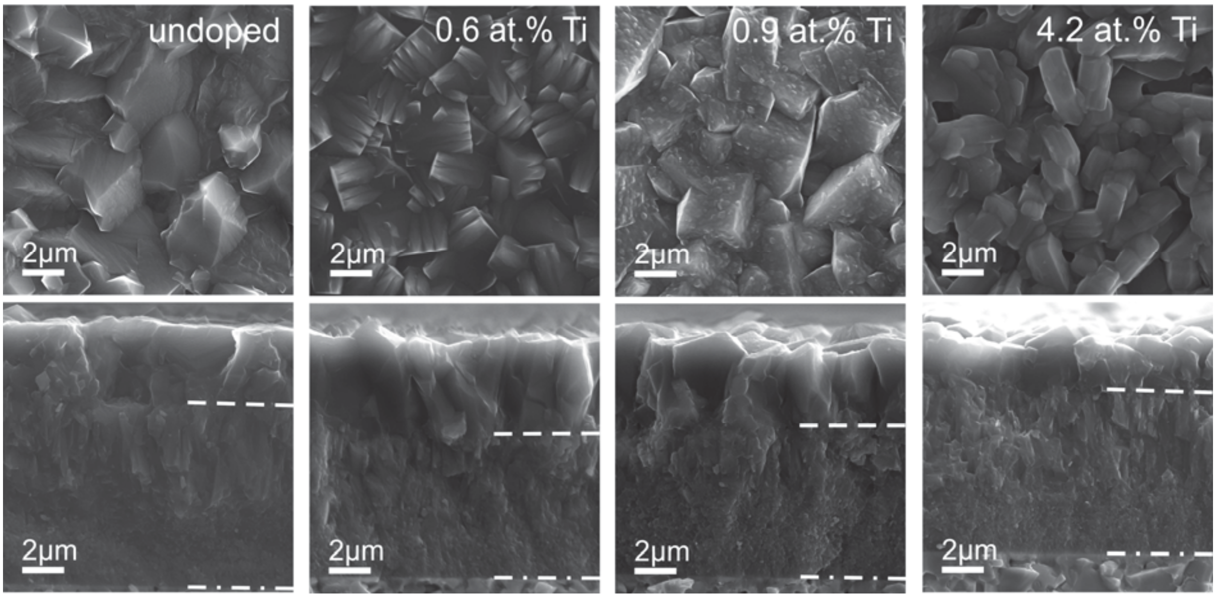

Fig. 2. SEM images of the coating top-view morphology (upper row) and the fracture cross-sections (lower row) with increasing Ti-content. The alumina/TiCN interface and the TiCN/cemented-carbide interface are indicated by white dashed and dash-doted lines, respectively.

XPS investigations of as-deposited and in-situ vacuum annealed coating surfaces showed pronounced contents of the elements O, Al, and C as well as low amounts of N and Ti. In order to exclude surface contamination the relevant peaks were identified after Ar^+ sputtering, while this process implanted ~2-3 at.% Ar. Nevertheless, for detailed analysis the data obtained on vacuum annealed coatings were considered, because of the possible correction of charge-related shifts of the spectra using the C 1s peak, which was not possible after sputtering. Furthermore, the Ti-spectrum was distorted after the sputtering process, i.e.

splitting in at least two broad doublets for the highest Ti-content was observed. This sputtering effect is well known for titanium oxides [24, 25]. Fig. 3 shows the Al 2p, Ti 2p and O 1s spectra for increasing Ti-content after in-situ vacuum annealing. The Al 2p doublet, at the binding energy of Al_2O_3 (Al $2p_{3/2}$ = 73.9 eV) [26], is almost unaffected by the increased $TiCl_4$ flow rate. The Ti 2p doublet is positioned at the binding energy of TiO_2 (Ti $2p_{3/2}$ = 458.5 eV, Ti $2p_{1/2}$ ~ 464 eV) [26, 27] and shows a clearly increasing intensity with increasing $TiCl_4$ flow rate. The quantification of the XPS measurements (surface contamination included) resulted in Ti-contents of 0.4 at.%, 0.7 at.% and 3.9 at.%, hence, confirming the GDOES measurements of the Ti-contents. For the coating with the highest Ti-content, a second Ti 2p doublet appears ~2.1 eV below the major peak. This indicates a second type of environment for a smaller fraction of the Ti atoms, detectable only for the coatings with the highest Ti-content. The lower binding energy suggests a less electronegative surrounding, as for example observed in Ti sub-oxides [24, 25, 28] while a ternary phase like Al_2TiO_5 should have a higher binding energy (Ti $2p_{3/2}$=459.1 eV) [27]. The oxygen peak consists of at least two components which are positioned close to the binding energy of Al_2O_3 and adsorbed water at 531.6 eV [26] and 532.9 eV [29, 30], respectively. After vacuum annealing, the water sub-peak is only visible as asymmetrical shape of the O 1s peak, due to its comparably low intensity. It is much more pronounced in the as-deposited state but disappears completely after Ar^+ sputtering. A clear shoulder appears for the coating with the highest Ti-content at 530.1 eV, which could be attributed to the oxygen-titanium binding energy [27, 30-32]. The quantification of this sub-peak (6.7 at.% O bonded to Ti) shows a reasonable match with the detected Ti-content with regard to the formation of Ti-oxide. For the coatings with lower Ti-content, it was not possible to distinguish whether this peak is not existent or superimposed by the main O1s peak.

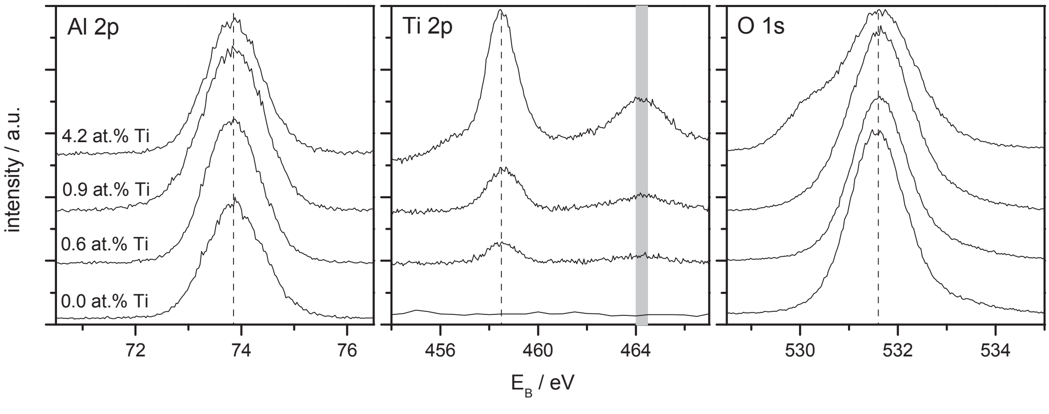

Fig. 3. XPS spectra of Al, Ti and O with increasing Ti-content. The position of the Ti $2p_{3/2}$ and the Ti $2p_{1/2}$ peak is indicated with a dashed line and a grey bar, respectively.

Complementary to the investigation of the chemical binding states, the crystalline coating components were examined with GAXRD (Fig. 4). All diffraction patterns show the α-Al_2O_3 structure with only slight differences concerning the preferred orientation which was estimated using the Harris formula [33], considering the eight strongest peaks of the JCPDS standard (PDF 00-010-0173). In general, the (110) and (214) reflections at 2θ angles of 37.8° and 66.5° are more pronounced while (104) and (116) peaks at 35.1° and 57.5°, respectively, are comparably smaller. This type of preferred orientation is not changed, but more pronounced for the Ti-containing coatings. Except for this increase in preferred orientation, the patterns of the undoped and 0.6 at.% Ti-containing coating are very similar; hence only the former one is displayed in Fig. 4. Beside the α-Al_2O_3 peaks, all coatings show TiCN peaks (PDF 00-042-1488) of the base-layer. For higher Ti-contents, additional phases are observed within the XRD patterns, which are Ti-sulfide and Ti-oxide for 0.9 and 4.2 at.% Ti, respectively. The Ti-sulfide phase can be clearly attributed to Ti_2S_3 (PDF 04-006-5312) while the Ti-oxide peaks comprise two different types of Ti_3O_5 (PDF 00-023-0606, PDF 00-040-0806). Beside the Ti-oxide, possibly small amounts of Al_2TiO_5 (PDF 01-070-1434) emerge, indicated by two tiny shoulders which coincide with the two most intensive peaks of this ternary phase at 2θ angles of 26.5° and 33.7°.

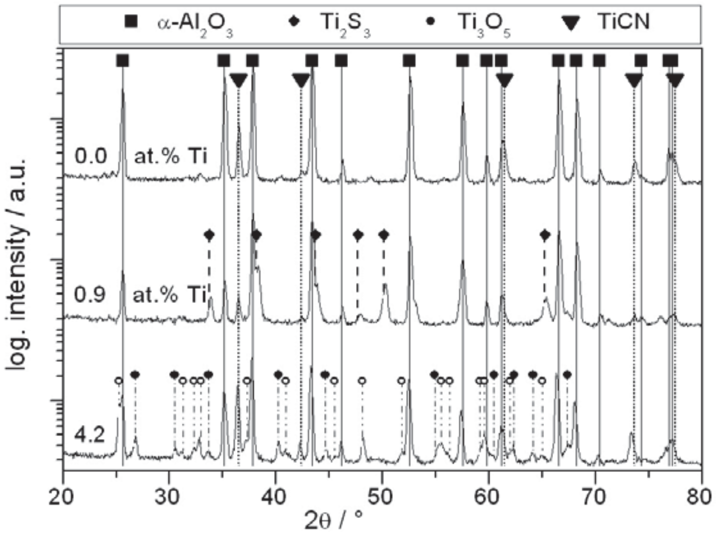

Fig. 4. GAXRD patterns with increasing Ti-content. The Ti_3O_5 peaks are attributed to two different JCPDS files, indicated by solid (PDF 00-040-0806) and open circles (PDF 00-023-0606).

Fig. 5 displays the lattice parameters a and c of the rhombohedral alumina unit cell, which are close to the standard value of α-Al_2O_3 (PDF 00-010-0173) and essentially constant for Ti-contents below 1 at.%. It is assumed that due to the low Ti solubility limit of alumina [34] virtually no Ti is incorporated in the α-Al_2O_3 phase for these lower $TiCl_4$ flow rates. It should be mentioned that an eventually formed Ti-oxide phase for these low Ti-contents might be below the detection limit of GAXRD. Nevertheless, for the highest Ti-content, the deposition conditions are quite different (lower coating growth rate, powder formation) and it seems that some Ti is forced to be incorporated in the alumina beside the major amount of Ti which segregates as an oxide. Thus, the lattice parameters show a slight increase of 0.02 Å and 0.04 Å along the a and c axis, respectively.

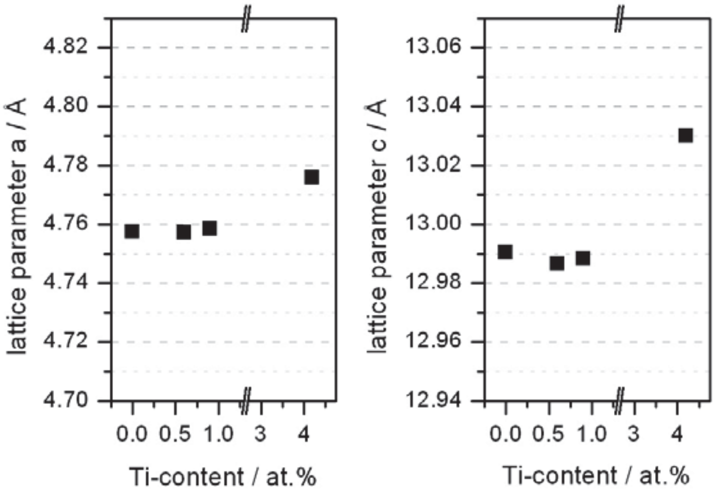

Fig. 5. Lattice parameters a (left) and c (right) of the rhombohedral alumina unit cell as a function of Ti-content. Alumina standard values (PDF 00-010-0173) are a = 4.758 Å and c = 12.991 Å.

The residual stresses of the coatings as determined by the $\sin^2\psi$-method are tensile and decrease from a maximum around 570 MPa for undoped alumina to a value below 400 MPa for low Ti-contents (see Fig. 6). A stress minimum was obtained for the 0.9 at.% Ti-containing coating (~250 MPa), while higher Ti-contents result in again increasing tensile stress. The decline in residual stress is accompanied by a denser crack network, as visible on the LOM images of polished coating surfaces shown in Fig. 6. Obviously, already low Ti-contents decrease the resistance of the coating against tensile crack formation, as evidenced by the increasing crack density visible in Fig. 6. It can be assumed that in the vicinity of a crack the local residual stresses are significantly reduced [35, 36]; for example in [37] a distance of a few 10 µm of reduced stress level is mentioned. Thus, for a denser crack network a reduction of the average stresses as determined by the $\sin^2\psi$-method seems to be justified. On the other hand, the changed structural environment caused by the increasing Ti-content could affect the thermal mismatch of different alumina grains, caused by the anisotropic coefficient of thermal expansion (CTE) of the alumina lattice. Consequently, the microstresses, usually originating from the anisotropic CTE of the crystallites [38], would be changed, which could also influence the results of the $\sin^2\psi$-measurement.

The again increasing residual stresses for the highest Ti-containing coating could be in part attributed to the higher CTE of the additionally formed Ti-oxide phase (cf. Fig. 4). The CTE for the Ti_3O_5 sub-oxide might be estimated by the value reported for TiO_2 ($\sim 9\cdot 10^{-6}$ K^{-1}) and compared to the CTE for alumina which is $\sim 8.4\cdot 10^{-6}$ K^{-1} [39]. Further, the lower thickness and the finer grain structure of the 4.2 at.% Ti-containing coating favor a higher coating toughness and thus enables the coating to bear more strain and higher residual stresses, respectively.

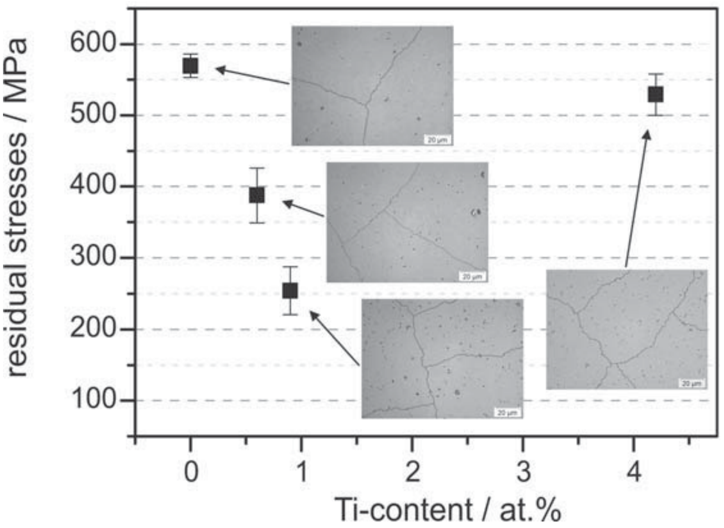

Fig. 6. Residual tensile stresses in the alumina phase with increasing Ti-content. The inserted LOM images (~140 µm × ~100 µm) show cracks as visible after polishing.

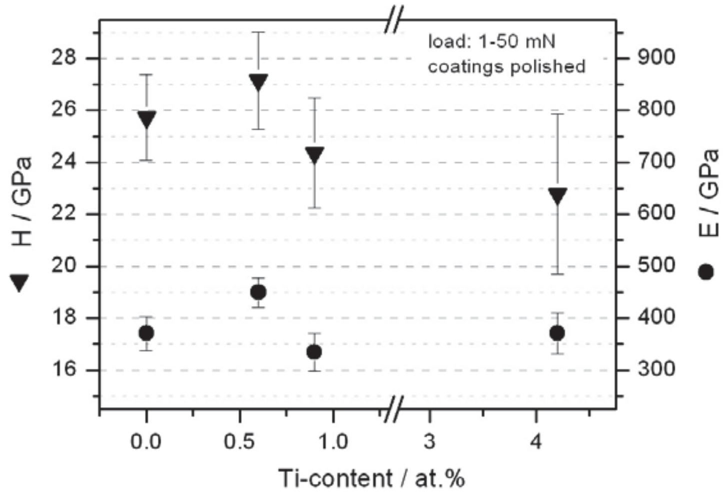

Fig. 7. Coating hardness and Young’s modulus measured by nanoindentation as a function of Ti-content.

Although the residual stresses are different for undoped and low Ti-containing coatings, the nanoindentation measurements yield a rather constant hardness in a range of 26-27 GPa (see Fig. 7). The 0.9 at.% Ti-containing coating shows a slightly lower hardness, which could be related to the small amounts of soft titanium sulfide phase [40] detected by GAXRD (cf. Fig. 4). The lowest hardness value is measured for the coating with the highest Ti-content, which is attributed to a comparably higher amount of the additional Ti_3O_5 phase. The assumption of a lower hardness for Ti_3O_5 compared to Al_2O_3 is supported by the reported hardness for TiO_2 (~11 GPa) [39]. The determination of the Young's modulus reveals values between 330 and 450 GPa for all coatings, which shows no clear dependency on the variation of the Ti-content.

The tribological behavior was investigated at room temperature and 700°C. The average steady-state friction coefficient (μ_{ss}) obtained by room temperature ball-on-disc tests ranges between 0.7 and 0.8 (Fig. 8). After a running-in period, the friction coefficient remains more or less constant and shows low scattering. Only the 4.2 at.% Ti-containing coating comprises sharp changes in the friction curve, although the local scattering is still low. This varying behavior could be associated with the generation of large wear debris which can eventually rotate, thus explaining the sometimes slightly reduced friction coefficient. Once these particles get crushed under the load, the friction coefficient increases again.

By contrast, μ_{ss} as well as its scattering strongly depend on the Ti-content at 700°C testing temperature (Fig. 8). Undoped and low Ti-containing alumina coatings show a considerable higher scattering which is caused by a larger quantity of wear debris, mainly consisting of ball material, as indicated by the observed broad and flat coating wear track. At the same time, μ_{ss} for undoped and 0.6 at.% Ti-containing alumina is ~0.70 and ~0.85, respectively. Higher Ti-contents result in lower scattering and μ_{ss} values, which are significantly reduced to ~0.49 (0.9 at.% Ti) and ~0.42 (4.2 at.% Ti). The wear track width and the amount of worn ball material are much smaller for these two samples compared to the undoped and low Ti-containing coatings (see Fig. 9). Hence, wear seems to correlate with friction within this study, i.e. a low friction coefficient is connected with a small wear track width. It should be noted here that the wear was evaluated by the wear track width because the depth was essentially around zero. Furthermore, longer sliding distances tend to result in local coating failure, rather than in a deeper wear track. In this case, the broken-out regions exhibit a typical dimension of ~100 × 100 μm^2 and a depth comparable to the alumina coating thickness. At room temperature a constant wear track width of ~0.4 mm is measured for all coatings, while at 700°C this value drops from ~1.5 mm for undoped and low Ti-containing coatings to a value of less than 0.3 mm for medium and high Ti-containing coatings.

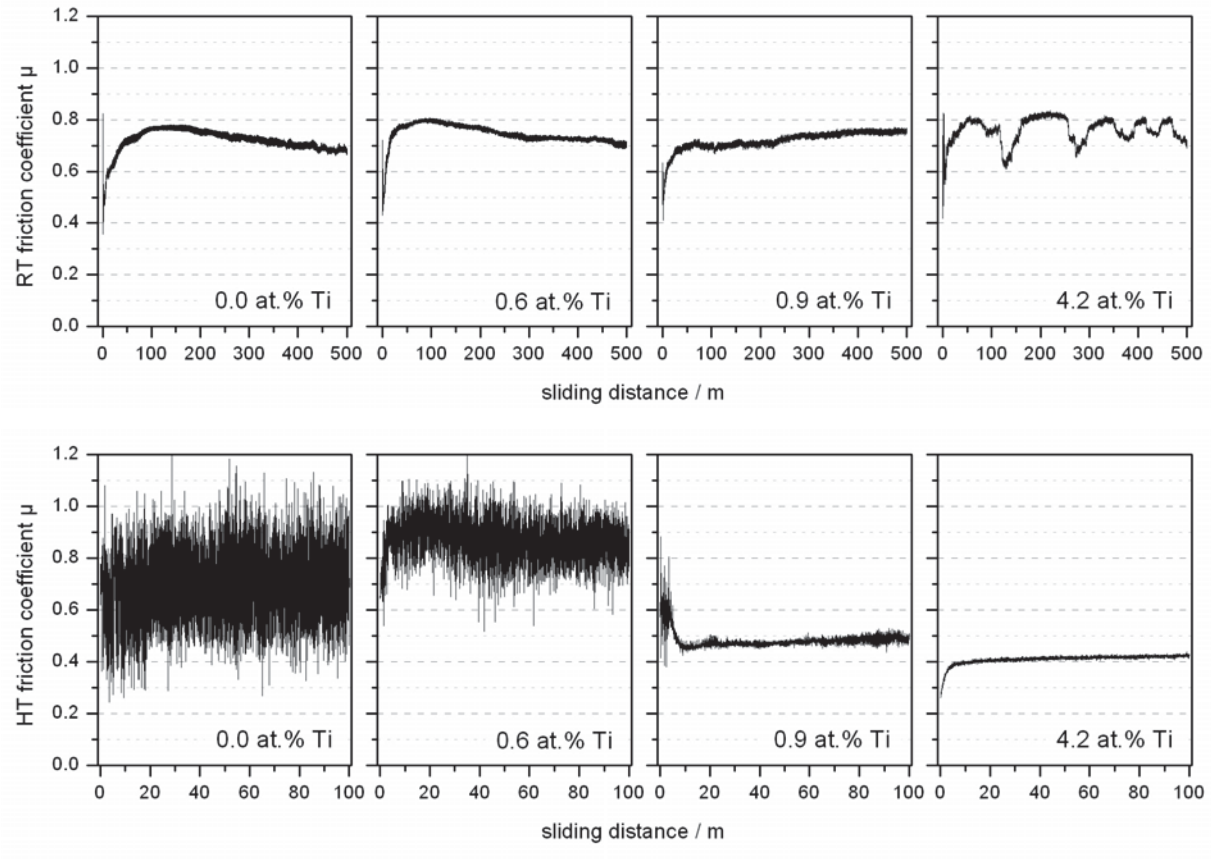

Fig. 8. Friction coefficient determined with ball-on-disc tests at room temperature (upper row) and at 700°C (lower row) with increasing Ti-content within the alumina coating.

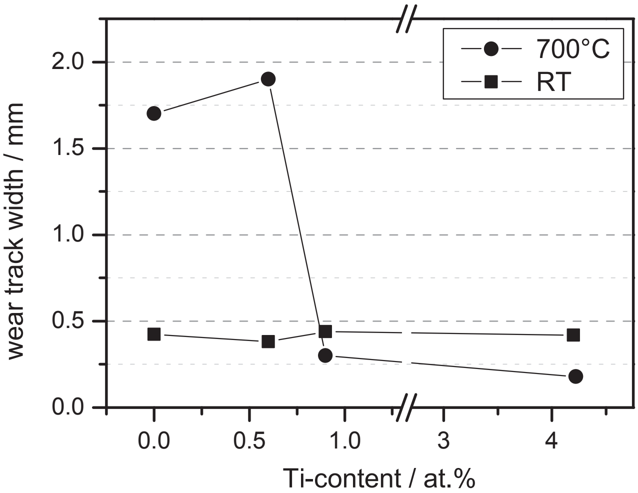

Fig. 9. Influence of increasing Ti-content on wear.

In order to clarify the changed tribological behavior for medium and higher Ti-contents at 700°C, Raman measurements were conducted on all samples within and outside the wear track. SEM investigations were done on the 700°C wear tracks, showing different wear mechanisms, exemplarily displayed for the undoped and the highest Ti-containing coating in Fig. 10. The magnification of the overview is higher for the 4.2 at.% Ti-containing coating because of the much smaller wear track (cf. Fig. 9), while both details are recorded with the same magnification. In case of the undoped coating, the wear track shows a lot of transferred material which originates mainly from the ball (Fig. 10a). The coating with a Ti-content of 0.6 at.% shows a very similar wear track which is slightly broader (cf. Fig. 9) but appears somewhat rougher. For a Ti-content of 4.2 at.%, there are some dark areas and spots present within the wear track, but no grooves or debris are visible (Fig. 10b). Also the 0.9 at.% Ti-containing coating shows a comparable behavior, with slightly broader wear track, again comprising of dark areas and more or less unaffected regions in between. By Raman measurements only alumina [41] was detected within the rough wear tracks of the undoped and low Ti-containing coatings. Measurements within the narrow wear tracks on the 0.9 and 4.2 at.% Ti-containing samples reveal that the dark regions mainly consist of rutile [42] (Fig. 10c – spectrum I) while alumina is detected on the unaffected areas in between [41] (Fig. 10c – spectrum II). Rutile is also detected outside the wear track after the ball-on-disc test at 700°C, but not after room-temperature ball-on-disc test. It can be concluded that at high temperature rutile forms on the coating surface, which is plastically deformed and partially removed by the ball in the sliding contact and subsequently back-transferred to the wear track. The measured rutile Raman peaks show small deviations from the ideal peak position which are possibly caused by non-stoichiometry [43] and local residual stresses [44] induced in the tribo-contact. GAXRD measurements showed that the Ti-sub-oxide (Ti_3O_5) occurring for the 4.2 at.% Ti containing coating in the as-deposited state is partly transformed to TiO_2 after the 700°C ball-on-disc test. However, there is still Ti_3O_5 left which changes the overall stoichiometry and could influence the rutile peak-position.

Taking into account the results obtained by Raman spectroscopy and SEM, the reduced friction coefficient for the medium and high Ti-containing coatings can be attributed to the presence of rutile in the wear track [45, 46]. The tribological results at room temperature suggest that this friction reducing mechanism is only active at elevated temperatures for mixtures of alumina with a sufficient amount of titanium oxide.

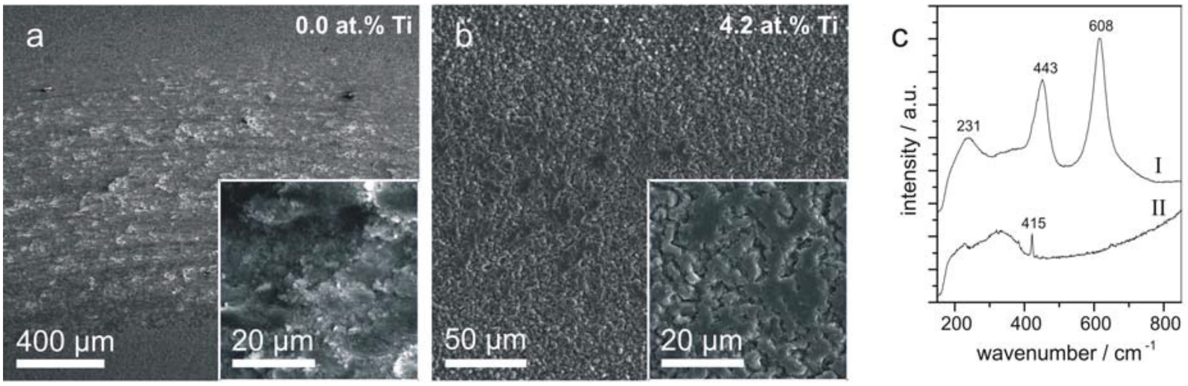

Fig. 10. SEM images of wear tracks obtained during 700°C ball-on-disc testing: undoped alumina coating (a), 4.2 at.% Ti-containing coating (b). The overview micrograph of the undoped coating is displayed with a lower magnification compared to the doped one, while both details exhibit the same magnification. Raman measurements (c) within the wear track of the 4.2 at.% Ti containing coating, showing one measurement at a dark spot (I, rutile) and one in between (II, alumina).

4. Conclusions

Alumina coatings deposited by low-pressure CVD tolerate a low $TiCl_4$ addition to the precursor gas mixture which is limited by powder formation in connection with a decreased deposition rate. The coatings comprise two phases for higher (α-Al_2O_3, Ti_3O_5) as well as for medium $TiCl_4$ flow rates (α-Al_2O_3, Ti_2S_3). The low Ti solubility limit of alumina, the unaffected α-Al_2O_3 lattice parameter and XPS investigations suggest that also for low Ti-contents a small fraction of Ti-oxide is formed which is below the detection limit of GAXRD. The hardness decreases slightly with increasing Ti-content due to the lower hardness of the second phase. Coatings with a detectable second phase show significantly reduced friction and wear at 700°C, caused by the formation of rutile on the coating surface, which efficiently separates sample and counterpart in the sliding contact. An increased Ti-content results in a friction coefficient decreasing from 0.7 to 0.85 for undoped to low Ti-containing coatings to 0.5 to 0.4 for medium to high Ti-contents. No rutile is detected after room temperature ball-on-disc tests where Ti-doping just slightly affects friction and wear. Nevertheless, the obtained results strongly indicate that doping of alumina coatings with Ti in the range of a few atomic percent improves their tribological behavior significantly.

Acknowledgement

Financial support by the Austrian Kplus Competence Center Programme is gratefully acknowledged. The authors are grateful to DI A. Fian from Joanneum Research in Weiz for the support regarding the XPS analysis, to G. Hawranek for SEM investigations and to Dr. G. Fontalvo for valuable discussions.

References

[1] M.J. Capitan, A. Stabel, J.C. Sanchez-Lopez, A. Justo, A.R. Gonzalez-Elipe, S. Lefebvre, A. Fernandez, Appl. Surf. Sci. 161/1-2 (2000) 209.

[2] K.A. Habib, J.J. Saura, C. Ferrer, M.S. Damra, E. Gimenez, L. Cabedo, Surf. Coat. Technol. 201/3-4 (2006) 1436.

[3] F. Halitim, N. Ikhlef, S. Abdeslam, G. Fantozzi, Ceramics International 23/6 (1997) 509.

[4] T. Nagai, K. Wasa, S. Hayakawa, J. Mater. Sci. 11/8 (1976) 1509.

[5] M. Kathrein, W. Schintlmeister, W. Wallgram, U. Schleinkofer, Surf. Coat. Technol. 163-164 (2003) 181.

[6] B. Lux, C. Colombier, H. Altena, K. Stjernberg, Thin Solid Films 138/1 (1986) 49.

[7] B. Lux, R. Haubner, C. Wohlrab, Surf. Coat. Technol. 38/3 (1989) 267.

[8] S. Ruppi, J. Phys. IV 11/PR3 (2001) 847.

[9] C. Chatfield, J.N. Lindstrom, M.E. Sjostrand, J. de Physique 50/C-5 (1989) 377.

[10] M. Halvarsson, H. Norden, S. Vuorinen, Surf. Coat. Technol. 61/1-3 (1993) 177.

[11] A. Larsson, M. Halvarsson, S. Vuorinen, Surf. Coat. Technol. 94-5/1-3 (1997) 76.

[12] A. Larsson, M. Halvarsson, S. Vuorinen, Int. J. Refract. Met. Hard Mat. 16/4-6 (1998) 369.

[13] S. Ruppi, Int. J. Refract. Met. Hard Mat. 23/4-6 (2005) 306.

[14] M. Astrand, T.I. Selinder, F. Fietzke, H. Klostermann, Surf. Coat. Technol. 188-89 (2004) 186.

[15] T. Leyendecker, I. Rass, G. Erkens, M. Feldhege, Surf. Coat. Technol. 97/1-3 (1997) 790.

[16] H. Schulz, J. Dorr, I.J. Rass, M. Schulze, T. Leyendecker, G. Erkens, Surf. Coat. Technol. 146 (2001) 480.

[17] A. Schütze, D.T. Quinto, Surf. Coat. Technol. 162/2-3 (2003) 174.

[18] C. Colombier, J. Peng, H. Altena, B. Lux, Int. J. Refract. Hard Met. 5/2 (1986) 82.

[19] E. Fredriksson, J.O. Carlsson, Thin Solid Films 263/1 (1995) 28.

[20] M. Halvarsson, S. Vuorinen, Int. J. Refract. Met. Hard Mat. 15/1-3 (1997) 169.

[21] M. Danzinger, J. Peng, R. Haubner, B. Lux, J. de Physique II 1/C2 (1991) 571.

[22] S. Vuorinen, J. Skogsmo, Thin Solid Films 193/1-2 (1990) 536.

[23] M. Olsson, S. Hogmark, in: M. Nishimura (Ed.), Proc. Int. Tribology Conf., Jap. Soc. of Tribol., Yokohama, 1995, p. 569.

[24] S. Hashimoto, A. Tanaka, A. Murata, T. Sakurada, Surf. Sci. 556/1 (2004) 22.

[25] M. Oku, H. Matsuta, K. Wagatsuma, Y. Waseda, S. Kohiki, J. Electron Spectrosc. Relat. Phenom. 105/2-3 (1999) 211.

[26] C.D. Wagner, W.M. Riggs, L.E. Davis, J.F. Moulder, Handbook of X-ray Photoelectron Spectroscopy, Perkin-Elmer Corp., Eden Prairie, Minnesota, 1979.

[27] D. Leinen, A. Fernandez, J.P. Espinos, J.P. Holgado, A.R. Gonzalez-Elipe, Appl. Surf. Sci. 68/4 (1993) 453.

[28] J.L. Li, M.R. Sun, X.X. Ma, Appl. Surf. Sci. 252/20 (2006) 7503.

[29] J.T. Kloprogge, L.V. Duong, B.J. Wood, R.L. Frost, J. Colloid Interface Sci. 296/2 (2006) 572.

[30] V.I. Nefedov, D. Gati, B.F. Dzhurinskii, N.P. Sergushin, Y.V. Salyn, Russian J. Inorganic Chemistry 20/9 (1975) 2307.

[31] G. Hopfengartner, D. Borgmann, I. Rademacher, G. Wedler, E. Hums, G.W. Spitznagel, J. Electron Spectrosc. Relat. Phenom. 63/2 (1993) 91.

[32] L. Ramqvist, K. Hamrin, Johansso.G, A. Fahlman, C. Nordling, J. Phys. Chem. Solids 30/7 (1969) 1835.

[33] G.B. Harris, Phil. Mag. 43/336 (1952) 113.

[34] W. Swiatnicki, S. Lartiguekorinek, J.Y. Laval, Acta Metall. Mater. 43/2 (1995) 795.

[35] P. Bansal, P.H. Shipway, S.B. Leen, Surf. Coat. Technol. 200/18-19 (2006) 5318.

[36] A. Mezin, Acta Metall. Mater. 43/8 (1995) 3151.

[37] S.M. Hu, J. Appl. Phys. 50/7 (1979) 4661.

[38] W. Kreher, A. Molinari, J. Mech. Phys. Solids 41/12 (1993) 1955.

[39] H. Holleck, J. Vac. Sci. Technol. A-Vac. Surf. Films 4/6 (1986) 2661.

[40] E.S. Peters, C.J. Carmalt, I.P. Parkin, J. Mater. Chem. 14/23 (2004) 3474.

[41] S.P.S. Porto, R.S. Krishnan, J. Chem. Phys. 47/3 (1967) 1009.

[42] S.P.S. Porto, P.A. Fleury, T.C. Damen, Phys. Rev. 154/2 (1967) 522.

[43] J.C. Parker, R.W. Siegel, Appl. Phys. Lett. 57/9 (1990) 943.

[44] P. Merle, J. Pascual, J. Camassel, H. Mathieu, Phys. Rev. B 21/4 (1980) 1617.

[45] M.N. Gardos, H.S. Hong, W.O. Winer, Tribol. Trans. 33/2 (1990) 209.

[46] M. Woydt, A. Skopp, I. Dörfel, K. Witke, Wear 218/1 (1998) 84.

Publication II

Proceedings of the 17th Int. Plansee Seminar 2009, Vol. 2, p. 555-564.

The effect of boron doping on thermal CVD of alumina

D. Hochauer[a], C. Mitterer[b], M. Penoy[c], C. Michotte[c], H.P. Martinz[d], M. Kathrein[e]

[a] Materials Center Leoben Forschung GmbH, Roseggerstrasse 12, A-8700 Leoben, Austria
[b] Department of Physical Metallurgy and Materials Testing, University of Leoben, Franz-Josef-Strasse 18, A-8700 Leoben, Austria
[c] CERATIZIT Luxembourg SARL., L-8201 Mamer, Luxembourg
[d] PLANSEE SE, A-6600 Reutte, Austria
[e] CERATIZIT Austria GmbH, A-6600 Reutte, Austria

Abstract

Wear-resistant alumina coatings grown by chemical vapor deposition (CVD) are widely applied on cemented carbide cutting tools. From metallurgy, boron is known to be a highly effective dopant. In order to evaluate its effect on alumina coatings, low-pressure CVD was applied with varied BCl_3 flow-rates and deposition temperatures. To foster B incorporation, $TiCl_4$ was also added.

While boron incorporation without $TiCl_4$ addition was not possible at 1005°C, contents up to 2.4 or 1.3 at% can be reached either by reducing the growth temperature to 850°C or by $TiCl_4$ addition, respectively. α-Al_2O_3 was formed under all conditions, with accompanying $Al_{20}B_4O_{36}$ at high BCl_3 and $TiCl_4$ flow-rates or $Al_4B_2O_9$ phases at low growth temperatures. Hardness increases from 26 to 29 GPa for low boron contents and decreases as the ternary aluminum borate phases appear. Simultaneous doping with small amounts of B and Ti results in a slight reduction of friction at wear rates comparable to undoped alumina, while increasing abrasive wear was observed for the aluminum borate phase containing coatings.

1. Introduction

The modification of alumina with boria is well known for catalyst supports, in order to influence surface activity and texture [1,2]. From the thin-film point-of-view, boron is frequently used as a doping element in layers for semiconductor applications, i.e. materials like Si, Ge or polycrystalline diamond [3,4]. For wear resistant A_2O_3 coatings deposited at atmospheric pressure, B-doping is reported to improve phase stability and cutting performance [5]. Nevertheless, a study dealing with separated variation-series of precursor composition and deposition temperature (T_{dep}) is missing. The aim of this work was the investigation of BCl_3 addition during alumina deposition and the conditions for boron incorporation. Additionally, the influence of $TiCl_4$ and lower T_{dep} was examined. The coatings were deposited by chemical vapor deposition (CVD) at low-pressure (LPCVD) and high temperatures (thermally activated). With exception of BCl_3 and $TiCl_4$ flow-rates, the precursor gas composition was similar to commercial production, as well as the coating architecture. The coating system comprised of TiN and TiCN base-layers, and an outermost alumina monolayer with a desired coating thickness of ~4 µm. Boron incorporation, related phase formation and their impact on hardness and tribological behavior was investigated in detail.

2. Experimental details

Undoped, B-doped and Ti-B-doped alumina monolayer coatings were deposited by LPCVD at a pressure of 80 mbar. The deposition temperature T_{dep} was varied between 850°C and 1005° for one experimental series (B-doped), while two more series were conducted at 1005°C (B- and Ti-B-doped). All coatings were synthesized in an industrial-scale hot-wall CVD plant with radial gas distribution (Bernex BPX 530L). The precursor mixture comprised of the gases $AlCl_3$, BCl_3, CO_2, HCl, H_2S, H_2, and $TiCl_4$ which was the only liquid precursor. In order to provide different amounts of boron, the flow-rate of BCl_3 was varied in the range of 0 to 200 ml min^{-1} (0 - 0.37 vol.%). For Ti-B-doped coatings, a constant $TiCl_4$ flow-rate of 0.2 ml min^{-1} was added (~0.1 vol.%). The composition of the other gases was kept constant and is comparable to state-of-the-art coatings as reported in literature [6-9]. The alumina standard deposition time was set to 180 minutes, but extended to 300 minutes for a second deposition run at 850°C. To improve adhesion and suppress coating/substrate interdiffusion, an ~8 µm thick TiN/TiCN base-layer was applied between cemented carbide (CC) substrates (11 wt.% Co, 4 wt.% TiC, 8 wt.% TaC-NbC, 77 wt.% WC) and alumina. For tribological tests, disc-shaped substrates with a diameter of 30 mm and a thickness of 4 mm were used; all other investigations were performed on flat cemented carbide inserts (12.8 × 12.8 × 4.8 mm^3). Prior to deposition, all substrates were polished and cleaned with a standard procedure comparable to commercial production.

Concentration depth-profiles were determined by glow discharge optical emission spectroscopy (GDOES) with a Jobin-Yvon Horiba JY10000RF equipment. The given chemical compositions were calculated by averaging these concentration values within the respective alumina layers. Crystallographic structure and phase formation were determined with glancing angle X-ray diffraction (GAXRD) using Cu *Kα* radiation with an incident angle of 2°. The residual stresses in the alumina layer were analyzed with the $\sin^2\psi$-method. All XRD measurements were conducted with a Panalytical X'Pert Pro diffractometer. Coating top-view morphology was investigated with a scanning electron microscope (SEM, Zeiss EVO 50) and the coating thickness was determined on SEM fracture cross-section images. Hardness and Young's modulus were assessed by nanoindentation on diamond-polished coating surfaces, using a UMIS system with a Berkovich indenter, and loads stepwise increased from 1 to 50 mN for each measurement. Coating heat treatment was conducted in a Carbolite RHF 1600 and the changes in mass were measured with a Scaltec SBC 21 balance. The tribological characterization was performed on CSM ball-on-disc tribometers at room temperature and 700°C with a 6 mm diameter alumina ball counterpart. Normal-load sliding-distance combinations of 10 N for 500 m and 5 N for 100 m were used for room temperature and high temperature tests, respectively. For all tests, a tangential sliding speed of 0.1 m/s and a wear track radius of 5 mm were selected. The depth of the wear tracks was measured with a Wyko NT1000 3D profiling system (white light interferometry). Selected wear tracks were investigated with Raman spectroscopy, using a Jobin-Yvon LabRam confocal Raman spectrometer (Nd-YAG laser, wavelength: 532.2 nm, power: 10 mW). Several measurements were performed within and outside the wear track after a calibration procedure on silicon, polyethylene and calcite.

3. Results and discussion

The influence of BCl_3 addition on the boron content of alumina coatings deposited under different conditions is shown in Fig. 1. Lower T_{dep} favor the incorporation of boron and decrease the coating growth rate from 1.2±0.1 $\mu m\ min^{-1}$ (1005°C) to ~0.6 $\mu m\ min^{-1}$ (850°C). Starting from very low values at 1005°C and 950°C (~20 ppm), the boron content increases to 0.46 at.% at 900°C. At 850°C, the boron content raises further to 1.2 at.% and 2.4 at.% for a coating thickness of 1.5 μm and 3.2 μm, respectively. The thinner coating was deposited with the standard time (180 minutes), while the low deposition rate was compensated for the thicker coating with a longer deposition time (300 minutes). For the highest T_{dep} (1005°C), BCl_3 addition up to 200 $ml\ min^{-1}$ does not cause an increased boron content within the coating. On the other hand, an additional small amount of $TiCl_4$ (0.2 ml min^{-1}) favors boron incorporation also at 1005°C, already at a comparatively low BCl_3 flow-rate (90 ml min^{-1}). A combination of 150 ml min^{-1} BCl_3 and 0.2 ml min^{-1} $TiCl_4$ increases the boron content to 1.3 at.% and the deposition rate to ~4 µm h^{-1}.

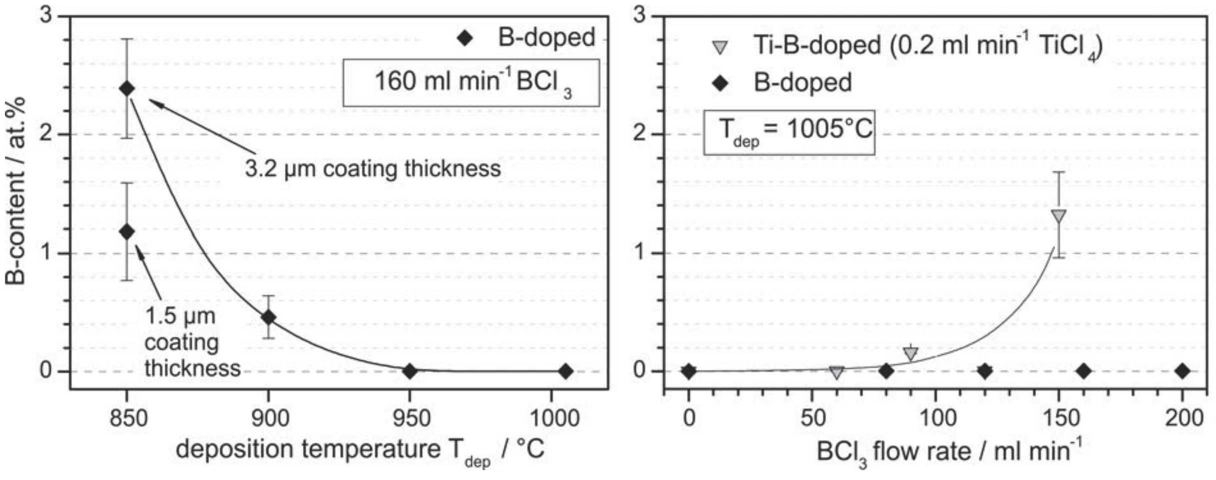

Fig. 1. Boron content, detected with GDOES within the alumina layer, for varied T_{dep} and BCl_3 flow-rate.

A comparison of boron concentration depth profiles for the temperature variation series (GDOES measurements, Fig. 2) shows the tendency of boron segregation near the surface and at the TiCN/CC interface. As visible in the detailed concentration profile shown in the inserts in Fig. 2, this enrichment occurs also for the low boron containing coatings, deposited at 1005°C and 950°C. The coating grown at 900°C shows a maximum in boron concentration underneath the surface and a less pronounced peak at the TiCN/CC interface. Nevertheless, the increasing boron content within the outermost layer (left of the dashed line in Fig. 2) is clearly visible with decreasing T_{dep}, only the coatings deposited at 850°C show an additional increased boron content within the TiCN layer (~100 ppm) compared to coatings grown at higher temperatures (~50 ppm). Most probably, the high boron amount within the outermost layer causes a pronounced diffusion of boron into the TiCN layer. The Ti-B-doped coating (150 ml min^{-1} BCl_3, $T_{dep} = 1005$°C) also shows an increased boron content within the TiCN layer, as the boron amount within the outermost layer is also relatively high. Additionally, the higher T_{dep} enhances diffusion; hence the boron concentration is much higher within the TiCN layer (average concentration: ~0.16 at.% B) and within the CC substrate (Fig. 2). Also for this sample, a small concentration peak indicates boron segregation on the TiCN/CC interface.

SEM top-view images (Fig. 3) show the influence of the varied deposition parameters on coating morphology. The addition of BCl_3 causes slightly smaller grain size and a coating surface which is formed by distinct facets compared to less clearly shaped grains in the undoped coating (Fig. 3a). This changed coating top-view morphology is comparable for all investigated BCl_3 additions, i.e. all alumina coatings deposited at 1005°C with BCl_3 (80 – 200 ml min^{-1}) look similar. Hence, only one example is displayed here (160 ml min^{-1} BCl_3, Fig. 3b). The grain size is decreasing with decreasing T_{dep}, as shown for the coating deposited at 850°C (Fig. 3c) which contains small grains but also a few medium size grains compared to the relatively large grains visible for the undoped coating (Fig. 3a). The clear appearance of crystal facets is also visible for a combination of low Ti- and low B-doping (90 ml min^{-1} BCl_3 + 0.2 ml min^{-1} $TiCl_4$, Fig. 3d), however, with increasing grain size. The fast growing Ti-B-doped coating (150 ml min^{-1} BCl_3 + 0.2 ml min^{-1} $TiCl_4$, Fig. 3e) shows much bigger grains, which can be mainly related to its higher coating thickness of ~12 μm.

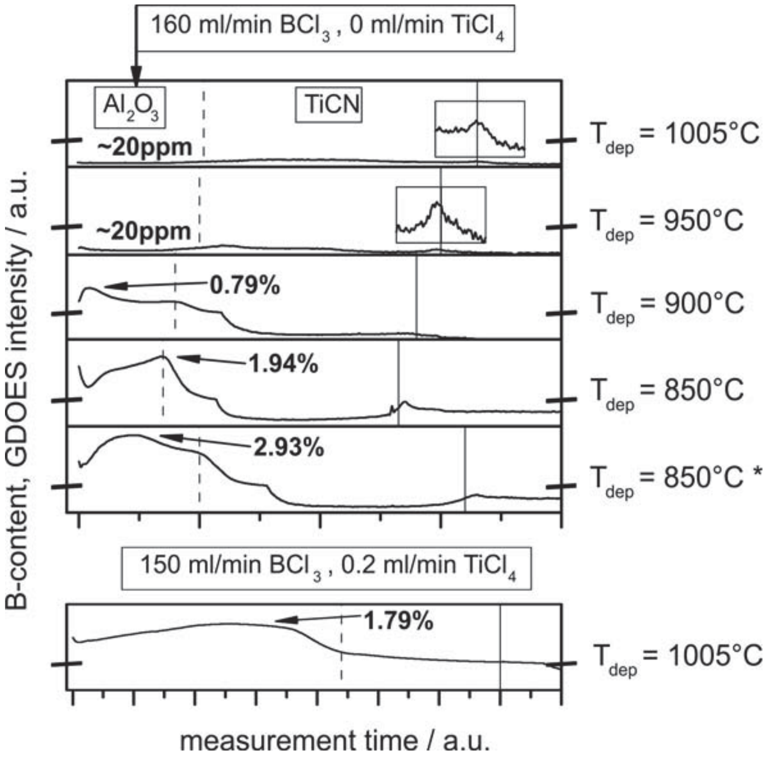

Fig. 2. Boron concentration depth-profiles (GDOES) of B-doped alumina coatings with decreasing deposition temperature, compared to a Ti-B-doped coating below. The coating marked with (*) was deposited for 300 minutes, instead of 180 minutes standard alumina deposition time. The Al_2O_3/TiCN and the TiCN/CC interfaces are indicated with dashed and solid lines, respectively. The inserts shown for T_{dep} = 950°C and 1005°C are displayed with a relative magnification factor of ten.

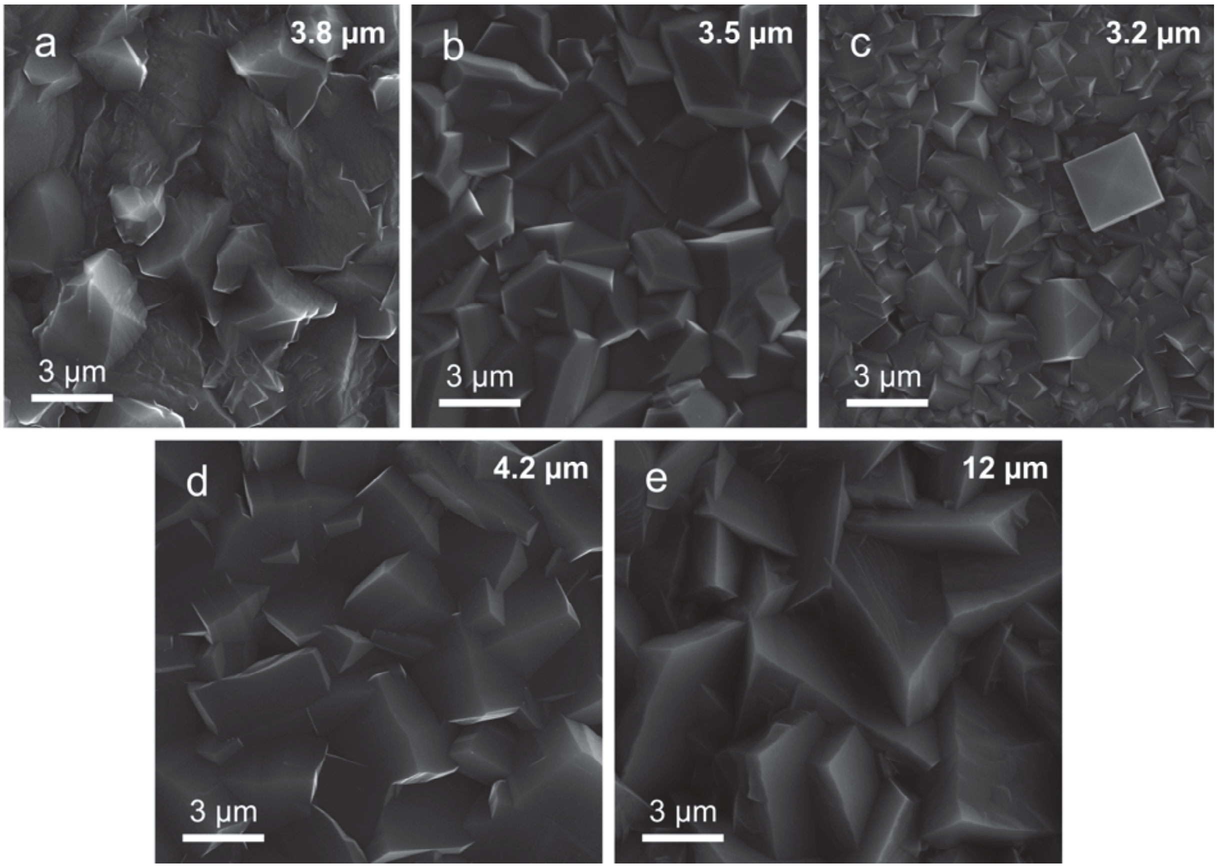

Fig. 3. SEM coating morphology: undoped (a); B-doped: 160 ml min^{-1} BCl_3 (b), 160 ml min^{-1} BCl_3 + T_{dep} = 850°C (c); Ti-B-doped: 90 ml min^{-1} BCl_3 + 0.2 ml min^{-1} $TiCl_4$ (d), 150 ml min^{-1} BCl_3 + 0.2 ml min^{-1} $TiCl_4$ (e). The deposition temperature was constant at 1005°C for (a, b, d, e). The coating thickness of the outermost layer is displayed in the top right corner of each micrograph.

At T_{dep} = 1005°C, the GAXRD patterns, mainly showing α-Al_2O_3 (JCPDF # 00-010-0173) and TiCN, are very similar for undoped (Fig. 4a) and B-doped coatings (e.g. 160 ml min^{-1} BCl_3, Fig. 4b), i.e. the different top-view coating morphology (cf. Fig. 3) is not connected with a visible change in phase composition or texture. Lower T_{dep} result in a small amount of κ-Al_2O_3 at 950°C and the formation of an aluminum borate phase within the range of 850°C to 900°C (Fig. 4c), which shows a stoichiometry like $Al_4B_2O_9$ (JCPDF # 01-079-1477). An aluminum borate phase also appears for the addition of 150 ml min^{-1} BCl_3 and 0.2 ml min^{-1} $TiCl_4$ at T_{dep} = 1005°C. This phase seems to have a stoichiometry comparable to $Al_{20}B_4O_{36}$ (JCPDF # 01-080-2301), which is supported by the occurrence of peaks at 20.3° and 28.7° (Fig. 4d). The observed dependency of stoichiometry on temperature is in agreement with thermodynamic equilibrium [10] and also reported for the production of aluminum borate whiskers [11-14]. Moreover, the higher content of boron within the aluminum borate deposited at 850°C explains the still increasing boron content within the coating, while its phase fraction (Fig. 4c) seems to be lower compared to the Ti-B-doped coating (Fig. 4d). In general, different types of aluminum borates show similar XRD patterns and the unambigous detection of small changes in stoichiometry (e.g. $Al_{18}B_4O_{33}$ vs. $Al_{20}B_4O_{36}$) is not possible.

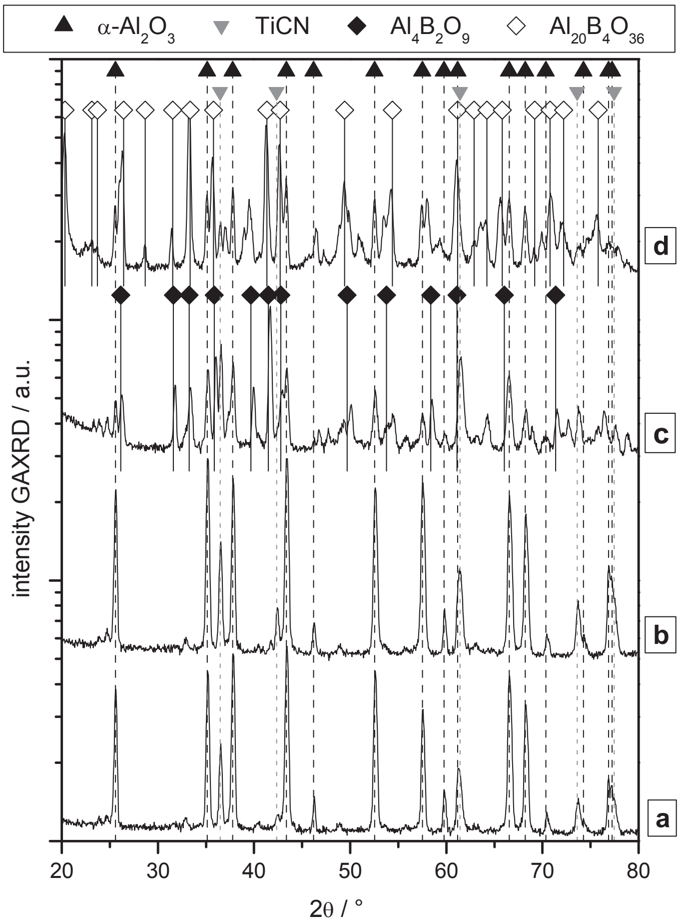

Fig. 4. Selected GAXRD patterns: undoped alumina (a), B-doped alumina (160 ml min^{-1} BCl_3, b), B-doped alumina deposited for 300 minutes (T_{dep} = 850°C, 160 ml min^{-1} BCl_3, c), Ti-B-doped coating (150 ml min^{-1} BCl_3 + 0.2 ml min^{-1} $TiCl_4$, d). T_{dep} is constant at 1005°C for (a), (b) and (d).

For each investigated coating, the α-Al_2O_3 lattice parameters a and c range from 4.76 Å to 4.77 Å and from 12.98 Å to 13.00 Å, respectively. Thus, the lattice of the alumina phase is very similar to the standard values α-Al_2O_3 (a: 4.758 Å, c: 12.991 Å, JCPDF # 00-010-0173). The residual tensile stresses for B-doped alumina coatings deposited at 950°C and 1005°C were measured to vary between 490 MPa and 610 MPa. The coating deposited at 900°C showed a lower stress value (290 MPa), which can be attributed to the lower coating thickness and the lower difference between its T_{dep} and room temperature (i.e., lower thermal mismatch). For Ti-B-doped coatings slightly lower stress values have been observed (320 –

450 MPa). However, residual stress values were detected using the (116) α-Al_2O_3 peak only for coatings which mainly contsist of alumina.

Hardness measurements revealed increasing values for B-doped alumina coatings, deposited with low and medium BCl_3 flow-rates (80 – 160 ml min^{-1}, Fig. 5a) which could be partly attributed to the slightly decreased grain size. However, the lower hardness value for 200 ml min^{-1} BCl_3, where the grains are comparable in size and shape, is not understood yet. The addition of 0.2 ml min^{-1} $TiCl_4$ suppresses this hardness increase (Fig. 5c), which could be related to the increasing grain size for these coatings. Furthermore, a combination of $TiCl_4$ and higher BCl_3 flow-rate (150 ml min^{-1}) causes a drop in hardness. Decreasing T_{dep}, from 1005°C to 850°C, consequences a continuously decreasing hardness value from 27.4 GPa to 21.0 GPa, respectively (Fig. 5b). In connection with an increasing fraction of the aluminum borate phase with increasing boron content, these tendencies could be explained with the lower hardness reported for aluminum borate whiskers. Nanoindentation tests on single whiskers revealed hardness values of 10.4±0.3 GPa ($Al_4B_2O_9$) and 12.8±0.4 GPa ($Al_{18}B_4O_{33}$) [11]. Although these whiskers are about one order of magnitude smaller, compared to the aluminum borate grains in this work, their comparatively low hardness seems to be a reasonable explanation for the lower hardness of those coatings containing borate phases. The lowest hardness value (~18.4 GPa), measured for the Ti-B-doped coating deposited with 150 ml min^{-1} BCl_3, could consequently result from the highest aluminum borate content (cf. Fig. 4d) and the coarsest grain (cf. Fig. 3e).

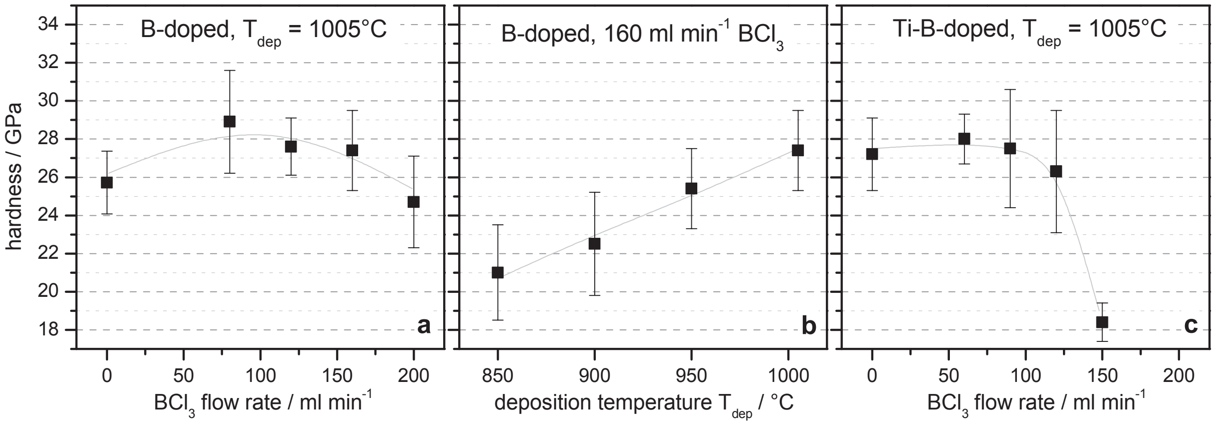

Fig. 5. Hardness of B-doped coatings deposited with varied BCl_3 flow-rate (a) and with varied T_{dep} (b), compared to Ti-B-doped coatings deposited with 0.2 ml min^{-1} $TiCl_4$. Measurements were performed on polished surfaces with increasing indentation force (1-50 mN).

The oxidation protection capability of each coating was characterized with measurements of the mass gain after a 2 hours heat treatment at 1000°C in ambient air. Subsequently performed GAXRD measurements showed the dominating formation of titanium oxide, while only a smaller peak-set of alumina is detected. Therefore, lower mass gain should be an indicator for less titanium and oxygen diffusing through the outermost coating, i.e. the diffusion barrier efficiency of the coating. In particular, B-doped coatings deposited with medium BCl_3 flow-rates (120 – 160 ml min^{-1}, Fig. 6) possessed the lowest mass gains, but no improvement is visible for the highest BCl_3 flow-rate. Mass gain values for Ti-B-doped coatings are more scattering and their higher average values can be related to a denser crack network as visible on polished samples. The mass gain is also increased to 6 mg and 9 mg for coatings deposited at 900°C and 950°C, respectively. The lowest T_{dep} (850°C) caused the highest mass gain (~160 mg), which could be related to the biggest difference between deposition and testing temperature. As the heat treatment is conducted 150°C above T_{dep}, thermally activated transformations are more likely, which could deteriorate the integrity of this coating.

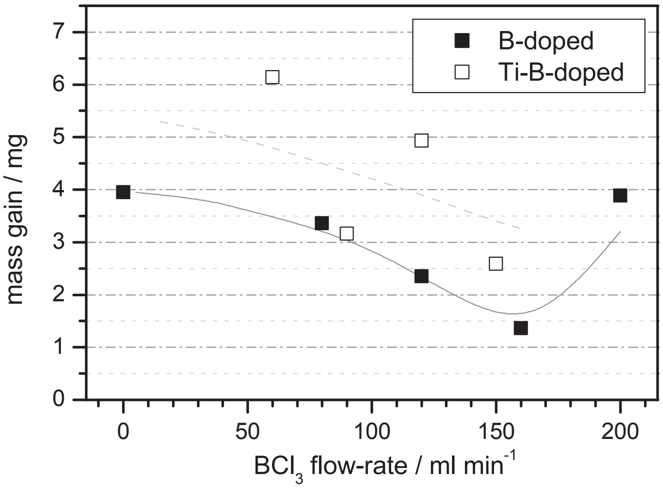

Fig. 6. Mass gain measured after a 2 hours heat treatment at 1000°C in ambient air. Comparision of B-doped and Ti-B-doped alumina coatings deposited at 1005°C.

Fig. 7 presents the summarized friction coefficients, determined with ball-on-disc tests at room temperature (open circles) and 700°C (solid triangles). The scattering of the steady-state friction coefficient, as visible in a friction vs. sliding-distance plot, is indicated by the error bars. At room temperature, all friction coefficients (μ_{RT}) are in the range of ~0.5 to ~0.7 and all friction curves show very low scattering. There seems to be a slight friction reducing effect for B-doped and Ti-B-doped coatings, deposited at 1005°C with low and medium BCl_3 flow-rates, respectively (Figs. 7a, c). However, the reduced T_{dep} and the consequently raised boron content results in a slight increase of μ_{RT} (Fig. 7b). At 700°C, the friction coefficient (μ_{700}) decreases to ~0.5 for B-doped coatings ($T_{dep} = 1005°C$) compared to μ_{700}~0.7 for undoped samples (Fig. 7a). For $T_{dep} = 950°C$, the μ_{700} value is still at ~0.45, but it increases rapidly as the aluminum borate phase appears at lower T_{dep} (Fig. 7b). This suggests that small amounts of κ-Al_2O_3, even if undetectable with GAXRD, could decrease high temperature friction. Ti-B-doping causes an increased μ_{700} with big changes in scattering, which do not correlate with the increasing BCl_3 flow-rate (Fig. 7c). Nevertheless, the aluminum borate phase containing coating deposited at 1005°C (150 ml min^{-1} BCl_3 + 0.2 ml min^{-1} $TiCl_4$, Fig. 7c) shows a slightly lower μ_{700} compared to coatings deposited below 950°C (Fig. 7b).

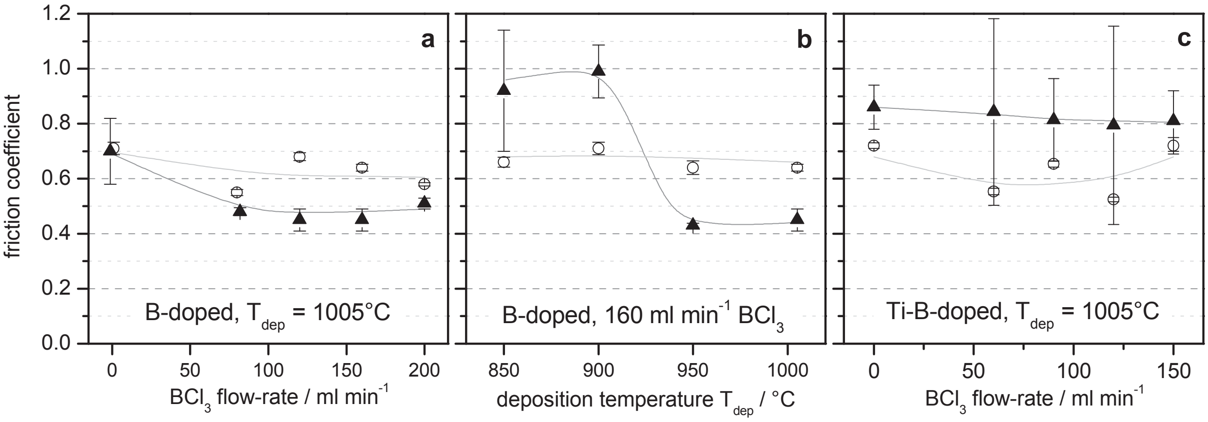

Fig. 7. Ball-on-disc friction coefficient at room temperature (open circles) and at 700°C (solid triangles) for B-doped coatings (a, b) and Ti-B-doped coatings (0.2 ml min^{-1} $TiCl_4$, c).

Optical profiler measurements show little influence of B-doping on the wear behavior at RT. While the wear track of the undoped coating (Fig. 8a) comprises lots of smaller grooves, for low and medium BCl_3 flow-rates (e.g. Fig. 8b), there are less grooves which are slightly deeper, and. the wear track looks on average smoother. For the highest BCl_3 flow-rate, there are only small grooves visible and the track is even smoother (Fig. 8c). Comparable wear tracks are also found for Ti-B-doped coatings. The deepest RT wear track (~3 µm) is detected for the 12 µm thick Ti-B-doped coating deposited with 150 ml min^{-1} BCl_3, which contains a big amount of aluminum borate phase (Fig. 8d). Similarly, coatings deposited at lower T_{dep} show a lower wear resistance with increasing aluminum borate content (Figs. 8e, f). Obviously, the lower hardness of the borate phase decreases the resistance against abrasive wear and, consequently, the softest coating shows the deepest wear track.

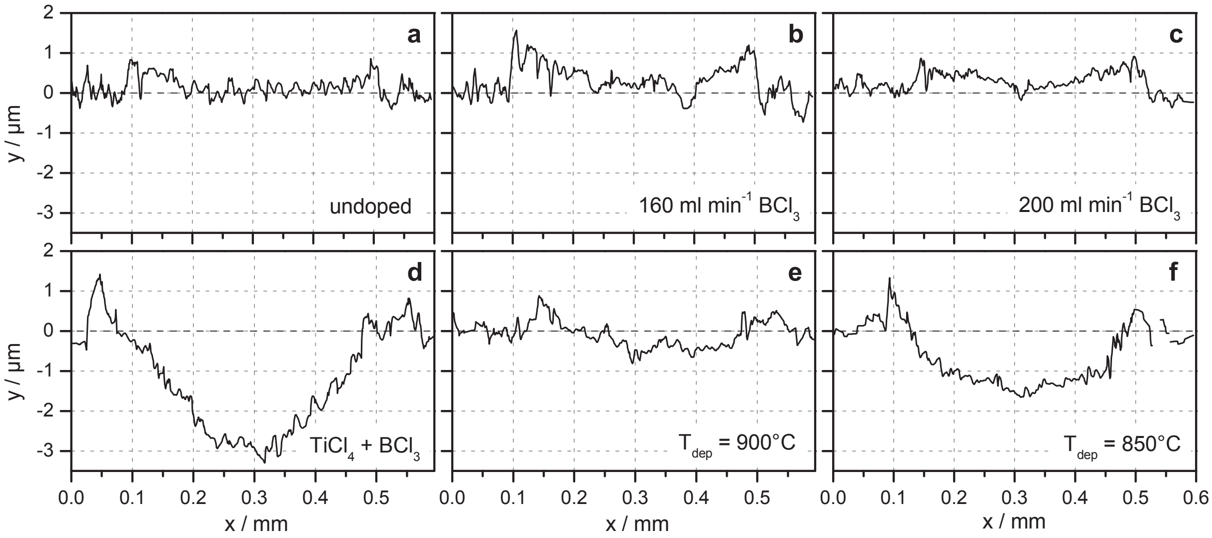

Fig. 8. Wear tracks after RT ball-on-disc tests, measured with white-light profilometry, for undoped (a), B-doped (b, c), Ti-B-doped coatings (150 ml min^{-1} BCl_3 + 0.2 ml min^{-1} $TiCl_4$, d) and lower T_{dep} (e, f).

At 700°C, all coatings show a much broader wear track (Fig. 9). Hence, all profiler measurements were performed at lower magnification, compared to the samples tested at RT. At elevated testing temperature, low and medium BCl_3 flow-rates result in a much narrower wear track (e.g. Fig. 9b) compared to the undoped sample (Fig. 9a). Only for the highest BCl_3 flow-rate the wear resistance is reduced, causing an ~2 µm deep groove (Fig. 9c). Simultaneously, B-doping weakens the coating adhesion at the Al_2O_3/TiCN interface, causing holes outside the wear track after the 700°C ball-on-disc test, with a depth comparable to the alumina coating thickness (Figs. 9b, c). The surface density of these holes increases with decreasing T_{dep} or with increasing BCl_3 flow-rate (up to 160 ml min^{-1}). However, the coating deposited with the highest BCl_3 flow-rate shows less holes. Also for Ti-B-doped coatings, adhesion deteriorates with the addition of BCl_3 (Fig. 9e) compared to $TiCl_4$ addition only (Fig. 9d), where no holes are detected. In the Ti-B-doped series, the wear tracks are similar to the undoped coating, until the aluminum borate phase appears (Fig. 9f). The absence of holes outside this wear track is rather attributed to the higher coating thickness, as the thinner borate containing coatings grown below 950°C also show adhesion failures (Figs. 9h, i). Nevertheless, local adhesion failure occurs in the center of this wear track, but no grooves deeper than 6 µm are visible. In general, coatings containing high aluminum borate amounts show deeper wear tracks, when compared to the respective RT wear track. For the coating deposited at 850°C, the low wear resistance consequences a wear track which already reaches the TiCN base-layer (Fig. 9i), where further wear could be stopped by this harder phase [15]. As the borate-containing Ti-B-doped coating is much thicker, the base-layer is not able to retard the penetration of the counterpart, which could explain the much deeper wear track shown in Fig. 9f.

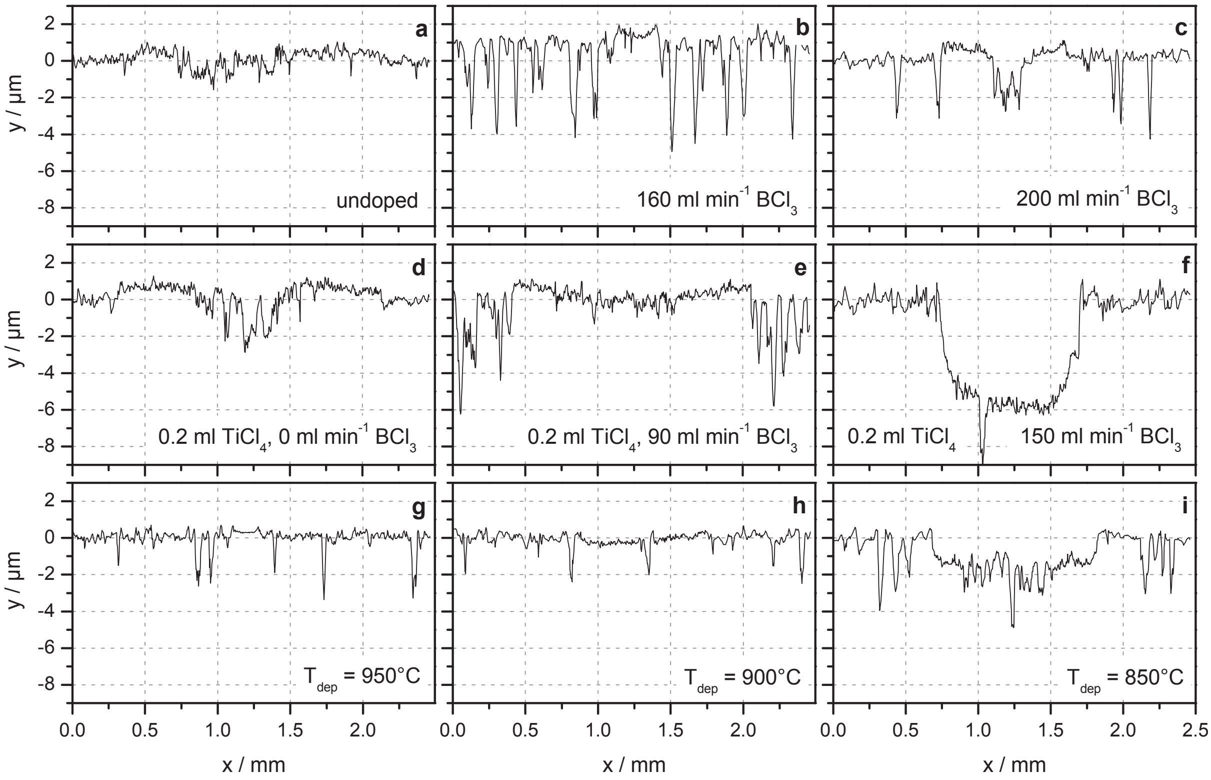

Fig. 9. Wear tracks after 700°C ball-on-disc tests, measured with white-light profilometry, for undoped (a), B-doped (b, c), Ti-doped (d), Ti-B-doped coatings (e, f) and lower T_{dep} (g – i).

The narrow wear tracks visible for medium BCl_3 flow-rates (e.g. Fig. 9b) and for $T_{dep} = 950°C$ (e.g. Fig. 9g), have been the objective of extensive Raman spectroscopy investigations. Nevertheless, no species beside alumina could be detected within these wear tracks. Furthermore, the changed coating morphology could have a decisive influence on initial testing conditions and the first formation of wear debris. A different kind of debris, mainly consisting of alumina, could separate sample surface and counterpart in the sliding contact. However, this approach could not explain the lower wear resistance for the coating deposited with the highest BCl_3 flow-rate, which possesses the same morphology. Thus, further methods are necessary, in order to clarify if tribologically active species or layers are formed within these wear tracks. Additionally, the formation of a volatile boron containing phase could impede an ex-situ detection. The lower μ_{700} of these samples can be explained with the smaller area in contact, hence less asperities are interlocking, which reduces friction. The very high μ_{700}, for lower T_{dep}, could be related to the fact that the sliding counterpart already faces the TiCN base-layer. Another influence might be, that for these coating adhesion failures occurred also within the wear track (Figs. 9h, i), which is not the case for coatings without aluminum borate phase.

4. Conclusions

B-doping of alumina coatings grown by low-pressure chemical vapor deposition was investigated, by the variation of precursor gases (BCl_3, $TiCl_4$) and deposition temperature. BCl_3 addition does not increase the boron content at T_{dep} = 1005°C. On the other hand, low to medium BCl_3 flow-rates (T_{dep} = 1005°C) change morphology, increase hardness and improve the high temperature tribological properties. The introduction of $TiCl_4$ at 1005°C favors boron incorporation but no coating hardening and reduced high temperature protection is observed. Coatings deposited below 950°C show an increasing boron content with decreasing T_{dep}. In general, significant boron incorporation is accompanied by the formation of aluminum borate phases which cause lower coating hardness. The tribological behavior at RT is only little influenced by B-doping, except the lower wear resistance of aluminum borate containing coatings. For ball-on-disc tests, performed at 700°C, coatings deposited with low and medium BCl_3 flow-rates at 950°C and 1005°C show lower friction values and improved wear behavior against alumina, when compared to the undoped sample. Aluminum borate containing coatings also show a lower wear resistance at 700°C. In contrast to thermal loads only, the combination of elevated temperatures and mechanical loads during ball-on-disc tests reveals a lower coating adhesion for all B-doped coatings with local failures originating mainly in the Al_2O_3/TiCN interface. In summary, it has been shown that properties of CVD alumina coatings can be improved by B- and Ti-doping, however, controlling the effect of B-dopants at interfaces turned out to be of crucial importance.

Acknowledgment

Financial support by the Austrian Federal Government and the Styrian Provincial Government, within the research activities of the K2 Competence Center on “Integrated Research in Materials, Processing and Product Engineering”, operated by the Materials Center Leoben Forschung GmbH in the framework of the Austrian COMET Competence Center Programme, is gratefully acknowledged.

References

[1] Y. Saih and K. Segawa, Appl. Catal. A 353 (2009) 258.

[2] S. Engels, E. Herold, H. Lausch, H. Mayr, H.-W. Meiners, and M. Wilde, Surf. Sci. Catal. 75/3 (1993) 2581.

[3] Y. Kunii, Y. Inokuchi, A. Moriya, H. Kurokawa, and J. Murota, Appl. Surf. Sci. 224 (2004) 68.

[4] R.B. Jackman, B. Baral, C.R. Kingsley, J.S. Foord, Diamond Relat. Mater. 5 (1996) 378.

[5] M. Kathrein, W. Schintlmeister, W. Wallgram, and U. Schleinkofer, Surf. Coat. Technol. 163-164 (2003) 181.

[6] S. Ruppi, Int. J. Refract. Met. Hard Mater. 23/4-6 (2005) 306.

[7] C. Colombier, J. Peng, H. Altena, and B. Lux, Int. J. Refract. Hard Met. 5/2 (1986) 82.

[8] E. Fredriksson and J.O. Carlsson, Thin Solid Films. 263/1 (1995) 28.

[9] M. Halvarsson and S. Vuorinen, Int. J. Refract. Met. Hard Mater. 15/1-3 (1997) 169.

[10] E.M. Levin, C.R. Robbins, and H.F. McMurdie, Phase Diagrams for Ceramists, M.K. Reser (ed.), Am. Ceram. Soc., Columbus, Ohio, (1964), p. 121

[11] X. Tao, X. Wang, and X. Li, Nano Letters. 7/10 (1995) 3172.

[12] Y. Liu, Q. Li, and, S. Fan, Chem. Pys. Lett. 375 (2003) 632.

[13] R. Ma, Y. Bando, and T. Sato, Appl. Phys. Lett. 81/18 (2002) 3467.

[14] Y. Li and R.P.H. Chang, Mater. Chem. Phys. 97 (2006) 23.

[15] J. Wagner, D. Hochauer, C. Mitterer, M. Penoy, C. Michotte, W. Wallgram, and M. Kathrein, Proc. 16th Int. Plansee Seminar, Vol. 2, G. Kneringer, P. Rödhammer, and H. Wildner (Eds.), Reutte, Austria, (2005), p. 917-931

Publication III

in manuscript

Carbon doped alumina coatings grown by thermally activated CVD

D. Hochauer[a], C. Mitterer[b], M. Penoy[c], C. Michotte[c], S. Puchner[d,e], H. Hutter[e],
H.P. Martinz[f,*], M. Kathrein[g]

[a)] Materials Center Leoben Forschung GmbH, Roseggerstrasse 12, A-8700 Leoben, Austria
[b)] Department of Physical Metallurgy and Materials Testing, Montanuniversität Leoben, Franz-Josef-Strasse 18, A-8700 Leoben, Austria
[c)] CERATIZIT Luxembourg SARL, L-8201 Mamer, Luxembourg
[d)] Kompetenzzentrum Automobil- und Industrieelektronik GmbH, Europastraße 8, A-9524 Villach, Austria
[e)] Institute for Chemical Technologies and Analytics, Vienna University of Technology, Getreidemarkt 9, A-1060 Vienna, Austria
[f)] PLANSEE SE, A-6600 Reutte, Austria
[g)] CERATIZIT Austria GmbH, A-6600 Reutte, Austria

[*] The authors regret to note that their co-author Hans-Peter Martinz suddenly passed away during preparation of this manuscript.

Abstract

Alumina (Al_2O_3) coatings deposited by chemical vapor deposition (CVD) with different modifications and dopants are widely applied as wear resistant coatings on cemented carbide cutting tools. The aim of this work was to investigate the influence of CH_4 addition on the deposition of Al_2O_3 by low pressure chemical vapor deposition (LPCVD). The coatings were deposited at 1005°C on a TiN-TiCN base layer using a precursor gas mixture of $AlCl_3$, CH_4, CO_2, HCl, H_2S, and H_2. Coating characterization was conducted by scanning electron microscopy (SEM), glow discharge optical emission spectroscopy (GDOES), X-ray photoelectron spectroscopy (XPS), time-of-flight secondary ion mass spectrometry (ToF-SIMS), glancing angle X-ray diffraction (GAXRD), nanoindentation and tribological ball-on-disc tests against Al_2O_3 balls. Additionally, the ball-on-disc wear tracks were investigated by Raman spectroscopy.

The highest carbon doping content achieved in this study was in the range of 0.5 – 1.0 at.%. SEM top-view images indicate a less facetted coating topography with slightly bigger grains for C-doped coatings. GAXRD patterns show the α-Al_2O_3 modification for undoped and C-doped coatings with only minor differences concerning lattice parameters, preferred orientation and stresses. The hardness values remain at ~25 GPa for both coating types. The friction coefficient decreases from 0.7 for undoped Al_2O_3 to 0.5 and 0.4 for the C-doped coating at room temperature and 700°C, respectively, which is attributed to the formation of a lubricious nanocrystalline graphite layer in the sliding contact. At 900°C, both coatings show a further reduction of the friction coefficient to 0.35 due to out-diffusion of titanium through the thermal crack network of the Al_2O_3 layer and formation of rutile.

1. Introduction

Hard coatings deposited by chemical vapor deposition (CVD) are frequently used, in order to increase the wear resistance of tools. Despite of their outstanding wear resistance, their friction behavior often seems to be improvable [1]. Introducing a lubricating phase is an approach which offers reduced friction compared to wear resistant hard coatings like (Al,Cr)N [2] or Al_2O_3 [3]. For cemented carbide cutting inserts, Al_2O_3 is often part of a CVD coating system, due to its chemical stability and hot hardness [4, 5]. In particular, the addition of CH_4 during deposition of Al_2O_3 is reported to reduce the grain size [6-8] and carbon incorporation is suggested [8, 9], but the tribological behavior of such coatings has not been investigated so far.

Consequently, the present work deals with the influence of C-doping on the tribological behavior of CVD Al_2O_3 coatings. While the general influence of C-doping on the structure of Al_2O_3 coatings has been reported only for laboratory-scale deposition experiments [6-9], in the present study an industrial-scale deposition plant is used. Thus, the already reported grain refinement, potentially related to improved mechanical properties, should be combined with the occurrence of solid-lubricating graphite-like phases as reported for other Al_2O_3 applications [10, 11], in order to improve cutting performance.

2. Experimental details

Al_2O_3 monolayer coatings were deposited by thermally activated low pressure CVD at a deposition pressure of 80 mbar. The temperature during Al_2O_3 deposition was set to 1005°C, utilizing an industrial-scale hot-wall CVD plant with radial gas distribution (Bernex BPX 530L). The precursor mixture is comparable to state-of-the-art recipes [12-14] and contains the gases $AlCl_3$, CO_2, HCl, H_2S, and H_2. For the C-doped coatings, a CH_4 flow-rate of 1 l/min and 2 l/min, respectively, was added (corresponding to 1.8 and 3.5 vol.% of the total gas flow) and balanced with a lower H_2 flow-rate, while all other flow rates were kept constant. The Al_2O_3 deposition time was kept constant at 3 hours. To improve adhesion and suppress coating/substrate interdiffusion, a TiN/TiCN base-layer was applied between the cemented carbide substrates (11 wt.% Co, 4 wt.% TiC, 8 wt.% TaC-NbC, 77 wt.% WC) and the Al_2O_3. In order to force the growth of the α-Al_2O_3 modification, a thin bonding layer [15-17] was deposited between base-layer and Al_2O_3. For tribological tests, disc-shaped cemented carbide substrates with a diameter of 30 mm and a thickness of 4 mm were used; all other investigations were performed on flat cemented carbide cutting inserts (ISO-1832: SNUN, 12.8 × 12.8 × 4.8 mm^3). Prior to deposition, all substrates were polished and cleaned with a standard procedure comparable to commercial production.

Concentration depth profiles were determined by glow discharge optical emission spectroscopy (GDOES) with a Jobin-Yvon Horiba JY10000RF equipment, using a pulsed RF generator. A plasma cleaning process was used in order to reduce the amount of contaminants adsorbed on the sample surface. The given chemical compositions were calculated by averaging these concentration values within the respective Al_2O_3 layers. To confirm these coating compositions, X-ray photoelectron spectroscopy (XPS) was performed, using an Omicron Multiprobe system (Al $K\alpha$ radiation). Spectra were obtained for the as-deposited state, after in-situ vacuum annealing at 350°C for 20 minutes and after Ar^+ ion sputtering at 2 keV for 20 minutes.

Additionally, time-of-flight secondary ion mass spectrometry (ToF-SIMS) measurements were performed, providing a qualitative comparison of the C-content with a higher resolution. An ION-TOF time-of-flight SIMS (TOF.SIMS^5) instrument with a 500 × 500 μm^2 field of view was used on cross-sections of undoped and C-doped coatings. Element mapping was carried out in the dual beam mode [18] using a high energy analysis beam (particles: Bi_1^+; acceleration energy: 25 keV; resolution: 256 × 256 pixel) and a low energy beam for material abrasion (particles: Cs^+; acceleration energy: 1 keV). First primary ions – from a liquid metal ion gun – were accelerated to the sample surface (in this case a cross-section of the coating), where they generate secondary ions, which were analyzed in a time-of-flight mass analyzer. During the analyze time, Cs^+ ions – which enhance the formation of negatively charged ions (like C^- or AlO^-) – ablated a 1000 × 1000 μm^2 area of the sample surface. Before the sample is analyzed again, an electron flood gun is used to compensate the charging of the sample surface. In order to increase the visible coating thickness on the cross-sections, the grinding and polishing of the cross-section was done with a grazing angle of 2°. The last polishing step was performed with a silica suspension (Struers, OP-U), as diamond polishing probably would interfere with the C-content measurement.

The crystallographic structure and phase formation were determined with glancing angle X-ray diffraction (GAXRD) using Cu $K\alpha$ radiation with an incident angle of 2°. The composition of the TiCN base-layer was calculated with stress correction, based on GAXRD measurements with an incident angle of 10°. The residual stresses were analyzed with the $\sin^2\psi$-method. All XRD measurements were conducted with a Panalytical X'Pert Pro diffractometer. Coating top-view morphology and fracture cross-section appearance were investigated with a scanning electron microscope (SEM, Zeiss EVO 50) equipped with an energy-dispersive X-ray analyzer (EDS, Oxford Instruments INCA).

Hardness and Young's modulus were assessed by nanoindentation on diamond-polished coating surfaces, using a UMIS system with a Berkovich indenter, and loads stepwise increased from 1 to 50 mN for each measurement. The tribological characterization was performed on CSM ball-on-disc tribometers at room temperature, 700°C and 900°C with a 6 mm diameter Al_2O_3 ball counterpart. Normal-load sliding-distance combinations of 10 N for 500 m and 5 N for 100 m were used for room temperature and high temperature tests, respectively. For all tests, a tangential sliding speed of 0.1 m/s and a wear track radius of 5 mm were selected. The wear tracks were characterized with light optical microscopy (LOM) and a Wyko NT1000 3D profiling system based on white light interferometry. Subsequently, all discs from room- and high temperature ball-on-disc tests were investigated with Raman spectroscopy, using a Jobin-Yvon LabRam confocal Raman spectrometer (Nd-YAG laser, wavelength: 532.2 nm, power: 10 mW). Several measurements were performed within and outside the wear track after a calibration procedure on silicon, polyethylene and calcite.

3. Results and discussion

The chemical composition of the undoped and C-doped Al_2O_3 layer, as characterized with GDOES, is listed in Table 1. Beside aluminum and oxygen, showing a stoichiometry close to the nominal Al_2O_3 value, also nitrogen (~5 at.%), titanium (~0.1 – 0.2 at.%) and carbon could be detected. The average C-content within the Al_2O_3 coating increases to 0.2 at.% only for an addition of 2 l/min CH_4, while the coating deposited with 1 l/min CH_4 shows a C-content of 0.1 at.% which is similar to the undoped coating. The GDOES concentration-depth-profiles show carbon enrichment for all coatings at the surface which is more pronounced for the C-doped coatings. The highest value is measured for the coating deposited with 2 l/min CH_4, which exhibits a C-concentration of ~0.7 at.% close to the surface. Apart from the initial surface contamination, the occurrence of thermal cracks could also contribute to the detection of elements which are forming the base-layer (titanium, carbon, nitrogen). As thermal cracks occurred for all coatings within this work, a simultaneous sputtering of base-layer atoms could influence the amount of titanium, carbon and nitrogen detected within the Al_2O_3 layer. The composition of the base-layer itself is relatively constant within the range of 15 – 17 at.% carbon and 35 – 33 at.% nitrogen, respectively (see Table 1), because its deposition conditions were unchanged. However, the origin of the rather high nitrogen content detected within the Al_2O_3 layer is not clear yet, but could in part also originate from the base-layer.

Table 1
Chemical composition of the Al_2O_3 coatings investigated (GDOES) and of the base-layer (GAXRD).

CH_4 [l min^{-1}]	at.% Al	at.% O	at.% N	at.% C	Al / O	base-layer
0	40.1	54.9	4.8	0.1	0.73	$TiC_{0.3}N_{0.7}$
1	42.0	52.5	5.2	0.1	0.80	$TiC_{0.33}N_{0.67}$
2	40.3	53.9	5.4	0.2	0.75	$TiC_{0.32}N_{0.68}$

A comparison of the GDOES data by applying more surface-sensitive XPS measurements has been performed for as-deposited coatings, after an 350°C in-situ heat treatment (20 minutes) and after 2 keV Ar-sputtering (20 minutes). For the C-doped sample (1 l/min CH_4), the amount of carbon is decreased from ~29 at.% (as-deposited) to ~20 at.% after the heat treatment. The undoped coating shows a decrease from ~11 at.% to ~8 at.%, respectively. Apparently, the addition of CH_4 during Al_2O_3 deposition also influences the amount of C-containing species at the surface of the Al_2O_3 layer. After the 2 keV Ar-sputtering, no carbon can be detected for the undoped coating while the C-content is comparable to the detection limit for both C-doped samples. For the latter, just a hint of a C-peak is visible, hence the corresponding amount of carbon could be roughly estimated to ~0.5 – 1.0 at.%. Nevertheless, this is in good agreement with the C-concentration values detected in the vicinity of the surface with GDOES.

Qualitative ToF-SIMS measurements show the difference between undoped and C-doped samples more clearly. The results displayed in Fig. 1 are based on measurements performed at an area of 500 × 500 µm^2 of the cross-section of the undoped and C-doped coating. For an easier comparison of the carbon signal, the two-dimensional field-of-view was summed up for each pixel row (parallel to the coating/substrate interface) and the resulting intensity is plotted in Fig. 1 along the coating cross section (from the base-layer, to the alumina coating and to the surface). As the C-content within the TiCN base-layer is rather similar for both coatings (see Table 1), it was used for normalization of the measurements. Within the C-doped alumina coating (1 l/min CH_4) a significantly higher content of carbon is detected compared to the undoped alumina coating (Fig. 1). The peaks of C-content detected within the C-doped alumina coating are rather attributed to a local influence of the base-layer than to local carbon enrichment. For example, local adhesion failure of the alumina coating occurring during ToF-SIMS measurement could consequence that base-layer species are detected within the alumina coating. Nevertheless, these additional peaks do not countermand the result that the C-doped coating shows a clearly higher level of C-content. Furthermore, the ToF-SIMS results obtained at the surface are in good agreement with the XPS results, as the C-content at the surface is relatively high for the C-doped Al_2O_3 coating (1 l/min CH_4) but clearly lower for the undoped coating.

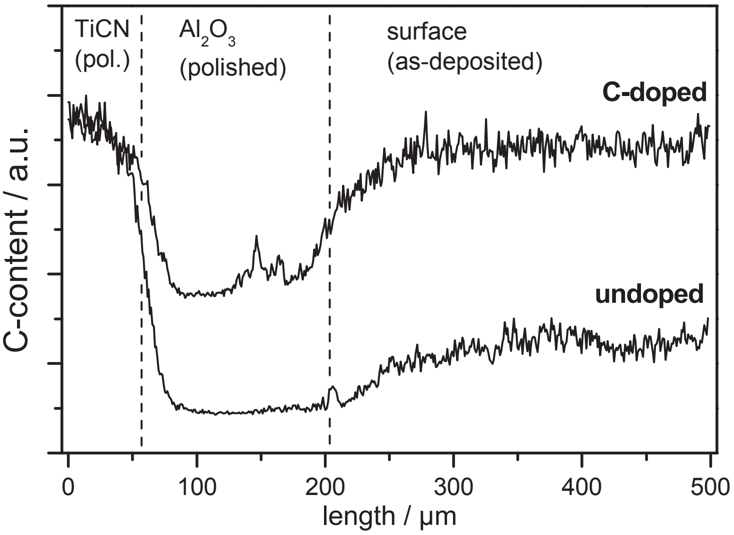

Fig. 1. Qualitative ToF-SIMS measurements on undoped and C-doped (1 l/min CH_4) alumina coatings, showing the C-content on the polished cross-section as well as on the unpolished surface.

Although only a small difference in chemical composition of the undoped and the C-doped layers could be detected, top-view SEM images (Fig. 2a,b) show less facetted and bigger grains for the C-doped Al_2O_3 coating compared to the undoped Al_2O_3. This is contrary to the reported grain refinement for carbon incorporation [7], which might be related to slightly changed growth conditions, where also the dopant amount could be too low for inhibiting grain growth. The undoped coating also shows some marbled grain faces and regions with many small facets, which are both not visible for the C-doped coatings. The fracture cross-section images (Fig. 2c,d) indicate a lower surface roughness for the undoped Al_2O_3 coating, probably related to its smaller grains. The coating thickness is comparable for undoped and C-doped coatings, which corresponds to an Al_2O_3 growth rate in the range of 1.3 $\mu m\ h^{-1}$, as the deposition time was kept constant at 180 minutes. The morphology is very similar for the C-doped coatings deposited with 1 l/min and 2 l/min CH_4, hence only the former is displayed in Fig. 2.

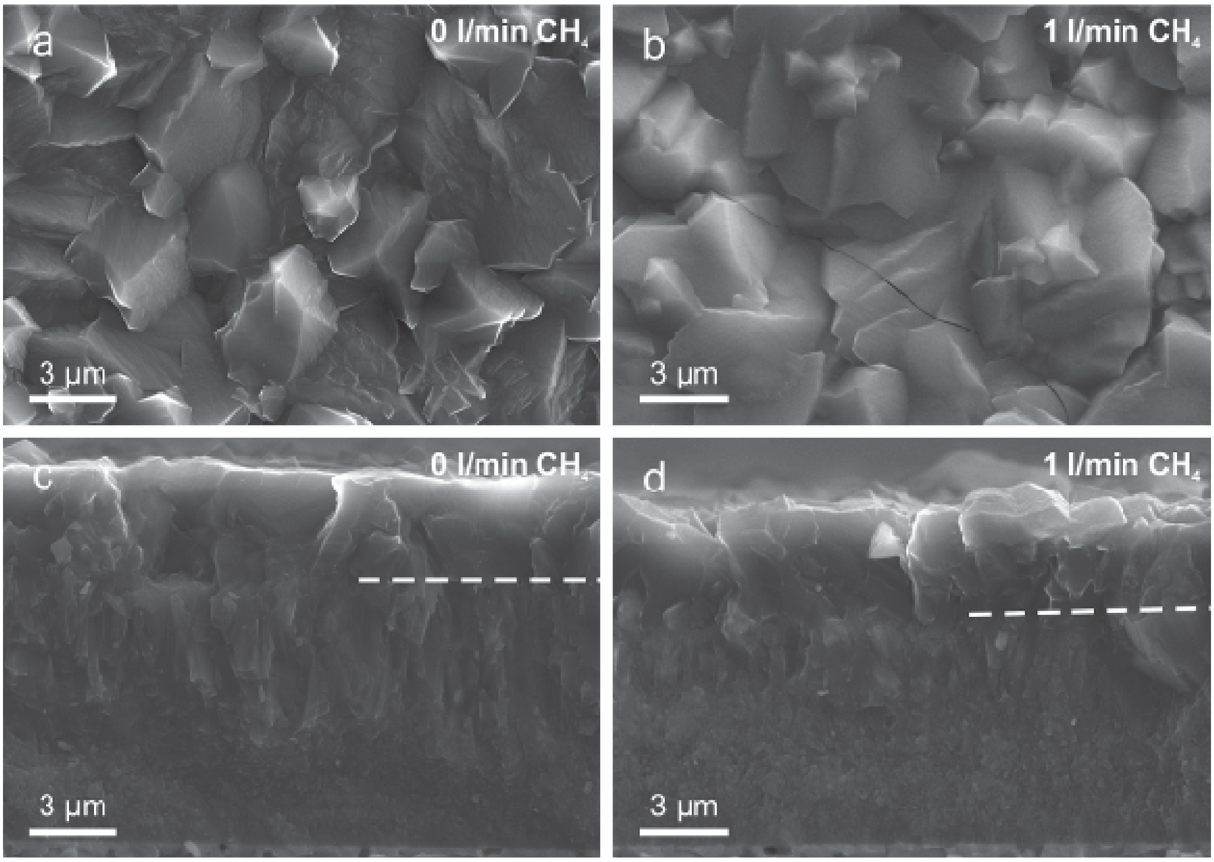

Fig. 2. SEM micrographs show the coating top-view morphology of undoped (a) and C-doped Al_2O_3 coatings (b). The fracture cross-section images show the Al_2O_3/TiCN interface (dashed white line) and the cemented carbide substrate (bottom edge) for undoped (c) and C-doped Al_2O_3 coatings (d).

For all coatings, GAXRD investigations show the α-Al_2O_3 modification with lattice parameters (Table 2) very close to the JCPDS standard (PDF 00-010-0173). Beside Al_2O_3, only TiCN from the base-layer and small amounts of TiO_2 could be detected with GAXRD. Most likely, the TiO_2 is located at the interface between Al_2O_3 and TiCN and part of the bonding layer [17]. No significant effect of C-doping on the preferred orientation of the α-Al_2O_3 phase could be detected. For the coating deposited with 1 l/min CH_4, the residual tensile stresses are slightly decreased to ~400 MPa, compared to ~570 MPa for the undoped coating, but the coating deposited with 2 l/min CH_4 again shows an increased residual stress of ~600 MPa. The thermal crack network, visible on polished sample surfaces, is comparable for all coatings. The coating hardness and the Young's modulus are in the range of 25 – 26 GPa and 370 – 390 GPa, respectively. Both values are not significantly affected by C-doping and comparable to literature [19, 20].

Table 2

Lattice parameters, residual stress, mechanical properties of the Al_2O_3 coatings investigated

CH_4 [l min^{-1}]	modification	a [Å]	c [Å]	σ_{res} [MPa]	H [GPa]	E [GPa]
0	α-Al_2O_3	4.758	12.991	570	25.7 ± 1,7	371 ± 33
1	α-Al_2O_3	4.757	12.988	400	24.9 ± 2.3	393 ± 26
2	α-Al_2O_3	4.755	12.983	600	26.1 ± 2.3	387 ± 23

As the tribological behavior of both C-doped coatings is comparable, only the data of the coating deposited with 1 l/min CH_4 is discussed below and in the following the term "C-doped" refers to this coating. Obviously, a very low and difficult to analyze C-content already influences the tribological behavior significantly and a further increase in C-content, say from <0.5 at.% to ~1 at.%, does not consequence an additional improvement. At room temperature, tribological investigations show a lower average steady-state friction coefficient (μ_{ss}) of ~0.5 for the C-doped Al_2O_3 coating, compared to ~0.7 for the undoped coating, while the scattering of the friction curve is not significantly affected (Fig. 3). LOM images reveal the occurrence of darker spots within the wear track of the C-doped coating (Fig. 4b,c), which are not visible within the wear track of the undoped Al_2O_3 coating (Fig. 4a). At a higher magnification, the LOM image reveals that these spots show an orientation perpendicular to the sliding direction (Fig. 4c), probably indicating a laminated structure and the occurrence of shear processes. Raman measurements show that these darker regions consist of Al_2O_3 [21] and nanocrystalline graphite [22, 23] as displayed in Fig. 4d (spectrum I), while in between these dark spots (Fig. 4d, spectrum II) and within the wear track of the undoped coating (similar to Fig. 4d, spectrum II), only Al_2O_3 can be detected. The reduction of the room temperature friction coefficient is attributed to the lubricating effect of graphite [24]. As these graphite containing areas are only partly covering the wear track, the friction coefficient is still higher compared to other graphite including systems reported in literature [25].

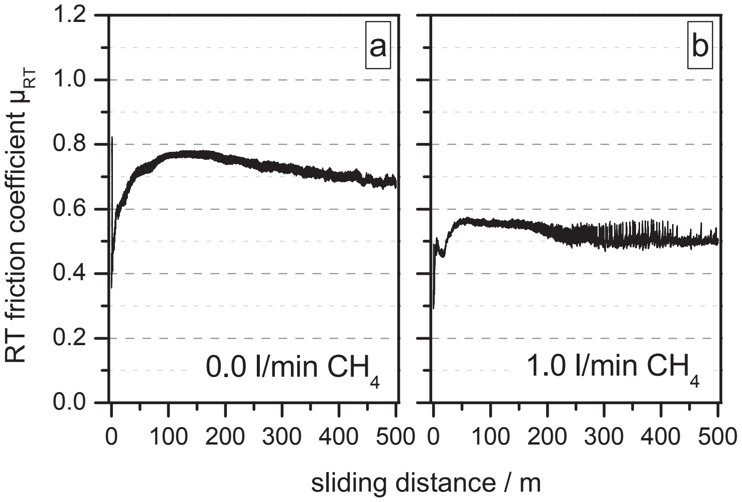

Fig. 3. Room temperature friction coefficients measured with ball-on-disc tests for undoped (a) and C-doped (b) Al_2O_3 coatings (Al_2O_3 counterpart, 10 N load, 0.1 m s^{-1} sliding speed).

At 700°C, the ball-on-disc tests show a comparatively higher difference between undoped and C-doped Al_2O_3 coatings, i.e. the average friction coefficient decreases from ~0.7 to ~0.4 for the undoped and C-doped coating, respectively (Fig. 5). The undoped coating also shows a considerably higher scattering of the friction curve, which is probably caused by the larger amount of wear debris (mainly ball material) within the broad, flat wear track. The wear track of the C-doped coating is at least five times narrower (see Fig. 6a,b) compared to the undoped coating and shows a completely different appearance. SEM images with higher magnification show a lot of smeared debris material within the wear track of the undoped coating (Fig. 6d), but only few debris for the C-doped coating (Fig. 6e). Moreover, for the C-doped coating there are relatively large regions which are almost unaffected by the sliding contact and the original coating morphology is still visible within the track (compare Fig. 6e to Figs. 6f and 2b). Consequently, at lower magnification, the wear track is difficult to identify on the SEM image (Fig. 6c). The wear track appearance suggests lower adhesion forces within the tribo-contact for the C-doped coating compared to the undoped coating. This could be the reason

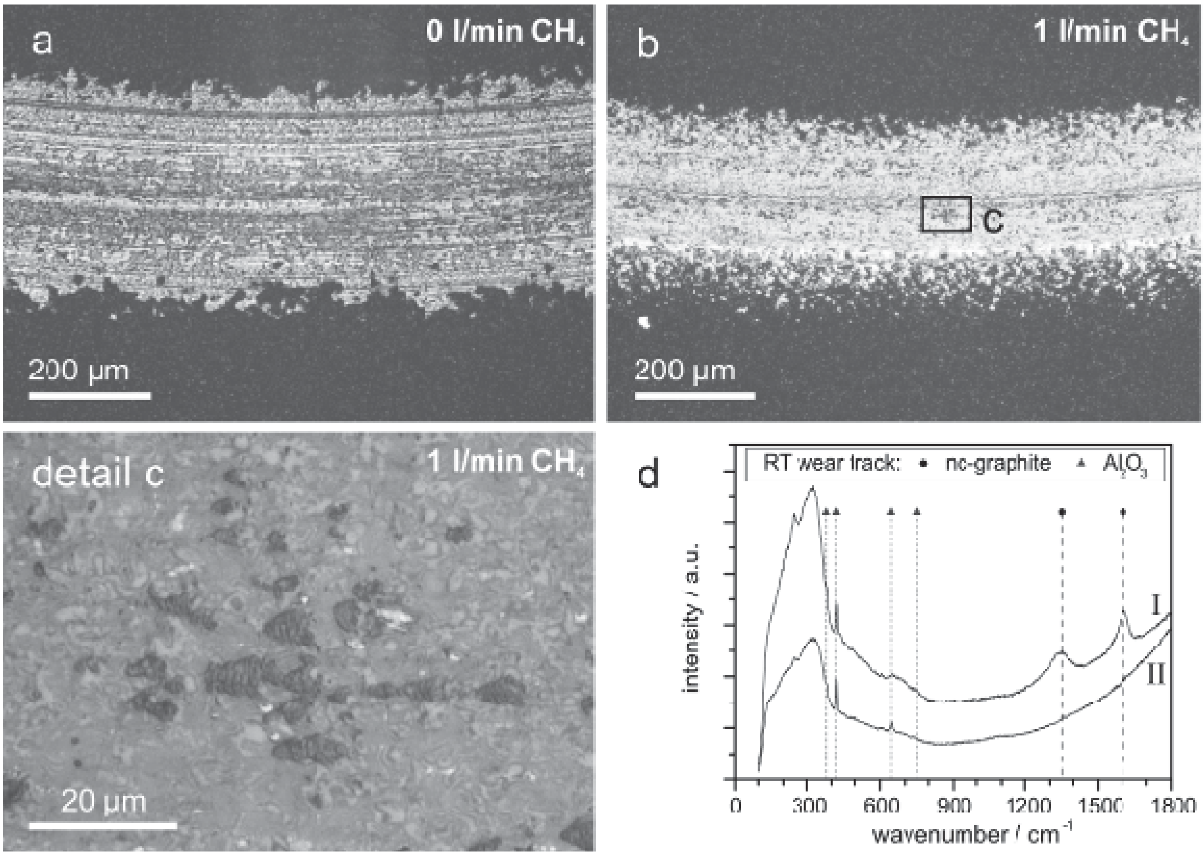

Fig. 4. Wear tracks of undoped (a) and C-doped (b, c) Al_2O_3 coatings after ball-on-disc tests at room temperature (LOM pictures). Raman measurements (d) performed at a dark region (spectrum I) and at a bright region (spectrum II) within the wear track of the C-doped coating, showing bands of Al_2O_3 and nanocrystalline graphite.

for lower ball wear and hence less wear debris formation, causing a smaller area of interaction, i.e. a narrower wear track (see Fig. 6a,b). The reason for the lower adhesion forces could be either a modification of the Al_2O_3 structure by C-doping and/or the effect of carbon on formation of tribological reaction layers in the sliding contact, where the undoped Al_2O_3 coating is rather similar to the ball material, which would favor adhesion [26]. However, extensive Raman measurements did not detect any species, except Al_2O_3, within or outside the wear tracks after the 700°C test and there are no signs for surface-segregation of base-layer elements. Although the oxidation of carbon starts at 600°C [27], the activity of Al_2O_3-incorporated carbon, which diffuses to the surface during testing, can not be excluded. Additionally, traces of surface-segregated carbon could – although being permanently formed in the sliding contact – probably completely vanish during the cooling period after the ball-on-disc test.

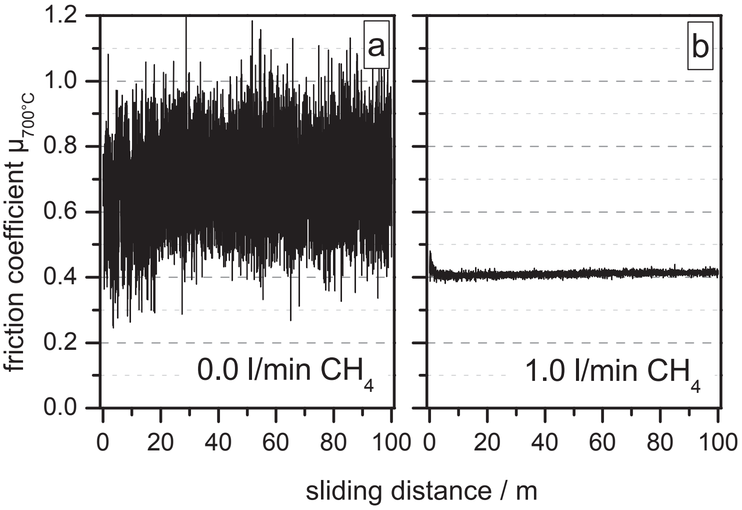

Fig. 5. Friction coefficients measured with ball-on-disc tests at 700°C for undoped (a) and C-doped (b) Al_2O_3 coatings (Al_2O_3 counterpart, 5 N load, 0.1 m s^{-1} sliding speed).

Increasing the ball-on-disc testing temperature to 900°C causes a still slightly lower friction coefficient for undoped (~0.36) and C-doped coatings (~0.37, see Fig. 7) and both coatings offer a good high temperature protection during the testing procedure with an overall duration of ~2 hours at 900°C. SEM images (Fig. 8a,b) show a narrow wear track with low amounts of wear debris for both the C-doped and undoped coating. The scattering of the friction curve and the amount of wear debris is slightly smaller for the C-doped coating. SEM images with higher magnification show almost unaffected regions within the wear track of both coatings (Fig. 8c,d), suggesting that the original coating surface is partly well separated from the counterpart ball. EDS elemental maps show an enrichment of Ti in the vicinity of the thermal cracks (Fig. 8e,f), which are visible within and outside the wear track for the undoped and the

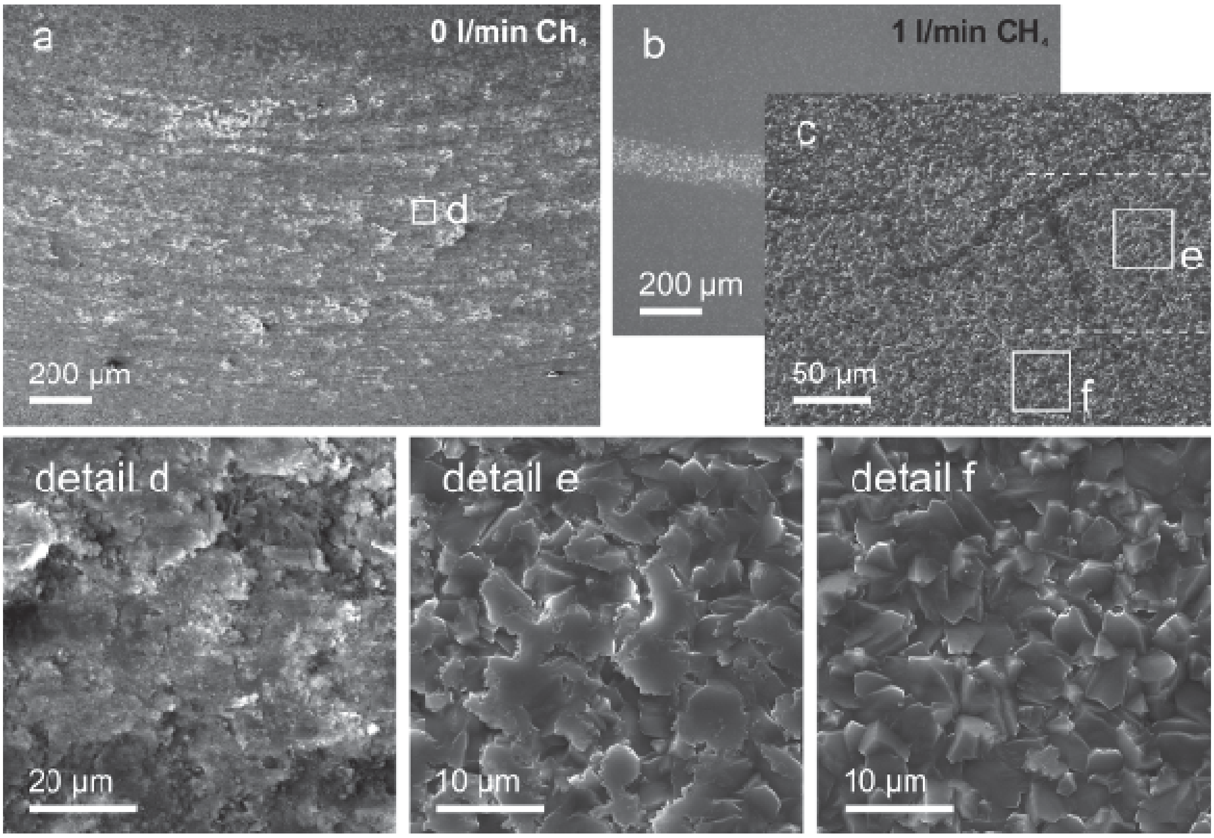

Fig. 6. Comparison of 700°C wear tracks for undoped (a, SEM) and C-doped Al_2O_3 coating (LOM: b, SEM: c). Wear track images with higher magnification are shown for undoped (d) and C-doped Al_2O_3 coatings (e). Detail (f) shows an area outside the wear track of the C-doped coating.

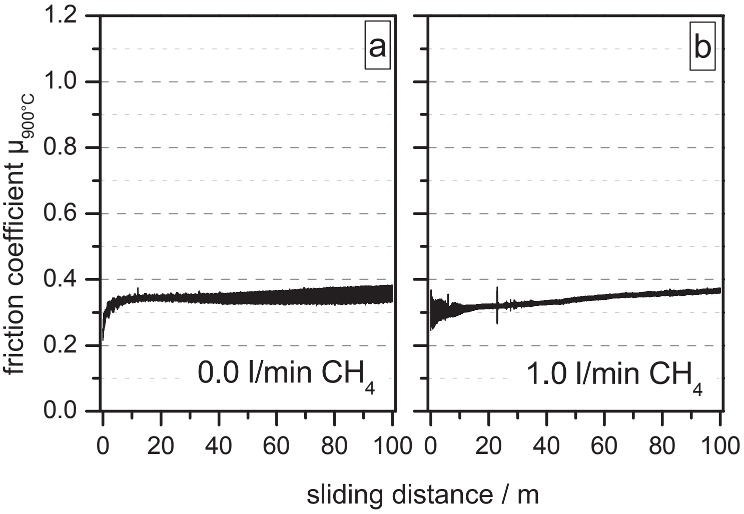

Fig. 7. Friction coefficients measured with ball-on-disc tests at 900°C for undoped (a) and C-doped (b) Al_2O_3 coatings (Al_2O_3 counterpart, 5 N load, 0.1 m s^{-1} sliding speed).

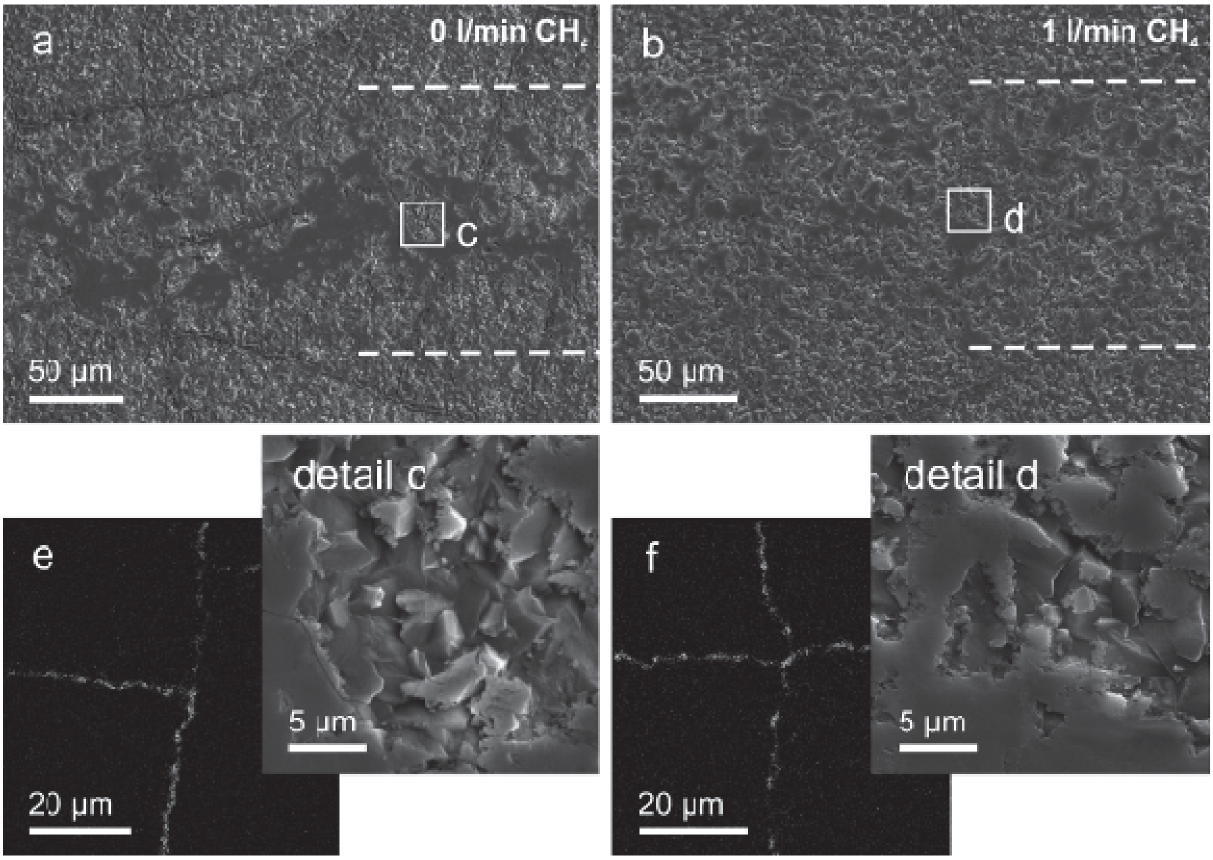

Fig. 8. SEM images of wear tracks for undoped (a,c) and C-doped Al_2O_3 coatings (b,d) after a ball-on-disc test at 900°C. Elemental EDS-maps, showing the Ti-signal within the wear tracks, are also shown for undoped (e) and C-doped Al_2O_3 coatings (f).

C-doped coating. Despite the apparently more pronounced segregation occurring at the thermal cracks (cf. Fig. 8a and Fig. 8b) of the undoped coating, the amount of detected Ti at the crack network is similar for the undoped and the C-doped coating. Raman investigations within the 900°C wear tracks revealed the occurrence of Al_2O_3 [21] and rutile [28] for both coatings (Fig. 9). Only Al_2O_3 containing regions (Fig. 9, spectrum I), rutile dominated spectra showing only tiny shoulders at the Al_2O_3 peak positions (Fig. 9, spectrum II, III) and spectra with similar amounts of Al_2O_3 and rutile can be found within undoped and C-doped wear tracks. The occurrence of graphite is attributed to diffusion of base-layer atoms to the surface, which is corroborated by two facts: *(i)* carbon bands occur only in connection with rutile and *(ii)* also the undoped coating shows graphite bands. Furthermore, the formation of rutile consumes titanium from the base-layer and makes some carbon redundant, which could diffuse to the surface. A comparable behavior has been reported for Al_2O_3-TiC bulk material [29], where also titanium oxidation and carbon diffusion occur. The relatively big amount of carbon, which is available as the TiCN base-layer contains a major fraction of carbon, could explain the detection of graphite bands, despite the increased temperature which should lead to faster oxidation and volatilization of carbon at the surface. Compared to the room temperature wear tracks, the graphite bands are much weaker at 900°C and the rutile bands are dominating. Hence, for both coatings, the observed reduction of the friction coefficient seems to be mainly caused by Ti which diffuses from the TiCN base-layer through the thermal crack network of the Al_2O_3 coating and forms rutile on the surface (Fig. 9). The friction reduction capabilities of rutile are already documented in literature [30, 31]. The slightly lower friction coefficient, compared to similar systems [3], is attributed to the higher testing temperature, which could favor lower shear forces in the rutile.

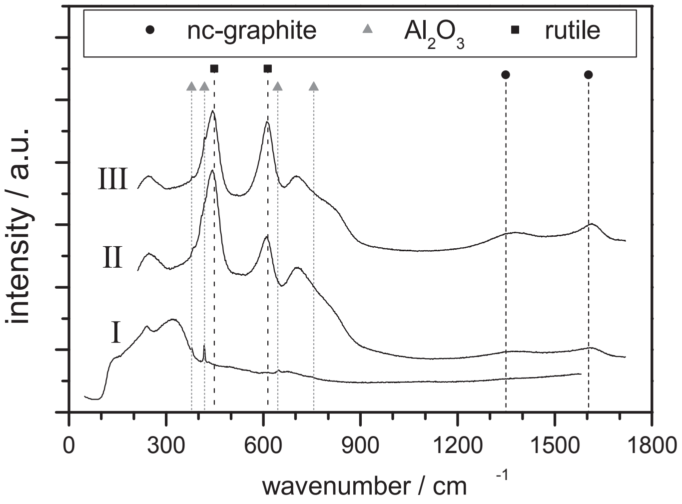

Fig. 9. Raman measurements after the 900°C ball-on-disc test within the wear tracks of the undoped Al_2O_3 coating (spectrum I, II) and the C-doped Al_2O_3 coating (spectrum III), showing bands of Al_2O_3, rutile and nanocrystalline graphite.

4. Conclusions

For the investigated CVD Al_2O_3 coating system, the addition of CH_4 to the precursor gas mixture causes incorporation of small amounts (i.e. ≤ 1 at.%) of carbon within the Al_2O_3 layer, but changes the coatings morphology and significantly improves the tribological behavior without deteriorating the mechanical properties. Surface segregation of carbon – more pronounced for the C-doped alumina coatings – suggest that carbon incorporation into alumina is less favorable at the deposition conditions applied within this study. However, the friction coefficient of undoped Al_2O_3 (~0.7) is lowered by C-doping to ~0.5 and ~0.4 at room temperature and 700°C, respectively. At 900°C testing temperature, titanium diffusion from the base-layer and the formation of rutile determines the tribological behavior of undoped and C-doped Al_2O_3, resulting in a still relatively low friction coefficient (~0.35). The diffusion of base-layer elements mainly occurs through the thermal crack network and seems to be less pronounced for the C-doped coating. Nevertheless, both, undoped and C-doped Al_2O_3 coatings, offer good high temperature protection against thermal loads like the two hours of tribological testing at 900°C. In order to further illuminate the influence of carbon incorporation in Al_2O_3 (e.g. grain refinement), higher C-contents, i.e. further adaptations of the deposition process would be necessary. However, also the low C-contents investigated within this study have proven to influence the tribological behavior of Al_2O_3 coatings beneficially.

Acknowledgement

Financial support by the Austrian Federal Government and the Styrian Provincial Government, within the research activities of the K2 Competence Center in the framework of the Austrian COMET Competence Center Programme, is gratefully acknowledged. The authors are grateful to DI A. Fian from Joanneum Research in Weiz for the support regarding the XPS analysis and to G. Hawranek for the SEM investigations.

References

[1] H.E. Hintermann, Wear 100/1-3 (1984) 381.

[2] R. Franz, J. Neidhardt, R. Kaindl, B. Sartory, R. Tessadri, M. Lechthaler, R. Polcik, C. Mitterer, Surf. Coat. Technol. 203/8 (2009) 1101.

[3] D. Hochauer, C. Mitterer, M. Penoy, C. Michotte, H.P. Martinz, M. Kathrein, Surf. Coat. Technol. 203/3-4 (2008) 350.

[4] P.K. Mehrotra, D.T. Quinto, High Temp.-High Press. 18 (1986) 199.

[5] S. Ruppi, J. Phys. IV 11/3 (2001) 847.

[6] H. Altena, G. Pauer, P. Wilhartitz, B. Lux, in: J.O. Carlsson, J. Lindström (Eds.), 5th EuroCVD, Uppsala, Sweden, 1985, p. 334.

[7] M. Danzinger, J. Peng, R. Haubner, B. Lux, J. Phys. II 1/C2 (1991) 571.

[8] A. Kwatera, Thin Solid Films 200/1 (1991) 19.

[9] P. Wilhartitz, M. Grasserbauer, H. Altena, B. Lux, Surf. Interface Anal. 8/4 (1986) 159.

[10] A.G. Khurshudov, M. Olsson, K. Kato, Wear 205/1-2 (1997) 101.

[11] J. Tian, Q.Z. Wang, Q.J. Xue, Nucl. Instrum. Meth. B 143/4 (1998) 488.

[12] C. Colombier, J. Peng, H. Altena, B. Lux, Int. J. Refract. Hard Met. 5/2 (1986) 82.

[13] M. Halvarsson, S. Vuorinen, Int. J. Refract. Met. Hard Mat. 15/1-3 (1997) 169.

[14] S. Ruppi, Int. J. Refract. Met. Hard Mat. 23/4-6 (2005) 306.

[15] M. Halvarsson, H. Nordén, S. Vuorinen, Surf. Coat. Technol. 68-69 (1994) 266.

[16] M. Halvarsson, S. Vuorinen, Surf. Coat. Technol. 76-77/1 (1995) 287.

[17] Z.-J. Liu, Z.-K. Liu, C. McNerny, P. Mehrotra, A. Inspektor, Surf. Coat. Technol. 198/1-3 (2005) 161.

[18] E. Niehuis, T. Grehl, in: A. Benninghoven (Ed.), 12th Int. Conf. Second. Ion Mass Spectrom., Brussels, 2000, p. 49.

[19] H. Chien, M.C. Gao, H.M. Miller, G.S. Rohrer, Z. Ban, P. Prichard, Y. Liu, Int. J. Refract. Met. Hard Mat. 27/2 (2009) 458.

[20] S. Ruppi, A. Larsson, A. Flink, Thin Solid Films 516/18 (2008) 5959.

[21] S.P.S. Porto, R.S. Krishnan, J. Chem. Phys. 47/3 (1967) 1009.

[22] I. Pócsik, M. Hundhausen, M. Koós, L. Ley, J. Non-Cryst. Solids 227-230/2 (1998) 1083.

[23] J. Robertson, J. Non-Cryst. Solids 299-302/2 (2002) 798.

[24] G.W. Stachowiak, A.W. Barchelor, Engineering Tribology, Butterworth-Heinemann, Oxford, 2001.

[25] G. Gassner, P.H. Mayrhofer, J. Patscheider, C. Mitterer, Thin Solid Films 515/13 (2007) 5411.

[26] E. Rabinowicz, Friction and wear of materials, John Wiley & Sons, Inc., New York, 1995.

[27] Y.H. Koh, O.S. Kwon, S.H. Hong, H.E. Kim, S.K. Lee, J. European Ceram. Soc. 21/13 (2001) 2407.

[28] S.P.S. Porto, P.A. Fleury, T.C. Damen, Phys. Rev. 154/2 (1967) 522.

[29] L.H. Zhang, R.V. Koka, Mater. Chem. Phys. 57/1 (1998) 23.

[30] M.N. Gardos, H.S. Hong, W.O. Winer, Tribol. Trans. 33/2 (1990) 209.

[31] M. Woydt, A. Skopp, I. Dörfel, K. Witke, Wear 218/1 (1998) 84.

Publication IV

Surface and Coatings Technology (2010), in submission

Thermal stability of doped CVD κ-Al_2O_3 coatings

D. Hochauer[a], C. Mitterer[b], M. Penoy[c], C. Michotte[c], H.P. Martinz[d,†], M. Kathrein[e]

[a] *Materials Center Leoben Forschung GmbH, Roseggerstrasse 12, A-8700 Leoben, Austria*
[b] *Department of Physical Metallurgy and Materials Testing, Montanuniversität Leoben, Franz-Josef-Strasse 18, A-8700 Leoben, Austria*
[c] *CERATIZIT Luxembourg SARL, L-8201 Mamer, Luxembourg*
[d] *PLANSEE SE, A-6600 Reutte, Austria*
[e] *CERATIZIT Austria GmbH, A-6600 Reutte, Austria*

[†] The authors regret to note that their co-author Hans-Peter Martinz suddenly passed away during preparation of this manuscript. He not only contributed significantly to this study with chemical fundamentals on the growth and formation of alumina phases, his ever friendly way brought joy and inventiveness to his colleagues.

Abstract

The application of wear resistant alumina-containing coating systems is a common approach to improve cutting performance of cemented carbide cutting inserts. This work focuses on the influence of B- and Ti-B-doping on the thermal stability of κ-Al_2O_3 deposited at high temperature and low pressure by chemical vapor deposition. The investigated coating architecture includes a κ-Al_2O_3 bilayer, separated by a TiN/TiCN interlayer, and a TiCN base-layer grown on cemented carbide substrates. The transformation from κ-Al_2O_3 to α-Al_2O_3 was examined with high temperature X-ray diffraction at 1030 and 1000°C as well as glancing angle X-ray diffraction after different heat treatment times at 1000°C. Chemical composition and coating morphology were determined with glow discharge optical emission spectrometry and scanning electron microscopy, respectively. In general, doping retarded the κ-α-transformation. Ti-B- and, to a lower degree, B-doping entailed a slower diffusion of base-layer and substrate species through the κ-Al_2O_3 bilayer, thus retarding the formation of segregated species on the sample surface. In addition, the heat treatment atmosphere decisively affected the κ-α-transformation.

1. Introduction

The unique combination of properties and the possibilities of designing them, e.g. by varying the crystal modification or the synthesis method, make alumina a widely used material for coatings [1] as well as for bulk material [2]. For cutting applications, it is probably the most successful material used as hard, wear- and oxidation-resistant coating [3]. It advantageously offers high hardness, chemical stability and low thermal conductivity, also at elevated temperatures [4, 5]. The major deposition method for these coatings is thermally activated chemical vapor deposition (CVD), where temperatures in the range of 800 to 1100°C are necessary [6, 7]. While numerous polymorphs of Al_2O_3 are known, only the metastable κ-, γ- and θ-Al_2O_3 as well as the thermodynamic stable α-Al_2O_3 have been investigated for cutting applications [8-11]. Mainly α- and κ-Al_2O_3, both anhydrous [12], are utilized in order to increase the performance of cemented carbide cutting tools [8, 10, 13-17]. Compared to the stable α-Al_2O_3, the κ-modification possesses morphological advantages, e.g. less pores, finer grain size [8, 10, 17, 18] and lower thermal conductivity [4]. However, the transformation from κ-Al_2O_3 to α-Al_2O_3 must be avoided, due to the accompanying volume contraction [19, 20], which deteriorates coating performance. Nevertheless, for κ-Al_2O_3 coatings grown without sophisticated process control, the transformation occasionally occurred during the deposition process, where the main influencing parameters are deposition temperature, deposition time and contamination of the precursor gas mixture [21]. Further effects may be caused by the presence of impurities [22, 23], multilayer periodicity [24] and the constitution of the layer deposited prior to κ-Al_2O_3 [9, 17]. Also mechanical activation and the stresses induced during cutting [25, 26] influence the transformations of the metastable Al_2O_3 phases. Improved control of the nucleation of Al_2O_3 growth allowed the deposition of the single-phase α- or κ-polymorphs [11]. During heat treatment of such single-phase κ-Al_2O_3 layers, the κ-α-transformation typically starts at thermal cracks [27] and high-temperatures as well as the presence of free surfaces seems to be a precondition for transformation [24, 28, 29]. Due to the volume contraction, transformed α-Al_2O_3 regions show secondary cracks, which form a continuous network for fully transformed coatings [27, 30, 31]. Except crack formation, there are no changes in surface morphology visible, which is related to the absence of large-scale atom rearrangement during transformation [19, 27]. Furthermore, the close-packed anion lattice planes seem to be preserved but rotated [29]. While the κ-α-transformation for undoped Al_2O_3 is investigated in detail, the influence of doping elements is often examined only for bulk Al_2O_3 [32-35] or it is a matter of unintentionally present impurities within CVD Al_2O_3 coatings [21-23]. Little work is accessible concerning the influence of doping elements, intentionally incorporated in CVD Al_2O_3 coatings [36, 37]. Consequently, this work focuses on the influence of B-doping and Ti-B-doping on the thermal stability of κ-Al_2O_3.

2. Experimental details

κ-Al_2O_3 bilayer coatings, separated by a thin TiN/TiCN interlayer, were deposited by thermally activated low pressure CVD at a deposition pressure of 80 mbar. The deposition time was kept constant at 65 minutes for each κ-Al_2O_3 layer. During κ-Al_2O_3 deposition, the temperature was set to 1000°C, utilizing an industrial-scale hot-wall CVD plant (Bernex BPX 530L) and the main precursor gases were $AlCl_3$, (~2 vol.%) and CO_2 (~4 vol.%) with H_2 carrier gas. Additionally, HCl and small amounts of H_2S were part of the precursor gas mixture. B-doping was realized with a BCl_3 flow rate of 150 ml min^{-1} (~0.3 vol. %). In the case of B-doped or Ti-B-doped κ-Al_2O_3 also the interlayer was B-doped. Ti-doped κ-Al_2O_3 coatings were deposited with a $TiCl_4$ flow rate of 0.2 ml min^{-1} (~0.1 vol.%). Both, BCl_3- and $TiCl_4$-addition were not balanced with a lower H_2 flow rate due to their comparable low amount. To improve adhesion and suppress coating/substrate interdiffusion, a TiN/TiCN base-layer was applied between the cemented carbide substrates and the κ-Al_2O_3 bilayer. For high-temperature X-ray diffraction (HTXRD), disc-shaped cemented carbide substrates (6 wt.% Co, 1 wt.% TiC, 5 wt.% TaC-NbC, 88 wt.% WC, grinded surface) with a diameter of 12 mm and a thickness of 2 mm were used. All other investigations were performed on polished cutting inserts (ISO-1832: SNUN, 12.8 × 12.8 × 4.8 mm^3) with a cemented carbide grade containing 11 wt.% Co, 4 wt.% TiC, 8 wt.% TaC-NbC and 77 wt.% WC. Prior to deposition, all substrates were cleaned with a standard procedure comparable to commercial production.

The coating top-view morphology and fracture cross-section appearance and the chemical composition of selected sample areas were investigated with a scanning electron microscope (SEM, Zeiss EVO 50) equipped with an energy-dispersive X-ray analyzer (EDS, Oxford Instruments INCA). Concentration depth profiles were determined by glow discharge optical emission spectroscopy (GDOES) with a Jobin-Yvon Horiba JY10000RF equipment, using a pulsed RF generator. A plasma cleaning process was used in order to reduce the amount of contaminants adsorbed on the sample surface. The crystallographic structure of as-deposited coatings were determined with glancing angle X-ray diffraction (GAXRD) using an angle of incidence of 2°. The residual stresses in the Al_2O_3 layer were analyzed with the $\sin^2\psi$-method. Isothermal high-temperature XRD (HTXRD) measurements were performed at 1000°C and 1030°C, with a N_2 flushed high-temperature oven-chamber (HTK 1200, Anton Paar). This heat treatment was done for 1000 minutes and the evolution of phase composition was observed with intermediate θ-2θ-scans. The amount of κ-Al_2O_3 (JCPDF # 00-052-0803) and α-Al_2O_3 (JCPDF # 00-010-0173) was measured with the peak sum intensity of the seven strongest peaks for each phase for $20° \leq 2\theta \leq 70°$. Both, GAXRD measurements and HTXRD measurements were conducted with a Panalytical X'Pert Pro diffractometer (Cu *Kα* radiation). At 1000°C, the thermal stability of the κ-Al_2O_3 bilayers was also examined with a heat treatment furnace (Carbolite RHF1600, Ar-flushed) and with a vacuum furnace (HTM-Reetz, pressure: ~10^{-6} mbar). There, the phase evolution was investigated with GAXRD, utilizing a Bruker D8 Advance diffractometer and an angle of incidence of 2°.

3. Results and discussion

The coating morphology of undoped, B-doped and Ti-B-doped κ-Al_2O_3 bilayer coatings is displayed in Fig. 1. The top-view micrographs do not show significant differences and the slightly more distinct surface relief for doped coatings does not correlate with increased roughness seen in the fracture cross-sections. The cross-sections shows the structure of the coating systems, comprising a TiCN base-layer (5-6 μm thick), two κ-Al_2O_3 layers (0.9-1.3 μm each) and a TiN/TiCN interlayer (0.2-0.3 μm) in between. In Fig. 1, both the interfaces of the interlayer and the interface between the base-layer and the inner κ-Al_2O_3 layer are highlighted with white dashed lines. Correlating to an increasing κ-Al_2O_3 coating thickness, visible at the cross-sections, the growth rate is increasing from 0.8 μm h^{-1} to 1.0 μm h^{-1} and 1.2 μm h^{-1} for undoped, B-doped and Ti-B-doped κ-Al_2O_3, respectively.

The doping influence on chemical composition is shown by the GDOES concentration depth-profiles for aluminum, oxygen, titanium and boron (Fig. 2). For undoped and doped κ-Al_2O_3, the aluminum and oxygen content is comparable and, within the outer κ-Al_2O_3 layer, the measured Al_2O_3 stoichiometry is close to the nominal value. Despite the comparable coating thickness of both κ-Al_2O_3 layers (see Fig. 1), the inner κ-Al_2O_3 layer seems to be significantly

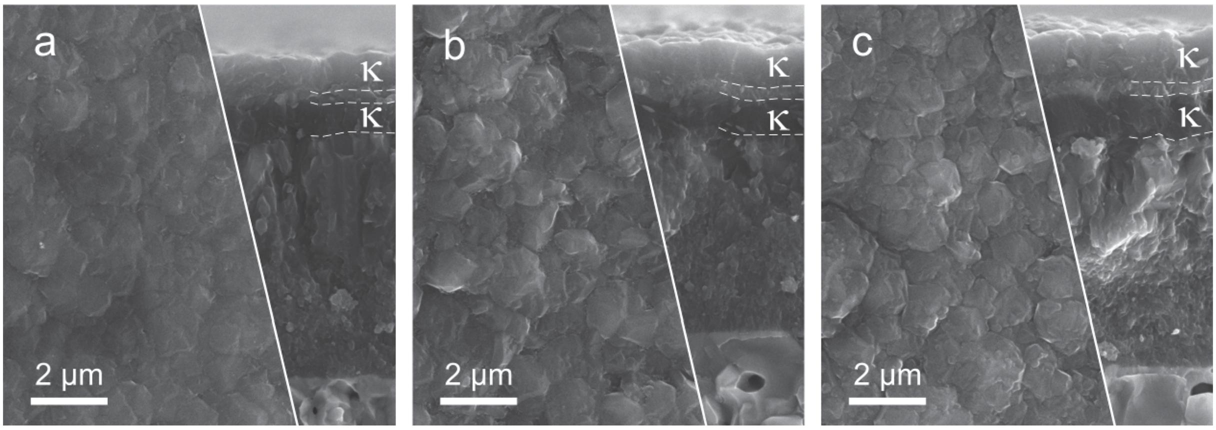

Fig. 1. SEM images of undoped (a), B-doped (b) and Ti-B-doped κ-Al_2O_3 bilayer coatings (c), showing top-view (left) and fracture cross-section images (right). Each of the two κ-Al_2O_3 layers is labeled and their interfaces are indicated by white dashed lines.

thinner and shows a slightly lower oxygen content, which could be related to the decreasing depth resolution of the GDOES measurement with increasing measurement time (i.e. increasing crater depth) [38, 39]. The undoped coating shows a boron content ~5 ppm within the κ-Al_2O_3 layers which is slightly increased in the interlayer (~30 ppm). For coatings deposited with a BCl_3-containing precursor gas mixture, the boron content within the κ-Al_2O_3 layers increases to 50 – 65 ppm and 70 – 100 ppm for B-doped and Ti-B-doped coatings, respectively. Simultaneously, the boron content within the interlayer is increased to a peak value close to 0.2 at.%. With $TiCl_4$ addition, the titanium content within the outer κ-Al_2O_3 layer increases to 0.5 at.% compared to 0.2 at.% for undoped and B-doped κ-Al_2O_3 (excluding the increasing Ti-concentration at the surface and at the κ-Al_2O_3/interlayer interface seen in Fig. 2). Assuming that this increasing titanium content (~0.3 at.%) is incorporated in the alumina lattice indicates a higher solubility limit of κ-Al_2O_3 for titanium compared to the significantly lower values reported for α-Al_2O_3 [40, 41]. Also previous investigations [42] showed that the incorporation of dopants within CVD α-Al_2O_3 is difficult at 1000°C deposition temperature. However, one should also keep in mind that the CVD deposition process, although conducted at relatively high temperatures, probably does not reach thermodynamic equilibrium, which might also contribute to an increased solubility of dopants. Comparing the outer and the inner κ-Al_2O_3 layer in Fig. 2 shows higher boron and titanium contents for the latter. This could be related to the fact that this layer is bordered by Ti- and B-containing coatings at both interfaces. Additionally, the deposition of the interlayer and the outer κ-Al_2O_3 layer, which acts as a 1000°C heat treatment for the inner κ-Al_2O_3 layer, could cause a more pronounced diffusion of titanium and boron into the inner κ-Al_2O_3 layer compared to the outer one. Moreover, the decreasing depth resolution of the GDOES with increasing measurement time reduces the sharpness of the interfaces visible in the concentration depth profiles, which could also contribute to an apparently increased titanium and boron content. Undoped and Ti-B-doped concentration profiles also show a segregation of titanium and boron at the surface, which is not visible for the B-doped coating.

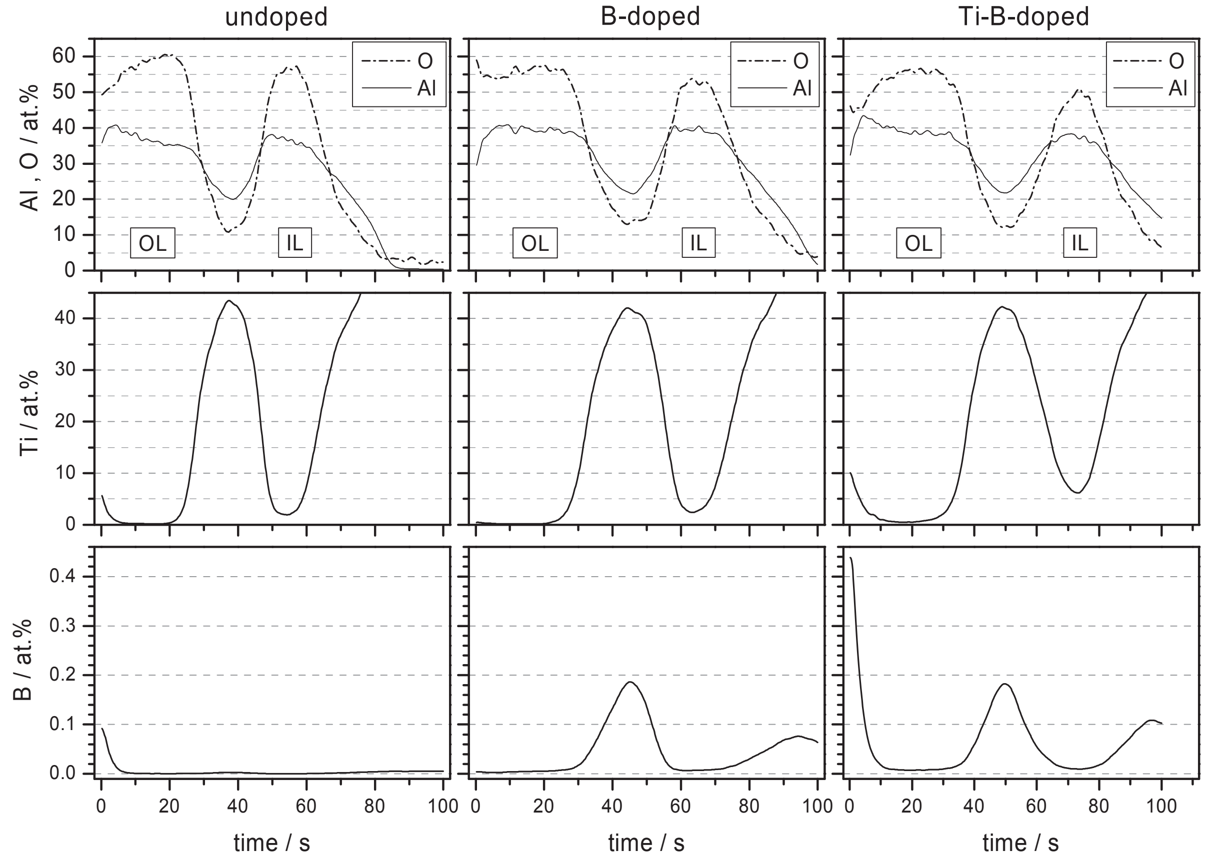

Fig. 2. Chemical composition of undoped (left column), B-doped (middle column) and Ti-B-doped (right column) κ-Al_2O_3 bilayer coatings, displayed by the GDOES concentration depth profiles of aluminum and oxygen (upper row), titanium (middle row) and boron (lower row). Outer κ-Al_2O_3 layer (at the surface) and inner κ-Al_2O_3 layer are labeled with “OL” and “IL”, respectively. The boron concentration is plotted with a larger scale of the ordinate.

For all as-deposited coatings, regardless of incorporated dopants, GAXRD measurements show two phases which are κ-Al_2O_3 and TiCN. As the GAXRD pattern is very similar for all as-deposited coatings, i.e. there are no peak shifts or changes in texture visible, only the pattern of the Ti-B-doped coating is shown in Fig. 3. The lattice parameters a (4.834±0.002 Å), b (8.304±0.003 Å) and c (8.934±0.003 Å) of the κ-Al_2O_3 phase are very close to standard values (JCPDF # 00-052-0803). With regard to the same powder standard, all κ-Al_2O_3 bilayers show more pronounced peaks for the (013), the (004) and the (015) orientation, which are all rather close to (001), being the dominant growth orientation of κ-Al_2O_3 [17]. This is in good agreement with the preferred growth orientation of CVD κ-Al_2O_3 layers reported in literature [43, 44]. The residual tensile stresses are increasing from ~240 MPa to ~290 MPa and ~390 MPa, for undoped, B-doped and Ti-B-doped κ-Al_2O_3 bilayers, respectively. The increasing residual stress could be partly related to the increasing coating thickness of the κ-Al_2O_3 bilayers as doping elements are introduced. On the other hand, it has to be mentioned that the minor variations of the base-layer thickness seen in Fig. 1, which could also influence the average residual stress in the κ-Al_2O_3 bilayers, do not seem to affect this tendency.

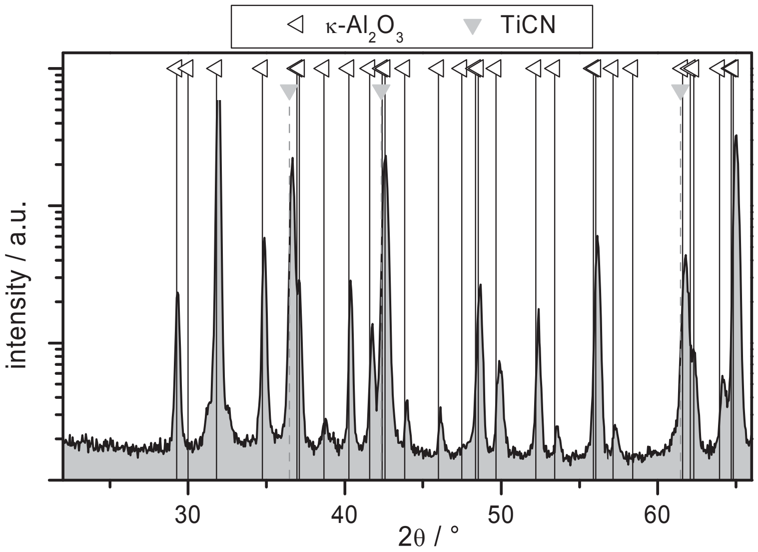

Fig. 3. GAXRD pattern of the Ti-B-doped κ-Al_2O_3 bilayer coating as deposited, including a detailed peak identification of κ-Al_2O_3.

The HTXRD investigations revealed a retarded κ-α-transformation for doped κ-Al_2O_3 compared to the undoped κ-Al_2O_3, i.e. the start times (Fig. 4a, solid lines) and finish times (Fig. 4a, dashed lines) are shifted to longer times at both annealing temperatures of 1000 and 1030°C. Furthermore, Ti-B-doped κ-Al_2O_3 transforms slower compared to the only B-doped κ-Al_2O_3. Applying the 95%-κ-Al_2O_3 criterion (determined from the intensity of the seven strongest κ-Al_2O_3 XRD peaks, see experimental details) for the onset of α-Al_2O_3 formation, the B-doped and the Ti-B-doped coatings show at 1030°C start times for the κ-α-transformation of ~13 and ~20 minutes, respectively, while the undoped coating fulfills this criterion already after 2 minutes. Moreover, traces of α-Al_2O_3 are already detected for the undoped coating after the heating step from room temperature to 1030°C in the HTXRD oven. At 1000°C, the onset of the κ-α-transformation is delayed to ~20, ~50 and ~60 minutes for undoped, B-doped and Ti-B-doped coatings, respectively. This sequence of undoped, B-doped and Ti-B-doped coatings is similar for starting and finishing of the κ-α-transformation at both annealing temperatures, i.e. 1030 and 1000°C. Compared to the undoped coating, Ti-B-doping delays the finish times for 85 and 110 minutes at 1030 and 1000°C, respectively. Subsequently to the κ-α-transformation, the formation of TiO_2 is detected, which is attributed to a small residual oxygen partial pressure within the high temperature chamber of the HTXRD system. It is striking, that the time gap between the finishing of the κ-α-transformation and the TiO_2 formation is rather constant for both testing temperatures (undoped: 40 min., B-doped: ~100 min., Ti-B-doped: ~200 min.), which suggests a less pronounced temperature dependence of the TiO_2 formation process compared to the κ-α-transformation. Obviously, the formation of a secondary crack network during κ-α-transformation increases the possibilities for oxidation of the TiCN base-layer, which explains the onset of TiO_2 formation soon after finishing of the κ-α-transformation. Moreover, the doped coatings show an increased delay of the TiO_2 formation (see Fig. 4b), which seems to originate from less pronounced diffusion of titanium and/or oxygen through the Al_2O_3 layer. This might be due to the doping elements which cause a less distinct secondary crack network [45] or that they are blocking diffusion paths within the Al_2O_3 layer.

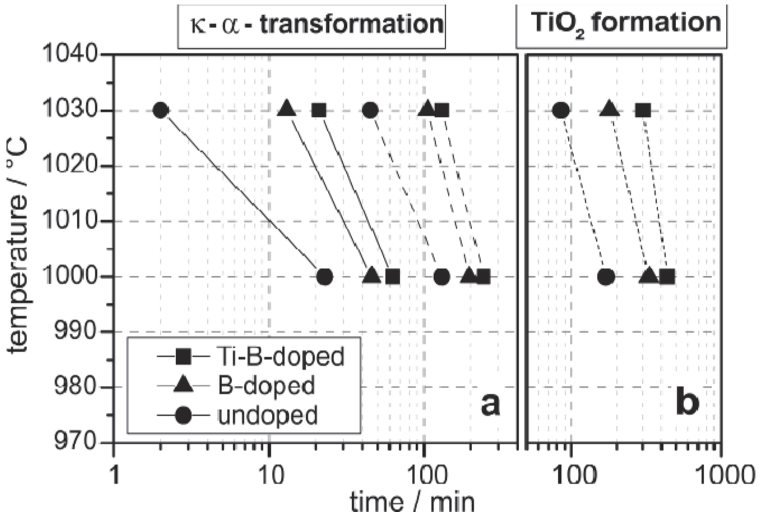

Fig. 4. κ-α-transformation (a) of undoped, B-doped and Ti-B-doped Al_2O_3 bilayer coatings showing start (solid lines) and finish times (dashed lines) at 1000 and 1030°C. The onset of TiO_2 formation (b, doted lines) occurs subsequently to the κ-α-transition.

In agreement with the HTXRD experiments, the undoped κ-Al_2O_3 bilayer transforms faster than the doped coatings during a 1000°C heat treatment with Ar flushing (below referred to as Ar-heat-treatment). Fig. 5a shows GAXRD patterns of the undoped, the B-doped and the Ti-B-doped samples after an 80 minute Ar-heat-treatment. The more pronounced α-Al_2O_3 peak confirms the faster κ-α-transformation of the undoped coating when comparing the κ-Al_2O_3

and α-Al_2O_3 peak at 2θ ~ 35° for all coatings. Simultaneously, most of the major α-Al_2O_3 peaks are clearly visible for the undoped coating after heat treatment but not for the doped coatings, hence corroborating the slower κ-α-transformation of the latter. In contrast to the HTXRD results, TiO_2 peaks are visible for all samples after much shorter Ar-heat-treatment times and the κ-α-transformation seems to be shifted to longer times. The undoped coating shows a considerable TiO_2 peak at 2θ = 27.5° after 60 minutes Ar-heat-treatment, while the first clear TiO_2 peaks appear after 100 minutes of HTXRD annealing at 1000°C for the same coating. For the Ti-B-doped coatings, the first TiO_2 peaks are detected after 120 minutes Ar-heat-treatment and after 300 minutes HTXRD. This earlier onset of TiO_2 formation is attributed to a higher oxygen partial pressure within the heat treatment furnace compared to the HTXRD chamber, which might have been introduced during sample batching despite the flushing with Ar. Comparing the transformation times of the HTXRD and Ar-heat-treatment, the slower κ-α-transformation during Ar-heat-treatment is more obvious for the doped coatings, as the undoped coating transforms relatively fast in both cases. In general, the starting of the κ-α-transformation occurs 3-4 times later for Ar-heat-treated samples. After 200 minutes Ar-heat-treatment (Fig. 5b), the GAXRD pattern of the undoped coating exhibits mainly TiO_2 peaks and a further phase appears. Delamination of the coating system is already visible to the naked eye, which explains the disappearing α-Al_2O_3 peaks and suggests the attribution of the additional phase to oxidized substrate material. For the same Ar-heat-treatment, delamination of the doped coatings occurred after ~400 minutes. The B-doped coating still contains a considerable κ-Al_2O_3 phase fraction, whereas in the Ti-B-doped coating the κ-Al_2O_3 phase is still dominating (Fig. 5b), which shows that Ti-B-doping further retards the κ-α-transformation compared to B-doping, also for the Ar-heat-treatment. For the 1000°C HTXRD experiments, after the same heat treatment time of 200 minutes, κ-α-transformation in the doped coatings was almost finished (see Fig. 4a, dashed lines), demonstrating the slower κ-α-transformation during Ar-heat-treatment.

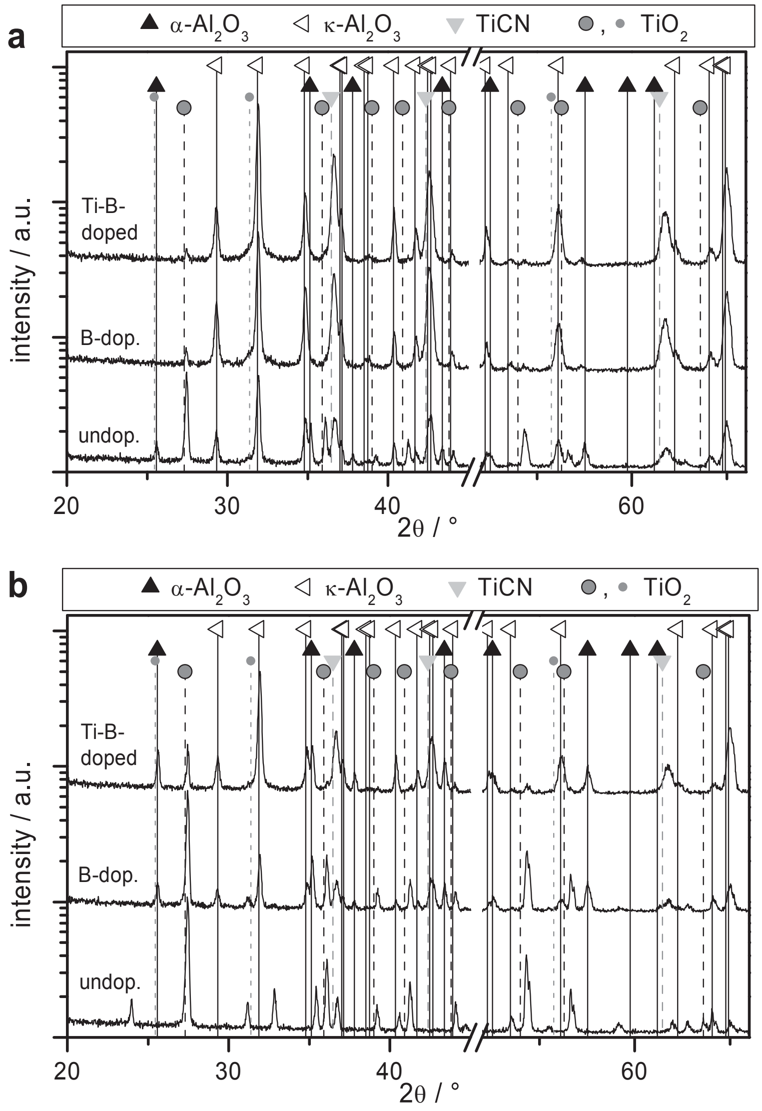

Fig. 5. GAXRD pattern of undoped, B-doped and Ti-B-doped Al_2O_3 bilayers after 80 minutes (a) and 200 minutes (b) heat treatment at 1000°C with Ar flushing.

The initial coating failure mechanism is exemplified in Fig. 6 for the undoped coating after 80 minutes Ar-heat-treatment. B-doped and Ti-B-doped coatings show a similar surface appearance after an Ar-heat-treatment time of ~200 minutes. The affected region appears slightly brighter in the backscattered electron image (Fig. 6b), which is attributed to a higher titanium content. With regard to the GAXRD results (see Fig. 5a), these regions seem to contain mainly TiO_2, where the Ti is provided by the base-layer. As the TiO_2 formation precedes the κ-α-transformation, it is supposed to occur primarily at thermal cracks formed during cooling down of the coating after deposition, until secondary cracks due to the κ-α-transformation are formed. The oxidation of the base-layer seems to lift off the Al_2O_3 bilayer, which causes a localized perforation and accelerates the oxidation process. This habit could be related to formation of titanium oxide already within the Al_2O_3 bilayer, hence causing local compressive stresses and buckling [46]. Additionally, titanium or TiO_2 seems to diffuse through the locally destroyed bilayer, increasing the volume of the hillocks growing on the Al_2O_3 surface. The generation of big pores, visible at the Al_2O_3/base-layer interface in Fig. 6a, deteriorates the adhesion of the Al_2O_3 bilayer and explains the coating delamination discussed above. Small pores are also visible between the Al_2O_3 layers, indicating a loss of interlayer atoms, but no separation of the two Al_2O_3 layers can be observed. Without oxidation protection by the Al_2O_3 layer, the TiCN base-layer heavily oxidizes, as TiCN is only oxidation resistant up to temperatures in the range of 500-650°C [47-49]. Consequently, also the cemented carbide is not protected against oxidation anymore.

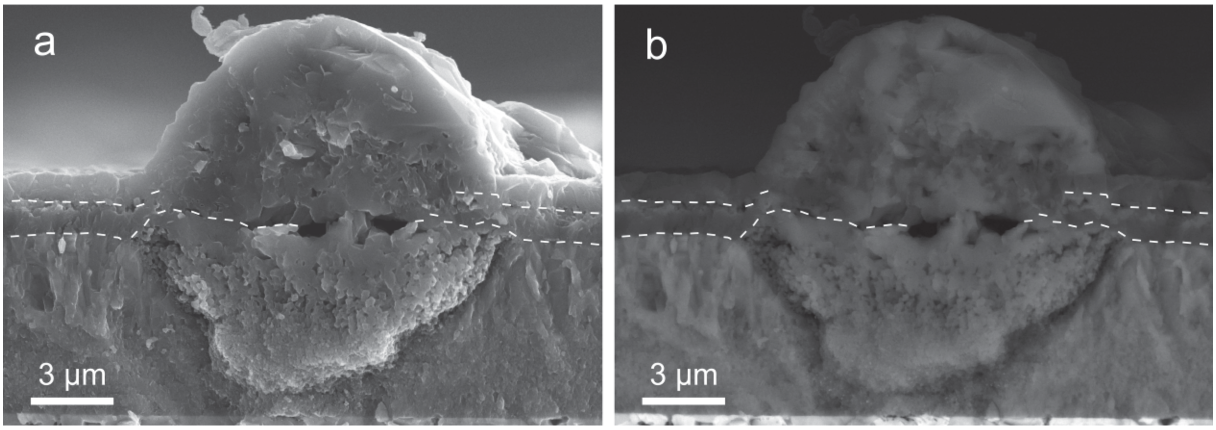

Fig. 6. SEM secondary electron (a) and backscattered electron (b) fracture cross-section images of the undoped κ-Al_2O_3 bilayer coating, after 80 minutes heat treatment at 1000°C (with Ar flushing). The interfaces "inner κ-Al_2O_3 / base layer" and "outer κ-Al_2O_3 / interlayer" are highlighted by dashed, white lines as a guide for the eye. The interlayer can be observed as brighter region below the upper dashed line in (b).

The vacuum-heat-treatment experiments performed at 1000°C at $\sim 10^{-6}$ mbar, thus minimizing oxidation processes, show the longest κ-α-transformation times within this study. After a vacuum-heat-treatment time of 720 minutes, the doped coatings contain a predominant fraction of κ-Al_2O_3 and also the undoped coating shows a still significant amount of κ-Al_2O_3 (Fig. 7). For HTXRD (cf. Fig. 4a) and Ar-heat-treatment (cf. Fig. 5b), the κ-α-transformation is finished much earlier. After vacuum-heat-treatment times longer than 16 hours, the GAXRD pattern of the undoped coating shows no κ-Al_2O_3 peaks anymore, but for the doped coatings the κ-Al_2O_3 peaks even do not disappear after a 32 hour vacuum-heat-treatment. At $2\theta = \sim 26°$ another peak doublet is visible, where the peak at lower angle perfectly fits to α-Al_2O_3. However, the peak at higher angle is attributed to an aluminum oxide (JCPDF # 00-048-0366) with an α-Al_2O_3 structure but slightly decreased lattice spacings, hence showing peak positions which are slightly shifted to higher angles. The detected amount of this second "α-Al_2O_3" phase is lower for the Ti-B-doped coating. Furthermore, the GAXRD patterns show an increasing amount of tungsten (JCPDF # 01-089-2767) with increasing heat treatment time for all coatings, which is generally higher for the undoped coating. Although the main tungsten peak is overlapping with a κ-Al_2O_3 peak, its strong increase, simultaneously to the disappearing of the κ-Al_2O_3 phase, justifies this attribution.

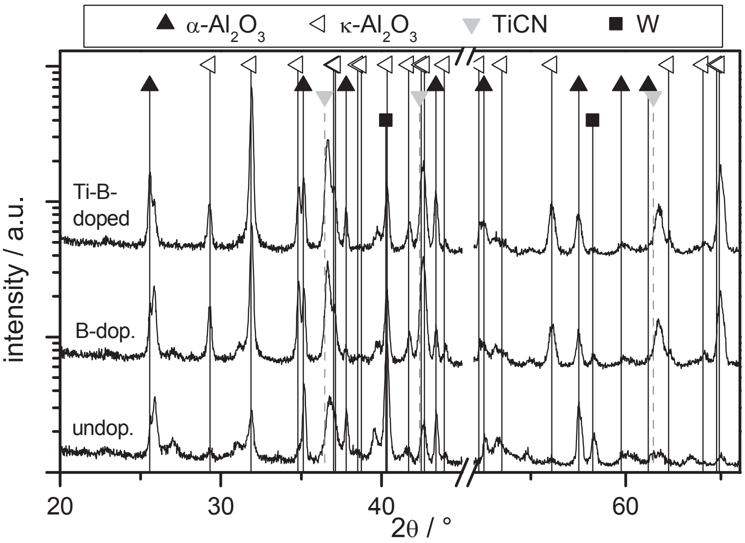

Fig. 7. GAXRD pattern of undoped, B-doped and Ti-B-doped Al_2O_3 bilayers after a 720 minutes vacuum heat treatment at 1000°C.

Qualitative EDS measurements (Fig. 8) confirm the occurrence of tungsten at the surface, where the brightness of the backscattered electron top-view images correlates with the tungsten enrichment. The darkest region (e.g. Fig. 1a, position 1) mainly consist of Al_2O_3 and the spectrum of the bright regions (e.g. Fig. 1a, position 2) shows a mixture of tungsten (major fraction) and Al_2O_3 (minor fraction). Within the brighter regions, there are also small bright spots visible (Fig. 1a, position 3), which mainly consist of tungsten. The top-view images (Fig. 8) clearly visualize the higher amount of tungsten segregated to the surface of the undoped coating. Furthermore, it is possible to distinguish between B-doped and Ti-B-doped coating. The latter shows less of the bright regions and no bright spots, i.e. less tungsten segregates to the surface. The brighter surface of the undoped coating, after 32 hours vacuum-heat-treatment, i.e. the higher amount of tungsten segregated to this surface, indicates that the undoped bilayer is a less efficient diffusion barrier when compared to the doped coatings, also suggested by the comparable faster formation of TiO_2 on undoped samples after HTXRD and Ar-heat-treatment (cf. Fig. 5).

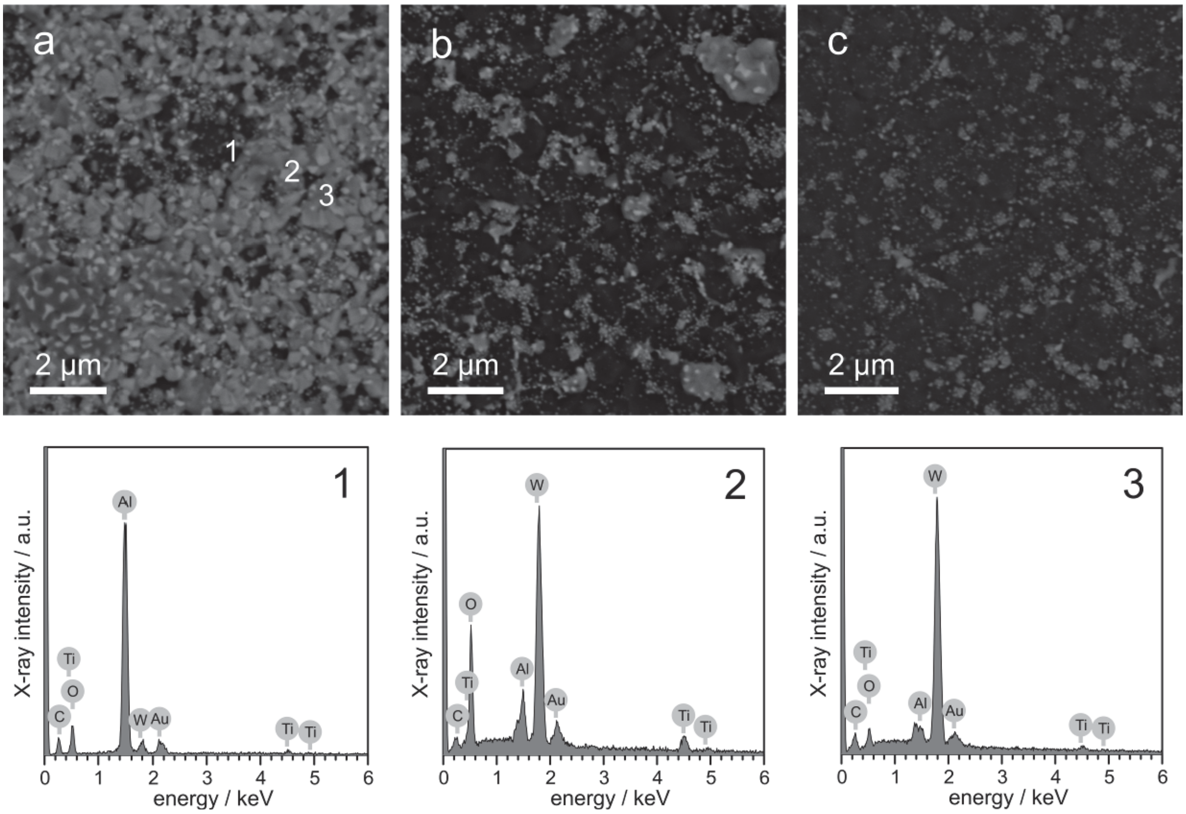

Fig. 8. SEM top-view images (electron backscattering mode) of undoped (a), B-doped (b) and Ti-B-doped Al_2O_3 bilayers (c) after a 1920 minutes vacuum heat treatment at 1000°C. The position of three qualitative EDS measurements on the undoped sample is indicated by numbers and the respective spectra are displayed in the lower row.

Fig. 9 displays a fracture cross-section of the undoped coating after 32 hours of vacuum-heat-treatment. No delamination is visible, confirming that the adhesion failure of the investigated coating systems, by applying thermal loads only, is at least partly determined by oxidation processes, but not directly by the κ-α-transformation. In agreement with the top-view micrograph (cf. Fig. 8a), the fracture cross-sections (Fig. 9b, c) display a bright surface layer, occasionally containing bright spots. There are also a few dome-shaped outgrows visible and both, outgrows and bright spots, seem to be located in the vicinity of cracks which appear also bright (Fig. 9c). The EDS line scan shows that these outgrows mainly consist of tungsten, but also contain a significant amount of titanium. Both elements seem to diffuse through cracks in the Al_2O_3 layers, indicated by the brightness of the cracks in Fig. 9b and more clearly in Fig. 9c, as well as by the tungsten concentration profile of the line scan. The profile exhibits a relatively high tungsten concentration within the outer Al_2O_3 layer, because the line scan coincides with a crack. As surface segregation of titanium is also observed, a small amount of titanium segregating at cracks is very probably, but mainly tungsten is detected. Furthermore, a tungsten peak at the interlayer and a tungsten diffusion gradient within the TiCN base-layer is visible. The diffusion gradient within the base-layer is much more pronounced and closer to

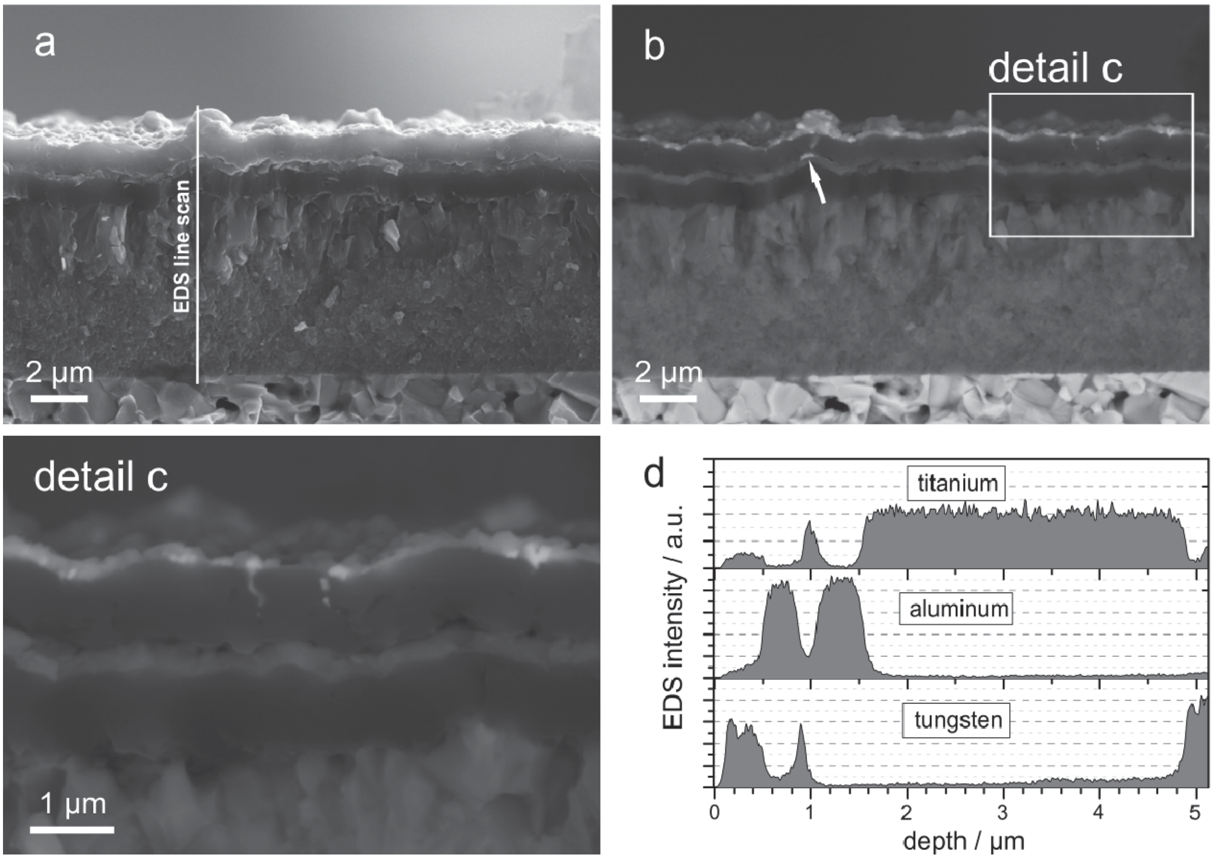

Fig. 9. SEM secondary electron (a) and backscattered electron (b) fracture cross-section images of the undoped κ-Al_2O_3 bilayer coating, after 1920 minutes vacuum heat treatment at 1000°C. The EDS line scan (d) starts within an outgrow at the surface (depth: ~0 µm – 0.5 µm) and shows the two Al_2O_3 layers, the interlayer (depth: ~1 µm), the TiCN base-layer (depth: ~1.6 µm – 4.8 µm) and the cemented carbide substrate (depth: ~5 µm).

the surface, when compared to the GDOES measurements on as-deposited coatings (cf. Fig. 2). Obviously, tungsten which may originate from the tungsten dissolved in the cobalt binder phase [50] of the cemented carbide substrate diffuses through the whole coating system. However, the big amount of tungsten detected with the EDS line scan, is attributed to its position close to a crack and close to an outgrow. On average, the amount of surface segregated tungsten is lower than detected with the EDS line scan. Thus, also diffusion of this lower amount of tungsten through the coating system could be possible. The titanium, detected within the outgrow, seems to mainly originate from the interlayer, as there are several pores visible at the interface of the outer Al_2O_3 layer and the interlayer. Occasionally, these pores seem to be “filled” with tungsten, as visible at the fracture cross-section (Fig. 9b, white arrow) and detected with EDS (tungsten peak close to the interlayer, Fig. 9d). Consequently, the detected tungsten peak shows a single pore where tungsten is segregated, but does not represent a continuous layer of tungsten underneath the outer Al_2O_3 layer. Compared to the other heat treatment processes, it is assumed that the absence of oxygen causes a lower chemical potential for titanium diffusion through the Al_2O_3 layer.

Consequently, a slower transport of titanium, away from the Al_2O_3 interfaces, occurs and fewer pores are generated. Hence, sufficient adhesion is maintained, and coating delamination even does not occur for heat treatment times as long as 32 hours. Moreover, the diffusion of tungsten through the whole coating system does not destroy the coating integrity, unlike shorter heat treatments accompanied by TiO_2 formation. This indicates that the diffusion of metal atoms through the coating system is less destructive, as long as the formation of oxides within the diffusion paths is avoided.

4. Comparative discussion of the transformation

Table 1 summarizes the above mentioned transformation times. The start time values for HTXRD are slightly smaller than those displayed in Fig. 4a, due to the fact that the graph shows the decline of κ-Al_2O_3 peaks, while in Table 1 the first clear appearance of α-Al_2O_3 peaks is listed. This difference also gives a hint for the order of magnitude of uncertainty of the time values. The κ-α-transformation finish time for undoped coating during Ar-heat-treatment is omitted as the massive formation of TiO_2 impedes a clear determination.

Table 1

κ-α-transformation start and finish times given in minutes for different heat-treatment processes at 1000°C

Coating	HTXRD	Ar-heat-treatment	vacuum-heat-treatment
undoped	15 / 130	70 / -	300 / 800
B-doped	20 / 200	150 / 250	700 / >1920
Ti-B-doped	40 / 240	180 / 300	480 / >1920

The observed diffusion of tungsten and titanium through the Al_2O_3 layers is related to a covered coating surface and covered surfaces of the thermal cracks, which are the preferred regions for the initiation of the κ-α-transformation and nucleation of α-Al_2O_3 grains [19, 31]. Molecular dynamic simulations [28] suggest that the mobility provided by surface diffusion is vital for the κ-α-transformation. Therefore, the coverage of surfaces with a tungsten-titanium film could be a reason for a retarded initiation of the κ-α-transformation. Apparently, the tungsten film limits the mobility at Al_2O_3 surfaces much more than the occurrence of an oxide species like TiO_2 does. This could be related to the higher density of the metal film which might impede diffusion processes more efficiently. In addition, TiO_2 is known to possess a strong disorder in its lattice structure [51], which could make diffusion more easily for atoms at the former free surface of Al_2O_3. Thus, the later onset of κ-α-transformation for the vacuum-heat-treated samples can be attributed to the segregation of tungsten and titanium at the free Al_2O_3 surfaces.

Considering the difference between Ar-heat-treatment and HTXRD, the earlier and more pronounced onset of TiO_2 formation for the Ar-heat-treatment, which is related to a higher oxygen partial pressure, causes a slower nucleation of the κ-α-transformation, compared to the HTXRD. The lower oxygen partial pressure within the HTXRD chamber, where the κ-α-transformation starts before the onset of TiO_2 formation, allows a less affected κ-α-nucleation process, which is consequently the fastest one within this study. Moreover, the oxygen partial pressure seems to influence the κ-α-transformation time itself (cf. Table 1). For both doped coatings, the transformation time (difference between finish and start time) increases from ~100 minutes to ~200 minutes and >1200 minutes, for Ar-heat-treatment, HTXRD and vacuum-heat-treatment, respectively. The undoped coating transforms within ~20 minutes, ~100 minutes and ~300 minutes, respectively. Obviously, an oxidizing atmosphere allows a faster progress of the κ-α-transformation, where a decreased oxygen partial pressure prolongs the transformation time. Changing to a reducing atmosphere, provided by high vacuum in combination with high temperature, strongly increases the κ-α-transformation times. This behavior is in agreement with the stabilization of doped transition alumina by a reducing atmosphere as reported in literature [52]. The present results also show the stabilization of undoped κ-Al_2O_3, which contains a much lower amount of foreign atoms (cf. Fig. 2).

As doping elements incorporated within the Al_2O_3 are consistently prolonging the κ-α-transformation time for all heat-treatment processes, it is assumed that the diffusion processes during the κ-α-transformation (changing of the stacking of the anion sublattice and changing the arrangement of the cations therein) proceed at a slower speed for doped Al_2O_3. In literature, the influence of impurities and dopants is often examined with regard to grain boundary segregations [32, 33], but the influence of doping elements within this study is related to solid soluted dopants in the Al_2O_3, as indicated in Fig. 2. Furthermore, based on the assumption of a higher solubility limit for κ-Al_2O_3 compared to α-Al_2O_3, segregation of boron and titanium could be a necessary prerequisite for the κ-α-transformation, in order to allow nucleation and growth of α-Al_2O_3. Such an additional segregation process can be assumed to consequence longer transformation times for doped coatings compared to undoped ones.

5. Conclusions

The addition of BCl_3 and $TiCl_4$ to the precursor gas mixture of κ-Al_2O_3 bilayers grown by thermally activated chemical vapor deposition seems to cause an incorporation of boron and titanium atoms, which indicates a higher solubility limit of these dopants within the κ-Al_2O_3, when compared to α-Al_2O_3.

The initiation of κ-α-transformation is influenced by the coverage of free surfaces and depends also on the covering material. The higher oxygen partial pressure within a conventional heat treatment furnace allows an earlier and more pronounced TiO_2 formation, which causes a retarded κ-α-transformation when compared to HTXRD investigations with its lower oxygen partial pressure. Much longer nucleation times are observed for vacuum heat treatments where the free surfaces are covered by a tungsten film, which probably contains a minor amount of titanium. A decreasing oxygen partial pressure, i.e. changing the heat treatment facility from a conventional heat treatment furnace (Ar-flushed) via a HTXRD equipment (N_2-flushed) to a vacuum furnace, prolongs the time period between onset and finishing of the κ-α-transformation.

During heat treatment, the deteriorated Al_2O_3 coating adhesion is rather determined by oxidation of the base-layer than by the κ-α-transformation itself. Consistently for all investigated heat treatment processes, the B-doped κ-Al_2O_3 transforms slower than the undoped one and Ti-B-doping causes a still slower κ-α-transformation. In the same line, the undoped κ-Al_2O_3 seems to be a less efficient diffusion barrier, compared to the doped layers. The Ti-B-doped κ-Al_2O_3 bilayer revealed to be the most thermally stable and most efficient diffusion barrier within this work.

Acknowledgement

Financial support by the Austrian Federal Government and the Styrian Provincial Government, within the research activities of the K2 Competence Center in the framework of the Austrian COMET Competence Center Programme, is gratefully acknowledged. The authors are grateful to G. Hawranek for the SEM investigations and DI Florian Rovere for helpful discussions.

References

[1] H.O. Pierson, Handbook of Chemical Vapor Deposition (CVD), Noyes Publ., Park Ridge, New Jersey, 1999.

[2] A. Petzold, Aluminiumoxid: Rohstoff, Werkstoff, Werkstoffkomponente, Deutscher Verlag für Grundstoffindustrie, Leipzig, 1991.

[3] H. Strakov, M. Auger, R. Bonetti, R. Dielis, in: L. Sigl, P. Rödhammer, H. Wildner (Eds.), 17th Int. Plansee Seminar, Reutte, 2009, p. 261.

[4] D.G. Cahill, S.M. Lee, T.I. Selinder, J. Appl. Phys. 83/11 (1998) 5783.

[5] P.K. Mehrotra, D.T. Quinto, High Temp.-High Press. 18 (1986) 199.

[6] C.-S. Park, J.-G. Kim, J.S. Chun, J. Vac. Sci. Technol. 1/4 (1983) 1820.

[7] S. Ruppi, J. Phys. IV 11/3 (2001) 847.

[8] C. Chatfield, J.N. Lindstrom, M.E. Sjostrand, J. Phys. 50/5 (1989) 377.

[9] E. Fredriksson, J.O. Carlsson, J. Chem. Vap. Dep. 1 (1993) 333.

[10] M. Halvarsson, H. Norden, S. Vuorinen, Surf. Coat. Technol. 61/1-3 (1993) 177.

[11] S. Ruppi, A. Larsson, Thin Solid Films 388/1-2 (2001) 50.

[12] G.W. Brindley, J.O. Choe, Am. Miner. 46/7-8 (1961) 771.

[13] M. Halvarsson, H. Nordén, S. Vuorinen, Surf. Coat. Technol. 68-69 (1994) 266.

[14] M. Halvarsson, S. Vuorinen, H. Norden, Mat. Res. Soc. Symp. Proc. 314 (1993) 83.

[15] B. Lux, C. Colombier, H. Altena, K. Stjernberg, Thin Solid Films 138/1 (1986) 49.

[16] C.-S. Park, J.-G. Kim, J.S. Chun, J. Electrochem. Soc. 130/7 (1983) 1607.

[17] S. Vuorinen, J. Skogsmo, Thin Solid Films 193/1-2 (1990) 536.

[18] M. Halvarsson, S. Vuorinen, Surf. Coat. Technol. 76-77/1 (1995) 287.

[19] P. Hansson, M. Halvarsson, S. Vuorinen, Surf. Coat. Technol. 76-77 (1995) 256.

[20] J. Skogsmo, M. Halvarsson, S. Vuorinen, Micron Microscop. Acta 23/1-2 (1992) 219.

[21] E. Fredriksson, J.-O. Carlsson, Surf. Coat. Technol. 56/2 (1993) 165.

[22] C. Colombier, J. Peng, H. Altena, B. Lux, Int. J. Refract. Hard Met. 5/2 (1986) 82.

[23] M. Danzinger, R. Haubner, B. Lux, in: T.S. Sudarshen, D.G. Bhat (Eds.), Surf. Modif. Technol. III, The Minerals, Metals & Materials Society, Warrendale, 1990, p. 829.

[24] N. Lindulf, M. Halvarsson, H. Norden, S. Vuorinen, Thin Solid Films 253/1-2 (1994) 311.

[25] O.V. Andryushkova, O.A. Kirichenko, V.A. Ushakov, V.A. Poluboyarov, Solid State Ionics 101-103 (1997) 647.

[26] A. Larsson, M. Halvarsson, S. Ruppi, Surf. Coat. Technol. 111/2-3 (1999) 191.

[27] S. Vuorinen, L. Karlsson, Thin Solid Films 214/2 (1992) 132.

[28] A.B. Belonoshko, R. Ahuja, B. Johansson, Phys. Rev. B 61/5 (2000) 3131.

[29] A. Larsson, M. Halvarsson, S. Vuorinen, Int. J. Refract. Met. Hard Mat. 16/4-6 (1998) 369.

[30] G. Gassner, P.H. Mayrhofer, J. Patscheider, C. Mitterer, Thin Solid Films 515/13 (2007) 5411.

[31] J. Skogsmo, M. Halvarsson, S. Vourinen, Surf. Coat. Technol. 54/1-3 (1992) 186.

[32] B. Bloch, B.C. Ravi, R. Chaim, Mater. Lett. 42/1 (2000) 61.

[33] S. Lartigue-Korinek, C. Legros, C. Carry, F. Herbst, J. European Ceram. Soc. 26/12 (2006) 2219.

[34] O. Mekasuwandumrong, P. Tantichuwet, C. Chaisuk, P. Praserthdam, Mater. Chem. Phys. 107/2-3 (2008) 208.

[35] X. Wu, B. Yang, D. Weng, J. Alloys Comp. 376/1-2 (2004) 241.

[36] B.D. Fahlman, A.R. Barron, J. Chem. Vap. Dep. 7/2 (2001) 62.

[37] M. Kathrein, W. Schintlmeister, W. Wallgram, U. Schleinkofer, Surf. Coat. Technol. 163-164 (2003) 181.

[38] T. Nelis, J. Pallosi, Appl. Spectr. Rev. 41/3 (2006) 227.

[39] M.R. Winchester, R. Payling, Spectrochim. Acta B 59/5 (2004) 607.

[40] W.D. McKee, E. Aleshin, J. Am. Ceram. Soc. 46/1 (1963) 54.

[41] G. PetotErvas, B. Saadi, C. Petot, M. Loudjani, J. European Ceram. Soc. 17/7 (1997) 943.

[42] D. Hochauer, C. Mitterer, M. Penoy, C. Michotte, H.P. Martinz, M. Kathrein, in: L. Sigl, P. Rödhammer, H. Wildner (Eds.), 17th Int. Plansee Seminar, Reutte, 2009, p. 555.

[43] S. Canovic, S. Ruppi, J. Rohrer, A. Vojvodic, C. Ruberto, P. Hyldgaard, M. Halvarsson, Surf. Coat. Technol. 202/3 (2007) 522.

[44] Y. Yourdshahyan, C. Ruberto, M. Halvarsson, L. Bengtsson, V. Langer, B.I. Lundqvist, S. Ruppi, U. Rolander, J. Am. Ceram. Soc. 82/6 (1999) 1365.

[45] D. Hochauer, C. Mitterer, M. Penoy, C. Michotte, H.P. Martinz, M. Kathrein, Surf. Coat. Technol. 203/3-4 (2008) 350.

[46] H. Hindam, D.P. Whittle, Oxid. Met. 18/5-6 (1982) 245.

[47] A. Mitsuo, S. Uchida, N. Nihira, M. Iwaki, Surf. Coat. Technol. 103-104 (1998) 98.

[48] J. Wagner, C. Mitterer, M. Penoy, C. Michotte, W. Wallgram, M. Kathrein, in: G. Kneringer, P. Roedhammer, H. Wildner (Eds.), 16th Int. Plansee Seminar, Reutte, 2005, p. 917.

[49] M. Wittmer, J. Noser, H. Melchior, J. Appl. Phys. 52/11 (1981) 6659.

[50] W. Schedler, Hartmetall, VDI-Verl., Düsseldorf, 1988.

[51] C. Leyens, in: C. Leyens, M. Peters (Eds.), Titanium and Titanium Alloys, Wiley-VCH Verlag GmbH & Co. KGaA, Weinheim, 2003, p. 187.

[52] A. Piras, A. Trovarelli, G. Dolcetti, Appl. Catal. B 28/2 (2000) L77.